ICFO - INSTITUT DE CIÈNCIES FOTÒNIQUES
AND
UPC - UNIVERSITAT POLITÈCNICA DE CATALUNYA

Thermal and optical-gain effects in nanophotonics with applications to sensing and perfect absorption

LIJUN MENG

Supervisor: Prof. Javier García de Abajo

Co-supervisor: Prof. Min Qiu

PhD Thesis - 2018

Contents

List of Acronyms

SPP – Surface plasmon polariton

LSP – Localized surface plasmon

SPR – Surface plasmon resonance

FWHM – Full width at half maximum

NIR – Near infrared

MIR – Middle infrared

TBC – Thermal boundary conductance

UCNP – Upconversion nanoparticle

LDOS – Local density of optical states

ERR – Electric ring resonator

MIM – Metal insulator metal

FOM – Figure of merit

ABSTRACT

Thanks to rapid developments of nanofabrication techniques and numerical simulation capabilities, the past decades have witnessed an explosive expansion of the field of nanophotonics. The main aim in this area is to unveil novel phenomena involving interactions between electromagnetic waves and material objects at the nanoscale. The resulting discoveries are benefiting our society and believed to contribute to a sustainable future. Surface plasmons, which are characteristic oscillations of induced charges at metal surfaces that can interact strongly with light, are a key topic in nanophotonics. Surface plasmons can tightly confine the optical electric energy in the vicinity of metallic nanostructures, resulting in a largely enhanced field intensity. These appealing properties have been exploited to break the diffraction limit, boost optical nonlinear effects, and improve the performance of solar cells, among other feats.

Plasmons can be engineered to interact strongly with external light, which is oftentimes illustrated by a large absorption cross-section of the host structure compared with its projected physical area. When such nanostructures are arranged into a periodic array, it can even totally absorb the energy of an incident light wave, a phenomenon that is known as perfect absorption. Controlling the full width at half maximum (FWHM) of the spectrum, especially realizing perfect absorption with ultranarrow bandwidth, is desirable for sensitive photodetection among other appealing potential applications. In the first part of this thesis, we present a grating-based absorber with FWHM smaller than 1 nm. This very small bandwidth results from the low dissipation rate of the delocalized resonance supported by the structure. Commonly, ultranarrow band absorbers rely on various delocalized resonances, which require the absorber to have a relatively large spatial extension. In this context, we further propose a general method to guide a rational design of

ultranarrow band absorbers that are based instead on localized resonances, which make it affordable to minimize the size of the absorbers. The basic idea is to utilize some high-order localized mode rather than the customarily used fundamental mode of a resonator to reduce the radiative decay rate. Additionally, we consider dielectric elements doped with gain impurities to compensate for the inelastic decay rate. We implemented this method in three kinds of absorbers that are based on different absorption mechanisms. All absorbers display dramatically improved performances compared with previous designs based on the use of fundamental modes.

Metallodielectric coreshell nanospheres constitute a classical and thoroughly studied structure in the nanoplasmonic community. In the second part of this thesis, we investigate the use of localized plasmon resonances supported by a metal shell to enhance the emission intensity of an upconversion nanoparticle embedded in the center of the dielectric core. To this end, a theoretical model accounting for absorption and emission processes of the system is established. Based on this theory, optimized coreshell structures are found under different pump intensity regimes. In the same chapter, we extend the simple coreshell nanoparticle structure to more complex multilayers, which consist of alternate metal/dielectric shells. We reveal a cascade effect of the field enhancement in the structure. This can lead to huge intensity in the core under moderate light illumination. We further study its photothermal performance by computing the resulting temperature distribution. It is interesting to find that the temperature increase can be very spatially inhomogeneous with the highest temperature in the center. The reason lies in the high inhomogeneity of the field enhancement and considerable thermal boundary resistance provided by multiple metal/dielectric interfaces. Finally, the thermally induced internal pressure lift is also calculated.

The interaction between light and particle arrays is a popular topic with great potential for practical applications. The collective behavior of the particles can be very different from the isolated ones. For example, a regular array of tiny nanoparticles is able to totally reflect the impinging light. Recently, it has been realized that a regular array of two-level atoms holds the same capability. In the third part of this thesis, we take a step further to explore light scattering on three-level atom arrays. Unlike the two-level atom, which elastically interacts with light, the three-level atom can either dissipate, perfectly reflect, or amplify the probed

light. Our investigations demonstrate these effects vividly, and how they can be controlled through the pump light intensity.

RESUMEN

Durante las últimas décadas la comunidad científica ha sido testigo de un rápido crecimiento del campo de la nano fotónica. Este avance ha sido principalmente motivado tanto por el rápido desarrollo en las técnicas de fabricación de dispositivos en la escala del nanómetro como por el incremento de las capacidades de simulación numérica. El objetivo prioritario de la nano fotónica es iniciar la investigación para el estudio de nuevos fenómenos que tienen lugar en la interacción de la luz con objetos de tamaño nanométrico. Se espera que los resultados de la investigación contribuyan al beneficio de la sociedad, así como para el desarrollo de un futuro sostenible. Uno de los ingredientes más importantes dentro del campo de la nano fotónica son los plasmones de superficie, siendo éstos las oscilaciones de la nube electrónica que yacen en la interfaz entre un material metálico y un dieléctrico. Los plasmones de superficie son capaces de concentrar altas cantidades de energía eléctrica produciendo así un incremento del campo eléctrico respecto al inicialmente aplicado. Estas propiedades han sido estudiadas y empleadas para sobrepasar la barrera de difracción, impulsar aplicaciones de óptica no lineal, mejorar el rendimiento de placas solaras, entre otras aplicaciones.

Los plasmones pueden ser diseñados de tal manera que interaccionen fuertemente con la luz incidente, donde habitualmente la sección eficaz de la estructura, normalizada al área proyectada, presenta un máximo. Cuando estas estructuras se disponen de forma adecuada en una red periódica puede ocurrir una absorción completa de la energía electromagnética de la onda incidente, efecto que se conoce como absorción total. El control del ancho de banda a media altura (por sus siglas en ingles FWHM) del espectro es especialmente importante cuando se realiza la absorción total, donde se requiere un ancho de banda muy estrecho. Este tipo de montajes son muy útiles en foto-detección de alta precisión, así como para otras aplicaciones

interesantes que empiezan a emerger. En la primera parte de la tesis presentamos una red de absorción con un FWHM menor de 1 nm. El pequeño ancho de banda conseguido es debido al bajo ritmo de dispersión de las resonancias deslocalizadas que son soportadas por la estructura. En general, para procesos de absorción , los anchos de banda extremadamente pequeños se basan en diversas resonancias deslocalizadas, lo que implica que las dimensiones de los objetos que absorben han de ser grandes. Es por eso que proponemos un modelo racional para conseguir anchos de banda muy pequeños basados en resonancias localizadas, permitiendo así disminuir el tamaño de los objetos absorbentes. La principal idea para conseguirlo es crear un diseño basado en la excitación de modos localizados de orden elevado en lugar de manipular la forma del objeto para excitar el modo fundamental, así pues, se consigue reducir la tasa de desintegración radiativa. Además, consideramos objetitos dieléctricos dopados con elementos activos para compensar por la desintegración radiativa inelástica. En esta tesis, aplicamos el método a tres tipos diferentes de mecanismos de absorción. En cualquiera de los tres escenarios, los resultados muestran una mejora notable comparada con el uso de métodos basados en la excitación del modo fundamental.

La comunidad de la nano plasmónica ha estudiado en profundidad, y desde ya hace años, las esferas multicapa compuestas por la combinación de materiales metálicos y dieléctricos. En la segunda parte de la presente tesis, estudiamos el uso de los plasmones creados en carcasas metálicas para incrementar la señal emitida por nano partículas de conversión ascendente colocadas en el centro dieléctrico de la estructura. De esta forma, se presenta un formalismo teórico que tiene en cuenta la emisión y la absorción del sistema. Considerando este modelo teórico, se han encontrado diseños para la carcasa dieléctrica-metálica óptimos en función de las intensidades aplicadas. Más adelante, se extiende el modelo para multi-capas considerando de forma alternativa materiales metálicos y dieléctricos. En este tipo de estructuras observamos un efecto cascada en cuanto al incremento del campo se refiere. Por este motivo, las estructuras en multi-carcasa pueden crear un campo enrome en su interior con una iluminación inicialmente tenue. Además, estudiamos los efectos foto-térmicos determinando la distribución resultante de temperaturas. Es interesante mencionar que el incremento de la temperatura hacia el centro es considerablemente homogéneo hasta alcanzar la temperatura más alta en su interior.

Esto es debido a la gran inhomogeneidad del incremento del campo y la considerable resistencia térmica que hay en las uniones entre el metal y el dieléctrico. Finalmente, se determina el incremento de la presión inducida en la estructura.

La interacción entre la luz y redes de nano partículas es de un gran interés científico con un alto potencial en aplicaciones prácticas. El comportamiento de la disposición en red de las partículas, puede ser completamente diferente al de una sola. Por ejemplo, una red cuadrada compuesta de pequeñas partículas nano métricas es capaz de reflejar por completo la luz incidente. Recientemente, se ha conseguido el mismo efecto con una red regular cuyos constituyentes son átomos de dos niveles. En la tercera parte de esta tesis, damos un paso más allá y estudiamos redes de átomos de tres niveles. A diferencia de los átomos de dos niveles, que interaccionan de forma elástica con la luz, los átomos de tres niveles pueden disipar, reflejar perfectamente o amplificar un haz de prueba. Nuestras investigaciones demuestran todos los efectos mencionados y como pueden ser éstos controlados a través de la intensidad aplicada.

ABSTRACT IN CHINESE

得益于纳米加工技术和数值模拟方法的快速进步，纳米光子学在过去几十年里获得了蓬勃的发展。纳米光子学是一门致力于研究电磁波和物质在纳米尺度内相互作用的学科。这一领域的科学发现和与之相伴随的技术进步正在不断为我们社会的可持续发展做出贡献。表面等离子体是存在于金属表面的自由电子的集体振动。对它的研究构成了纳米光子学重要的一个部分。表面等离子体能够强烈的和来自远场的入射光波相耦合，把光子能量紧约束在纳米结构的附近，从而极大的增强纳米尺度内电磁场的强度。这一优秀的特性可以被用来打破衍射极限，增强光学非线性，以及提高太阳能电池的效率等等。

人们通常可以用相对于纳米结构物理几何尺寸更大的光学吸收截面来表征该结构所支持的表面等离子体。当把这些分立的结构排成周期阵列时，甚至可以完全吸收入射光波的能量。这一现象通常被称为光学完美吸收。控制吸收谱线的带宽，尤其是设计出超窄带的完美吸收器是这一领域努力的目标之一。它可以帮助人们制造出非常敏感的光学探测器，传感器等。在本论文的第一部分中，我们设计了一种基于光栅的吸收器，它的半高宽小于1纳米。其原因是，此种光栅支持的非定域谐振模式在结构表面传播时拥有非常低的能量损耗率。大部分报道的超窄带吸收器都是利用类似的光学非定域传播模式。这导致吸收器必须要有相对于吸收波长较大的几何面积。所以，进一步的，我们提出一种方法可以理性的设计出有超窄带，同时尺寸又微小的吸收器。基本思路是利用结构支持的高阶定域谐振模式，而非一般使用的低阶基模来降低和远场的耦合。另外，我们还需要在吸收器电介质成分中掺杂增益材料来补偿金属中过大的热损耗率。我们应用这一思路设计了三种基于不同吸收机制的小尺寸超窄带光学吸收器。发现它们的相关特性都优于采用传统基模的对照结构。

金属电介质壳核纳米球形结构是纳米等离子体领域中一个经典的研究对象。在本论文的第二部分，我们首先研究了如何用金属球形壳层支持的定域表面等离子体谐振来增强位于纳米颗粒中心的上转换材料的远场辐射强度。为此，我们发展了一个简单的模型来描述上转换材料的吸收和辐射过程。结合基于Mie理论的仿真计算，我们指出在不同泵浦光强下的最优结构。在同一章中，我们进一步研究了更复杂的多层纳米球形结构，它由一系列的金属和电介质壳层交替排列而成。我们揭示了此类结构中多个金属壳层支持的表面等离子体发生协同共振时引起的光学增强级联效应。它能将入射光能量聚焦在结构中心，引起中心区域极大的光场增强。我们还计算了光热效应引起的温度分布。发现即使在连续光照射的稳定状态下，由于电场强度的空间不均匀分布和不同材料壳层界面存在的界面热阻效应，温度的空间分布也是很不均匀的，中心处温度最高。最后，我们计算了主要由升温引起的结构内部压强的增大。

光与纳米颗粒阵列的相互作用由于其拥有的巨大应用潜力而成为一个热门研究方向。阵列中，颗粒之间的电磁相互作用所引起的所谓晶格谐振使得它对入射光的响应和单个颗粒的情况很不一样。比如，一个由极小颗粒排成的规则阵列可以完全反射入射光。最近的理论研究显示，即使把更小的二能级原子排成阵列也能达到相同的效果。在本论文的最后一部分中，我们进一步研究了入射光和三能级原子阵列的相互作用。不同于二能级原子只能和光发生弹性相互作用，我们发现，受泵浦光强调控的同一个三能级原子阵列既可以高效反射和吸收入射光，也可以变得对入射光高透，还可以对光进行放大。

Acknowledgments

At this very special moment, recalling the past 5+ years, I want to express my sincere gratitude to many people. This thesis cannot be finished without them.

I would like to thank my supervisor Prof. Javier García de Abajo for giving me the valuable opportunity to work as an international PhD student at ICFO. I am often shocked by his broad and deep knowledge. I thank him very much for his kind guidance and encouragements in my daily study. I always enjoy exciting discussions with him. They benefit me a lot during the past years.

I would like to thank my co-supervisor Prof. Min Qiu in Zhejiang University (ZJU), who recommended me to come here and monitored my work when I was in China. I am very grateful for his permanent and critical supports, which start when I was an undergraduate student. He led me enter into this amazing world of nanophotonics. I am continuously learning a lot from him in but not limited in academic research.

I think I am extremely fortunate to have them as my supervisors. They both have made great achievements in science. They are great examples for my life.

I also thank Prof. Zhichao Ruan and Prof. Qiang Li very much for their large amount of help when I was in ZJU. They are outstanding young experts, whose devoted work attitudes often stimulate me.

I want to say big thank you for my colleagues in Spain and China. They are Joel D. Cox, Deng Pan, Vahagn Mkhitaryan, Jose R. M. Saavedra, Renwen Yu, Sandra de Vega, Alvaro Rodriguez Echarri, Andrea Marini, Wei Cai, Dongli Liu, Ding Zhao, Yuanqing Yang, Hanmo Gong, Xinxin Chen, Si Luo, Hangbo Yang, Songan Bai, Kaikai Du, Jian Qin, Jingyi Tian, Yurui Qu, Meiyan Pan, Lu Cai, Yu hong, Huanzheng Zhu, Hao Luo, Jinsheng Lu, Ziquan Xu, Binze Ma, Yun Huang, Xuelu Pei, Ziyao Chen, Chuming Liu, Guangnan Yao, Wenting Zhao, Han Wang.

They made my life much more vivid in different periods during my PhD. Some of them are my close collaborators of the works presented in this thesis. Especially, I also want to thank some of my friends meet in Spain not mentioned above. They are Yan Xu, Jia Kong, Nan Li, Hanyu Ye, etc. They brought me lots of fun in a place far from my hometown.

Thanks to this PhD program, I have the opportunity to live in Barcelona for some time. I like this land and the people on it. I think they will constitute an important part of my memory in my life. I look forward to travelling back in the future.

At last, I thank my families and relatives, especially my mother. I am grateful to her throughout my life.

Castelldefels, Barcelona
September 2018

List of Publications

Publications included in this thesis

1. **Lijun Meng**, Ding Zhao, Zhichao Ruan, Qiang Li, Yuanqing Yang, and Min Qiu, "Optimized grating as an ultra-narrow band absorber or plasmonic sensor," ***Optics Letters*** *39(5), 1137-1140, (2014).*

2. **Lijun Meng**, Renwen Yu, Min Qiu, and Javier García de Abajo, "Plasmonic nano-oven by concatenation of multishell photothermal Enhancement," ***ACS Nano*** *11(8), 7915-7924, (2017).*

3. Vahagn Mkhitaryan*, **Lijun Meng***, Andrea Marini, and Javier García de Abajo, "Lasing and amplification from two-dimensional atom arrays," ***Physical Review Letters*** *121(16), 163602-163606, (2018).* ***equal contribution**

4. **Lijun Meng**, Ding Zhao, Yuanqing Yang, Javier García de Abajo, Qiang Li, Zhichao Ruan, and Min Qiu, "Gain-assisted plasmon resonance narrowing and its application in sensing," *submitted.*

Other relevant publications

1. **Lijun Meng**, Ding Zhao, Qiang Li, and Min Qiu, "Polarization-sensitive perfect absorbers at near-infrared wavelengths," ***Optics Express*** *21(101), A111-A122, (2013).*

2. Ding Zhao, **Lijun Meng**, Hanmo Gong, Xingxing Chen, Yiting Chen, Min Yan, Qiang Li, and Min Qiu, "Ultra-narrow-band light dissipation by a stack of lamellar silver and alumina," ***Applied Physics Letters*** *104 (22), 221107, (2014).*

3. Weichun Zhang, Qiang Li, **Lijun Meng**, Ding Zhao, and Min Qiu, "Universal scaling behavior of the temperature increase of a heat nanoparticle on a substrate," ***Journal of Nanophotonics*** *9 (1), 093046, (2015).*

Chapter 1

Introduction

Plasmonic nanostructures have attracted great interest in recent years since they provide us with a tool to manipulate light at the nanometer scale. The process is mediated by collective oscillations of free electrons known as surface plasmon resonances (SPRs), which are able to interact strongly with external light and largely concentrate electromagnetic intensity in the near-field [1]. They further facilitate energy conversion at the microscale, such as in hot-carrier generation [2, 3] and localized heating [4, 5]. These appealing features have led to intense research activities exploiting various structures used for nonlinear optics [6, 7], ultrasensitive molecular detection via surface-enhanced Raman scattering (SERS) [8, 9], photochemistry [10, 11], nanofabrication [12, 13], meta-holograms [14, 15], and perfect light absorption [16, 17, 18], just to name a few.

It is well known that the geometrical morphology of the nanostructure, now can be shaped at will using modern technologies (*e.g.*, femtosecond laser direct writing [19]), can dominate its interaction with light in many cases. In a different context, gain materials play an increasingly important role in this field. This is not only because they can compensate the intrinsic loss of metals, but also due to the fact that they provide a degree of freedom to actively tune the optical functionality of the structures. In this context, the aim of the works presented in this thesis is to study some novel geometrical and gain effects with potential for practical applications. In this introductory chapter, we discuss the basics of surface plasmons and then present a background of several topics used along this thesis.

1.1 Fundamentals of surface plasmons

Surface plasmons can be generally catagerized into two group. They are, respectively, named surface plasmon polaritons (SPPs) that propagate on extended surfaces and localized surface plasmons (LSPs) that reside on isolated particles.

1.1.1 Surface plasmon polaritons

In a classical picture, electromagnetic phenonmena can be describled using Maxwell's equations, whose form in the frequency doman is [1] [20]

$$\begin{aligned}
\nabla \times \mathbf{E}(\mathbf{r},\omega) &= ik\mathbf{B}(\mathbf{r},\omega), \\
\nabla \times \mathbf{H}(\mathbf{r},\omega) &= -ik\mathbf{D}(\mathbf{r},\omega) + \frac{4\pi}{c}\mathbf{J}(\mathbf{r},\omega), \\
\nabla \cdot \mathbf{D}(\mathbf{r},\omega) &= 4\pi\rho(\mathbf{r},\omega), \\
\nabla \cdot \mathbf{B}(\mathbf{r},\omega) &= 0,
\end{aligned} \tag{1.1}$$

where $\mathbf{E}$ is the electric field, $\mathbf{H}$ is the magnetic field, $\mathbf{D}$ is the electric displacemnt, and $\mathbf{B}$ is the magnetic induction, which are all generally taking complex values. Also, ρ and $\mathbf{J}$ are charge and current densities, respectively, while $k = \omega/c$ is the light wave vector. The Maxwell equations tell us how the electromagnetic source shape the field. They should be complemented with the so-called constitutive relations, which describe the material response to the electromagnetic wave. The constitutive relations of most typical metals and dielectrics can be written as

$$\mathbf{D}(\mathbf{r},\omega) = \epsilon(\omega)\mathbf{E}(\mathbf{r},\omega),\ \mathbf{B}(\mathbf{r},\omega) = \mu(\omega)\mathbf{H}(\mathbf{r},\omega), \tag{1.2}$$

assuming the local approximation (*i.e.*, $\mathbf{D}$ and $\mathbf{B}$ are related to $\mathbf{E}$ and $\mathbf{H}$ at the same spatial location only), a relative permeability $\mu = 1$ for non-magnetic materials is considered throughout this thesis, which is an excellent approximation at optical frequencies. The relative permittivity ϵ is usually dependent on frequency. For

[1] Gaussian electromagnetic units are used throughout this thesis

metals, it can be approximated by the Drude model

$$\epsilon(\omega) = \epsilon_{\mathrm{b}} - \frac{\omega_{\mathrm{p}}^2}{\omega(\omega + i\gamma)}, \tag{1.3}$$

where ω_p is the plasmon frequency, γ is the electron collision rate, and ϵ_b accounts for the background dielectric response (*e.g.*, as produce by interband transitions in noble metals).

When we are going to solve the Maxwell equations involving more than one material domain, boundary conditions are needed. They bridge the electric and magnetic fields on two sides of the interface that seperate them. These conditions are

$$\begin{aligned} \mathbf{n} \times (\mathbf{E}_1 - \mathbf{E}_2) &= 0, \\ \mathbf{n} \times (\mathbf{H}_1 - \mathbf{H}_2) &= \frac{4\pi}{c}\mathbf{K}, \\ \mathbf{n} \cdot (\mathbf{D}_1 - \mathbf{D}_2) &= 4\pi\eta, \\ \mathbf{n} \cdot (\mathbf{B}_1 - \mathbf{B}_2) &= 0, \end{aligned} \tag{1.4}$$

where $\mathbf{K}$ is the surface current on the boundary, and the η is the surface charge density. Based on the boundary conditions, we can derive the Fresnel equations to compute the reflection and transmission coefficients for $p-$ and $s-$polarized light incident from medium 1 on a planar interface with medium 2 [21],

$$r_p = \frac{\epsilon_2 k_{1\perp} - \epsilon_1 k_{2\perp}}{\epsilon_2 k_{1\perp} + \epsilon_1 k_{2\perp}}, \; t_p = \frac{2\epsilon_2 k_{1\perp}}{\epsilon_2 k_{1\perp} + \epsilon_1 k_{2\perp}} \sqrt{\frac{\epsilon_1}{\epsilon_2}}, \tag{1.5}$$

$$r_s = \frac{k_{1\perp} - k_{2\perp}}{k_{1\perp} + k_{2\perp}}, \; t_s = \frac{2k_{1\perp}}{k_{1\perp} + k_{2\perp}}, \tag{1.6}$$

where $k_{i\perp}$ is the perpendicular component of the total wavevector $k_i = \sqrt{\epsilon_i}k$ in medium i. If we denote the common parallel component as $k_{\parallel}$, then they should satisfy the relation $k_{i\perp}^2 + k_{\parallel}^2 = k_i^2$.

SPPs are evanescent waves bounded at metal-dielectric interfaces. They are $p-$polarized and are identified from the zeros in the denominator of Eq. (1.5)

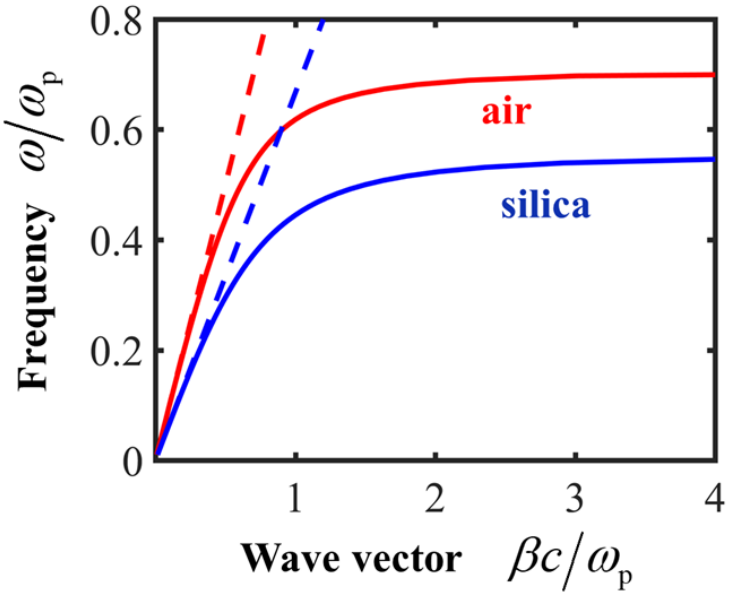

Figure 1.1: Dispersion relation of SPPs at the interface between a lossless Drude metal and air (red curve) or silica (blue curve).

(*i.e.*, infinite reflection in the absence of external field, implying a self-sustained resonance). Indeed, the dispersion relation can be worked out from the pole of the corresponding Fresnel equations:

$$\beta_{\mathrm{spp}} = \frac{\omega}{c}\sqrt{\frac{\epsilon_{\mathrm{m}}\epsilon_{\mathrm{d}}}{\epsilon_{\mathrm{m}}+\epsilon_{\mathrm{d}}}}. \tag{1.7}$$

Figure 1.1 displays the dispersion relations at two interfaces. One is between a metal and air ($\epsilon_d = 1$) as shown by the red curve, the other is between the same metal and silica ($\epsilon_d = 2.25$) as shown by the blue curve. The metal is described using the Drude model of Eq. (1.3) with $\epsilon_b = 1$ and $\gamma = 0$ (*i.e.*, lossless metal). The dashed lines are the light lines, and the solid curves represent the real parts of the wave vectors outside the light cones (*i.e.*, confined modes). One can see that the wave vectors of SPPs are always larger than that of light in free space with the same frequency, which hinders SPPs at a flat interface to be directly excited by external light. Decorating the interface with periodic structures can provide light with additional parallel wave vectors, therefore sorting out this problem. This will

be discussed in detail in chapter 2.1, where we periodically structure a gold film to change it from a good reflector to a perfect absorber.

Any real metal is lossy, so it can dissipate the propagating wave by transforming its electromagnetic energy into Joule heat in the metal. One can define a propagation length of a SPP as $L = 1/2\mathrm{Im}\{\beta_{\mathrm{spp}}\}$, which means that the intensity of the SPP decays by a factor of $1/e$ after travelling such a distance. For a long time in the past, it has been thought that the loss is an undesired effect. Then, gain material can be introduced to compensate the loss and improve the performance of plasmonic nanodevices. We discuss such an introduction of gain in a seperated section 1.5.

1.1.2 Localized surface plasmons

The surface plasmons can also be supported by nanoparticles, which localize the resonance in three dimensions. In contrast to the above-mentioned SPPs, the LSPs can directly couple to the external light, which is characterized by an enlarged extinction cross-section of the host structure on resonance. For the study of complex particles (*e.g.*, nanocubes [22], nanostars [23]), we usually need to rely on numerical calculations using for example the boundary element method [24] or finite element methods [25]. For the simple homogeneous nanosphere, we can analytically solve the Maxwell equations using Mie theory, which was established by Gustav Mie in 1908. The spirit of the theory is to decompose the incident field as well as the scatterred field into an infinite series of vector harmonics, and compute the scattering coefficient of each harmonic at the spherical interface according to the boundary conditions 1.4.

Specifically, we can obtain the extinction cross-section of a nanosphere with radius a in air as [26]

$$\sigma^{\mathrm{ext}} = \frac{\lambda^2}{2\pi}\sum_{l=1}^{\infty}(2l+1)\left[\mathrm{Im}\{t_l^E\} + \mathrm{Im}\{t_l^M\}\right], \tag{1.8}$$

where l labels orbital angular momentum taking interger values from 1 to infinity. The electric and magnetic scattering coefficients, respectively, read as

$$t_l^{\mathrm{E}} = \frac{\epsilon_i j_l(k_i a)[j_l(ka) + kaj_l'(ka)] - j_l(ka)[j_l(k_i a) + k_i a j_l'(k_i a)]}{ih_l^{(1)}(ka)[j_l(k_i a) + k_i a j_l'(k_i a)] - \epsilon_i j_l(k_i a)[ih_l^{(1)}(ka) + ikah_l^{(1)\prime}(ka)]}, \tag{1.9}$$

$$t_l^{M} = \frac{kaj_l'(ka)j_l(k_i a) - k_i a j_l(ka)j_l'(k_i a)}{ik_i a h_l^{(1)}(ka)j_l'(k_i a) - ikah_l^{(1)\prime}(ka)j_l(k_i a)}, \tag{1.10}$$

where ϵ_i is the relative permittivity of the particle. $k_i = \sqrt{\epsilon_i}k$. j_l and $h_l^{(1)}$ are Bessel and Hankel functions, respectively. The primes represent their derivatives with respect to the arguments. This can be further generalized to deal with multilayer nanospheres. The method is presented in Appendix A, which is used for the works discussed in Chapter 3.

When the size of the nanoparticle is in the deep subwavelength scale, the so-called electrostatic approximation becomes valid. Then, the light speed c can be regarded to be infinitly large in the Maxwell equations. Additionally, in the small particle limit, the dipolar resonance with orbital angular momentom $l = 1$ dominates the optical response. The polarizability of the induced electric dipole of the nanosphere is directly related to the lowest order of the electric scattering coefficients as $\alpha = 3t_1^{\mathrm{E}}/(2k^3)$ (see Appendix A). Combined it with the expression of t_1^{E}, one finds $\alpha^{\mathrm{es}} = a^3(\epsilon_i - 1)/(\epsilon_i + 2)$. It is important to recall that this polarizability in electrostatic approximation does not include the self-interaction part, *i.e.*, the particle does not interact with the field radiated by itself. It can be amended via incorporating the imaginary part of self interaction Green tensor [27], as discussed in detail in Appendix E.

Compared with the simple nanospheres, the resonant frequency of dielectric/metal coreshell nanoparticles can be tuned over a wider range and in a easier way by changing the ratio of metal shell thickness to the dielectric core radius. As an example, we present in Fig. 1.2 the normalized extinction cross-sections of coreshell nanospheres with varying ratios. The core is silica ($\epsilon_{\mathrm{d}} = 2.25$), the shell is gold described using experimental data [28]. One can observe that the resonant frequency is highly tunable from visible to near-infrared (NIR) range. The inset confirms that

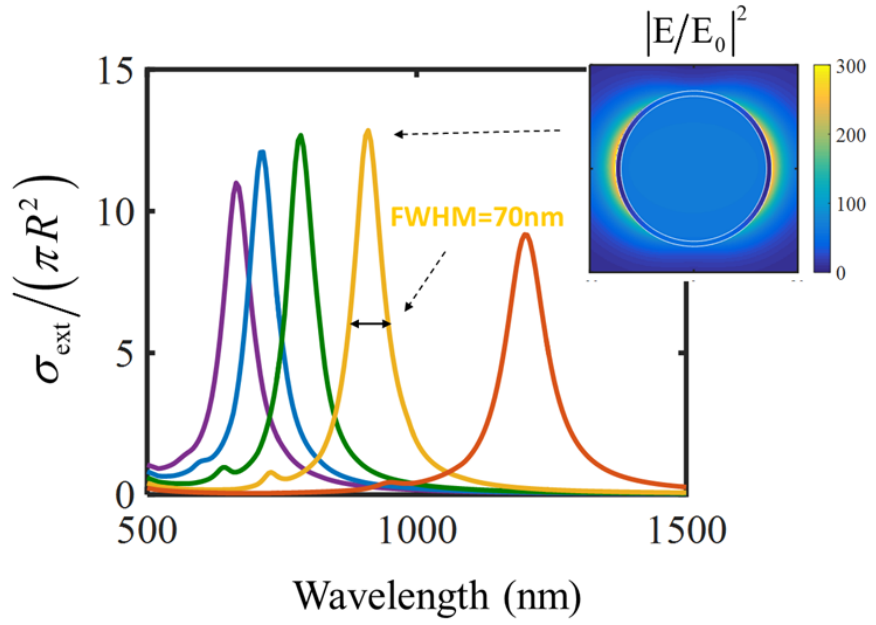

Figure 1.2: Normalized extinction cross-sections of silica/gold coreshell nanospheres with the same total radius $R = 60\,\text{nm}$, but different gold shell thicknesses. The corresponding thicknesses from left to right are 10 nm, 8 nm, 6 nm, 4 nm, 2 nm, respectively. Inset: Electric field intensity enhancement at resonance for one of the structures.

the resonance is dominated by a dipolar mode.

The confined near-field energy is partially emitted back to the far field, while the remaining part is dissipated as Joule heat in the metal. It can locally increase the temperature, causing a photothermal effect. An introduction of the effect is presented in section 1.3. A detailed study of the effect in complex structures is included in Chapter 3. Besides, one can also note from Fig. 1.2 that the typical FWHM of the spectra is dozens of nanometers in the investigated range, which leads to a relatively low Q factor. This can be addressed by incorporating a gain medium into the structures, as we discuss in section 2.2.

1.2 Selective light absorption

The reflection spectra of opaque flat metal films are totally determined by their intrinsic material properties. The typical plasmonic metals (*e.g.*, gold, silver, copper) show high reflection in the visible and longer wavelength ranges. When properly structuring the metal or metallodielectric hybrid films at subwavelength scales, transforming them into periodic arrays of optical antennas, the reflections can be largely reduced even down to zero, leading to perfect absorption at desired frequencies [29]. This phenomenon, in macroscopic electromagnetic theory, can be understood in terms of impedance matching. The impendance of a material is defined as $z(\omega) = \sqrt{\mu/\epsilon}$. Recent research into metamaterials has shown that the relative permittivity ϵ and the relative permeability μ, which characterize, respectively, the electric and magnetic responses, can be tailored by engineering corresponding electromagnetic resonances held by the antenna [30]. At some critical point, the impedance of the structure surface can be tuned to be equal to that of free space, which is unity. The perfect absorption effect can also be explained using coupled-mode theory [31]. A absorber without diffractive orders can also be regarded as a one-port resonator. The energy stored in the resonance mode is partially coupled to far field described by a radiative decay rate γ_{rad}. The remaining part is lost as heat described by resistive decay rate γ_{res}. Complete absorption is achieved when they are equal [32]. This will be further explained in Chapter 2.1.

In 2008, Padilla's group reported a metamaterial absorber at GHz frequency [33]. The right panel of Fig. 1.3(a) shows a unit cell and incident electromagnetic

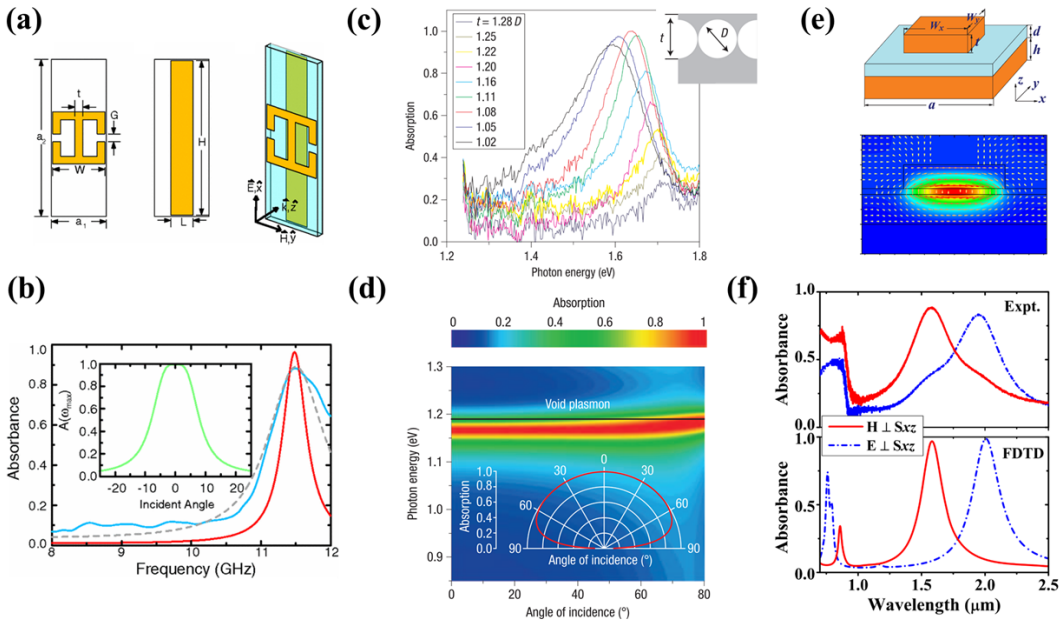

Figure 1.3: Three representive perfect absorbers. A perfect absorber operating in the GHz region (a,b) [33]. An omnidirectional absorber based on void plasmons (c,d) [34]. An absorber utilizing a typical metal-insulator-metal configuration (e,f) [16]. (a) From left to right are an electric resonator, a cut wire, and an unit cell. (b) Simulated (red curve) and experimental (blue curve) absorbance under normal incidence. Inset: Dependence of simulated on-resonance absorbance on incident angles. (c) Measured absorption spectra of mesoporous gold surfaces with different thicknesses under normal incidence. Inset: A sketch of the sample. (d) Absorbance as a function of incidence angle and wavelength. (e) A sketch of a unit cell of the absorber (upper panel) and magnetic field distribution at resonance (lower panel) (f) Experimental (upper panel) and simulated (lower panel) absorption spectra under normal incidence with different incident light polarizations.

wave. The unit cell is composed of an electric ring resonator (ERR) (left panel) and a cut wire (middle panel). The ERR supplies electric coupling, while the anti-parallel current supported by the center wire of the ERR and the cut wire supplies magnetic coupling. In this way, the authors were able to independently tune effective ε and μ parameters by varying geometry of the two elements and the distance between them. Figure 1.3(b) displays its nearly perfect absorption under normal incidence in simulations. The inset shows the angular tolerance of the high absorption. In the same year, García de Abajo and colleagues realized omnidirectional light absorption in vis-NIR regime using mesoporous gold surfaces [34]. The structure is depicted in the inset of Fig. 1.3(c). Silica-filled inclusions are buried in gold films to hold void plasmons [35], which can efficiently couple to external light with broad incidence angle. Figure 1.3(c) and (d), respectively, demonstrate absorption spectra of various geometries under normal incidence and absorption spectra of a certain geometry under broad-angle incidence. A high-performance angle-robust aborption can be also achieved in metal-insulator-metal (MIM) configurations. The upper panel of Fig. 1.3(e) is one of early MIM absorbers proposed by Qiu's group [16]. The light absorption is mediated by a remarkable magnetic resonance, which is characterized by a strongly localized magnetic field (color map) and circulating displacement current (white arrows) in the lower panel. Compared with the spherical-voids structure, this lithographically fabricated rectangular nanoparticles provides additional opportunities for manipulating absorption of orthogonal polarized light waves independently. Figure 1.3(f) illustrates numerical and experimental studies of this effect.

Absorbers working in the middle infrared (MIR) range are of great interest, especially for applications in sensing of molecular vibrational bands [36]. In this context, graphene plasmons have raised huge expectations owing to their outstanding optical properties in this spectral range [37, 38]. Perfect absorption has been demonstrated both theoretically [39] and experimentally [40]. Thanks to the unique linear dispersion around the Dirac point, graphene-based absorbers often owns an advantage of electrical tunability, which constitutes an important asset of dynamic absorbers. Apart from graphene, other active materials like phase-change media (*e.g.*, GST) [41] and gain media (*e.g.*, dye molecules, quantum dots) [42] can also contribute to the realization of dynamic absorbers. We discuss such cases in section 2.2.

The absorbers mentioned above are named narrow band absorbers. In the vis-

NIR regime, the Q ($= \lambda_0$/FWHM) factors of their absorption spectra are typically on the order of ten. There are other two trends in absorber design: (i) Trying to maximize the bandwidth to realize broadband absorption. Common strategies include combining multiple resonances into a single sub-wavelength unit cell [43, 44] and adiabatically nanofocusing light by anisotropic metamaterials [45, 46]. The broadband absorbers can benefit solar energy harvesting by improving the efficiency of photovoltic cells [47]. (ii) Trying to minimize the bandwidth to realize ultranarrow band absorption. Common strategies are utilizing lattice resonances [48, 49, 50] or guided modes [18, 51]. Ultranarrow band absorbers find potential applications in plasmon-based photodetection [52] and sensitive sensing [53]. We present several novel ultranarrow band absorbers in Chapter 2 and expolit their application in sensing.

Incidentally, as a consequence of Kirchhoff's law, light absorbers can also be regarded as selective thermal emitters [54]. A remarkable phenomenon is that the thermal radiation can be tailored to become highly spatially and temporally coherent [55]. We demonstrate it using an ultranarrow band absorber in section 2.1.

1.3 Photothermal effects

As illustrated in the previous section, properly designed metal nanostructures display remarable selective light absorption mediated by plasmon resonances. The energy of the absorbed photons is turned into Joule heat, which induces a local temperature increase [56]. This photothermal effect has been generaly regarded as a drawback of the plasmon resonance, especially in terms of applications to optical signal processing [57]. In past decades, however, advantages of the effect in potenital applications have been realized, such as for photothermal therapy [58, 59], nanosurgery [60, 61], photothermal imaging [62, 63], plasmon-assisted nano-chemistry [64, 65], plasmon-assisted, and optofluidics [66, 67], just name a few. They mainly benefit from two appealing features: (i) The optically generated thermal energy is highly confined in the vicinity of structures, and therefore a moderate incidence light power can induce considerable local temperature increase. (ii) Thanks to the ultrafast response of plasmons to external light, as well as small thermal diffusion distance involved, the heating process is also very fast.

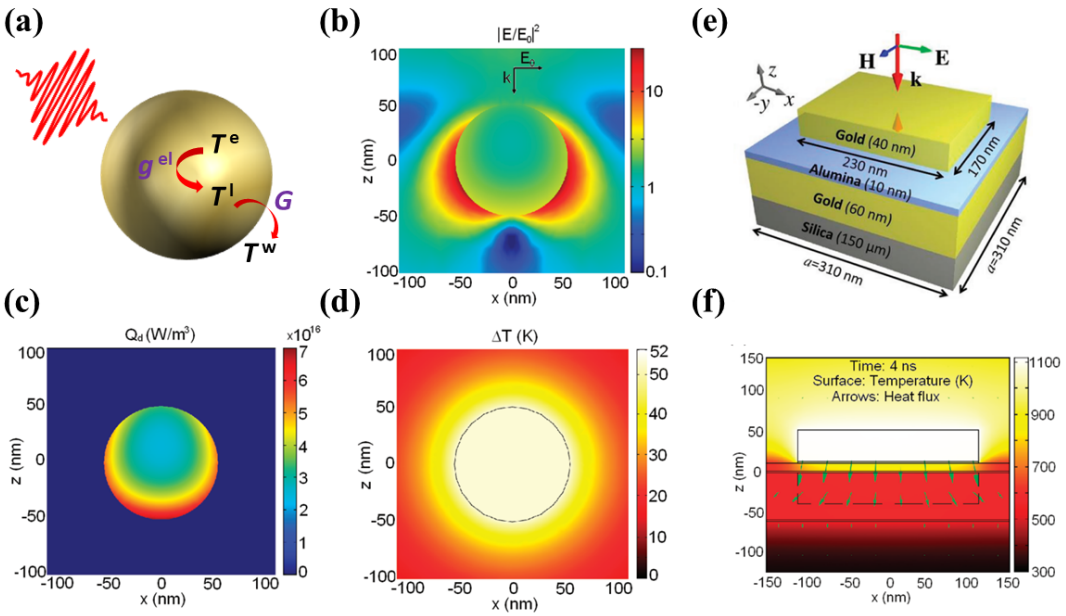

Figure 1.4: (a) A schematic view of energy flow in the photothermal effect of a metal nanosphere. (b,c,d) Photothermal effect of a gold nanosphere with 50 nm radius in water. The incident cw light wavelength is 530 nm, and the power intensity is $1\text{mW}/\mu\text{m}^2$. (b) Normalized electric field intensity. (c) Heat power density. (d) Temperature distribution. (e,f) Transient photothermal effect of a lithographic MIM absorber. The pulse source has a repetition rate of 25 kHz, and a pulse duration of 2.6 ns. (e) Geometric structure of a single absorber unit cell. (f) Temperature distribution at 4 ns after irradiation. (b-f) are adapted from [68].

Figure 1.4(a) illustrates basic energy flow steps happening when external light excites a nanostructure. Here, we take a gold nanosphere in water as an example. When a pulse incidents on the structure, within the first approximately 100 fs, the free electron gas partially absorbs light energy and quickly thermalizes to a Fermi-Dirac distribution. The temperature is denoted as T^{e}. The temperature of ion lattice (T^{l}), which has a larger heat capacity because it involves the motion of heavier objects (the ions), remains unchanged. In the next step (100 fs to 10 ps), the hot electrons thermize the ion lattice mediated by the volumetric transfer coefficient g^{el}. The transferred power is $P = g^{\text{el}}V(T^{\text{e}} - T^{\text{l}})$, where $V = (4/3)\pi R^3$ is the particle volume. Finally, the thermal energy diffuses into surrounding medium, heating the environment. However, this process is damped by the thermal boundary

conductance (TBC) (also called Kapitza conductance) [69], denoted by G. The TBC exists at a interface between two adjacent media, and causes a temperature discontinuity $(T^{\mathrm{l}} - T^{\mathrm{w}}) = P/(GS)$, where T^{w} is temperature of the water at the particle surface, and $S = 4\pi R^2$ is particle surface area. We investigate the effect of the TBC in detail in section 3.2. Generally speaking, the value of the TBC can be sensitive to the quality of the interface. It can become large if the liquid does not wet the particle surface or when coating the surface with hydrophobic molecules. Under excitation with cw light, these three steps occur as well, but in a steady-state manner. In steady state, the electrons and the ion lattice are usually regarded as in thermal equlibrium (*i.e.*, $T^{\mathrm{l}} = T^{\mathrm{e}}$) because of the large electron-lattice coupling strength g^{el}. Additionally, because the thermal conductivity of metal (*i.e.*, $\kappa_{\mathrm{gold}} = 318\,\mathrm{W\,m^{-1}\,K^{-1}}$) is much larger than that of liquid (*i.e.*, $\kappa_{\mathrm{water}} = 0.6\,\mathrm{W\,m^{-1}\,K^{-1}}$), the temperature in the metal can be considered as uniform.

Figure 1.4(b-d) displays such an example [68] without including TBC. A gold nanosphere in water is illuminated by cw light (see caption for details). Figure 1.4(b) shows the normalized electric field intensity. In order to maximize light absorption, the size of the particle needs to be engineered to make the frequency of dipolar resonance match that of incident light. Figure 1.4(c) illustrates the heat power density, which reads

$$Q(\mathbf{r}) = \frac{\omega}{2\pi}\mathrm{Im}\left\{\epsilon(\mathbf{r},\omega)\right\}\left|\mathbf{E}(\mathbf{r})\right|^2, \tag{1.11}$$

Figure 1.4(d) shows the temperature distribution pattern, as obtained by solving the thermal diffusion equation

$$-\nabla\cdot\left[\kappa(\mathbf{r})\nabla T(\mathbf{r})\right] = Q(\mathbf{r}), \tag{1.12}$$

The temperature increase in the nanoparticle is

$$\Delta T_{\mathrm{NP}} = \frac{Q_{\mathrm{tot}}}{4\pi\kappa_{\mathrm{water}}R}, \tag{1.13}$$

where Q_{tot} is the volume integration of the heat power density in the metal nanoparticle. It can be also expressed as $Q_{\mathrm{tot}} = \sigma_{\mathrm{abs}}I$, where σ_{abs} is the absorption cross-section of the particle, and I is the incident light intensity. Outside the

particle, ΔT decreases as $\Delta T(r) = (R/r)\Delta T_{\mathrm{NP}}$, where r is the distance to the particle center. Although there are analytical solutions for spherical structures, we have to rely on numerical simulations for other more complex ones. Rods, trangles, disks, ellipsoids, rings, stars [70, 71] among other many various structures have been studied. Actually, it has been found that the spherical structure is not the most efficient heater. A general design rule is that structures should be made flat, elongated, or sharp to let incoming light penetrate more easily into the structure, making the whole material involved in heating [70].

Compared with cw light, pulsed light can confine the generated heat more strongly in the near-field, therefore providing a larger temperature gradient [72]. Figure 1.4(e,f) shows such a study [68]. Figure 1.4(e) sketches a single unit cell of a typical MIM absorber. A supercontinuum light with wavelength range from 500 to 2400 nm (see details in caption) normally illuminates on the structure. Figure 1.4(f) is the simulated transient temperature distribution at 4 ns after pulse initiation. We can observe that the temperature difference in the nanoscale can reach hundreds of Kelvin (possibly leading to melting).

A high temperature can induce considerable local thermal stress, which has been experimentally exploited to be utilized to make a nanobomb as an alternative method to kill cancer cells [73, 74]. Then, a natural question arises: Can we design some nanostructure that sustains large temperature inhomogeneity at the nanoscale associated with an extreme hotspot under cw light excitation? We address this issue by using an optimized multilayer nanosphere, which is presented in Chapter 3.

1.4 Particle arrays

Light scattering on a single spherical nanoparticle can be described using Mie theory. Its basic optical and photothermal properties have been briefly introduced in the above sections. Arraging particles into a regular array brings about novel phenomena, which originate from coherent optical interaction among them [75]. The basic physics is presented in the following [27]. For simplicity, we consider 2D square arrays made of identical dielectric particles. The particles are small compared with both the wavelength and the lattice constant. So, only dipole-dipole interaction is involved. Calculations show that perfect reflection can be achieved for dilute arrays.

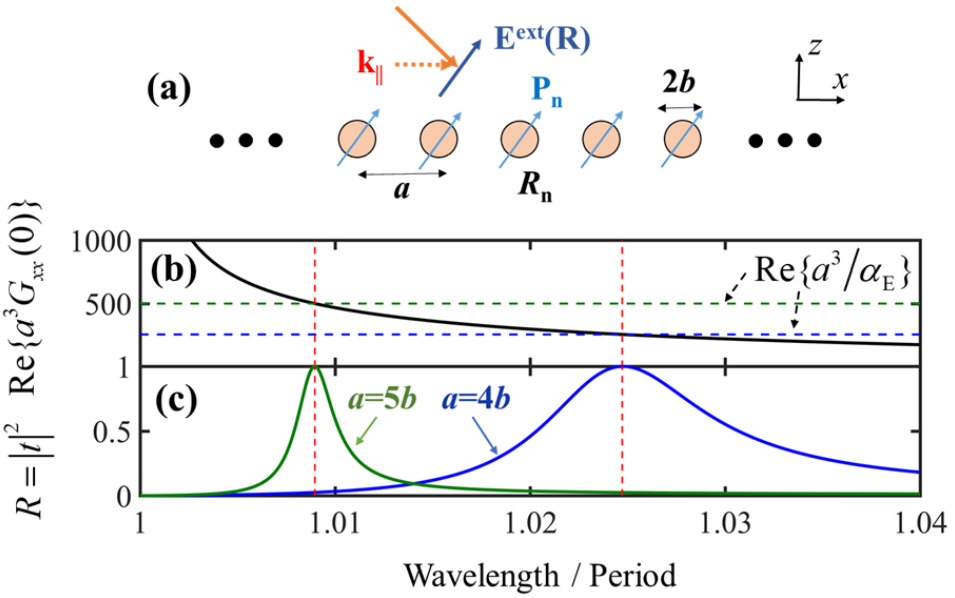

Figure 1.5: (a) A sketch of an infinite 2D particle array illuminated by a plane wave. $\mathbf{k}_{||}$ is the wave-vector component parallel with the array. The plane wave induces a dipole moment $\mathbf{p}_n$ of the particle at position $\mathbf{R}_n$. The lattice constant and particle radius are, respectively, denoted as a and b. (b) The real part of normalized lattice sum $\mathrm{Re}\{a^3 G_{xx}(0)\}$ as a function of normalized wavelength (solid black curve). The real parts of normalized reciprocal value of polarizability $\mathrm{Re}\{a^3/\alpha_{\mathrm{E}}\}$ with $a = 5b$ (green horizontal dashed line) and $a = 4b$ (blue horizontal dashed line). (c) Reflectance of the two arrays. The curves use the same color code as the two horizontal dashed lines in (b).

Figure 1.5(a) shows the configuration of the system under consideration. An external plane wave is incident on the particle array. The optical response of a particle can be represented by an induced electrical dipole p. The dipole feels the electric field of the external light wave plus those coming from all the other dipoles. For example, the dipole moment $\mathbf{p}_n$ at the particle occupying the position $\mathbf{R}_n$ is written as

$$\mathbf{p}_n = \alpha_{\mathrm{E}} \left[\mathbf{E}^{\mathrm{ext}}(\mathbf{R}_n) + \sum_{n' \neq n} \mathcal{G}(\mathbf{R}_n - \mathbf{R}_{n'}) \mathbf{p}_{n'} \right], \tag{1.14}$$

where $\alpha_{\mathrm{E}} = 1/(1/(\alpha_{\mathrm{E}}^{\mathrm{es}}) - 2\mathrm{i}k^3/3)$ is the polarizability of the dielectric particle. $\alpha_{\mathrm{E}}^{\mathrm{es}} = b^3(\varepsilon-1)/(\varepsilon+2)$ is the electrostatic part. For simplicity and concreteness, we assume $\varepsilon = 2$. The first term inside the square bracket is the external field $\mathbf{E}^{\mathrm{ext}}(\mathrm{R}_n) = \mathbf{E}^{\mathrm{ext}}\exp(\mathrm{i}\mathbf{k}_{||} \cdot \mathbf{R}_n)$. The second term captures the electromagnetic interactions among the particles. $\mathcal{G}$ is the dipole-dipole interaction tensor, whose explicit form is $\mathcal{G}(\mathbf{r})\mathbf{p} = [\exp(\mathrm{i}kr)/r^3]\{[(kr)^2 + \mathrm{i}kr - 1]\,\mathbf{p} - [(kr)^2 + 3\mathrm{i}kr - 3]\,(\mathbf{r}\cdot\mathbf{p})\mathbf{r}/r^2\}$. The solution of Eq. (1.14) should have the form $\mathbf{p}_n = \mathbf{p}\cdot\exp(\mathrm{i}\mathbf{k}_{||}\cdot\mathbf{R}_n)$ based on Bloch's theorem. Substituting this into Eq. (1.14), we have

$$\mathbf{p} = \frac{1}{1/\alpha_{\mathrm{E}} - G(\mathbf{k}_{||})}\mathbf{E}^{\mathrm{ext}}, \tag{1.15}$$

where $G(\mathbf{k}_{||}) = \sum_{n\neq 0}\mathcal{G}(\mathbf{R}_n)\exp(-\mathrm{i}\mathbf{k}_{||}\cdot\mathbf{R}_n)$ is a so-called lattice sum. Then, the reflected field is just the sum of the fields coming from all the dipoles. Here, we assume the external light is normally incident on the array, so that all the dipoles are oriented along the x axis. Besides, we focus on a wavelength range such that $\lambda > a$. So, only specular reflectance goes to far field. Thus, we reach the reflection coefficient as $r = (2\pi\mathrm{i}k/a^2)/(1/\alpha_{\mathrm{E}} - G_{xx}(0))$ (see section 4.2 for a detailed derivation). The computation of the real part of the lattice sum has to rely on numerical methods [76]. While the imaginary part has an analytical expression as $\mathrm{Im}\{G_{xx}(0)\} = 2\pi k/a^2 - 2k^3/3$ [27]. Finally, we get a straightforward formula of r as

$$r = \frac{-1}{1 + (\mathrm{i}a^2/2\pi k)\mathrm{Re}\{1/\alpha_{\mathrm{E}} - G_{xx}(0)\}}, \tag{1.16}$$

and the transmission coefficient $t = 1 + r$ [39], absorbance $A = 1 - |t|^2 - |r|^2$.

One can observe from Fig. 1.5(b,c) that total reflection can be achieved when $\mathrm{Re}\{a^3/\alpha_{\mathrm{E}}\}$ cancels $\mathrm{Re}\{a^3 G_{xx}(0)\}$. Because the value of the real part of the lattice sum approaches infinitely large when the wavelength goes close to the period. So, the perfect reflection can be always realized no matter how small the particle is. The differene is the peak will become narrower and narrower.

Replacing the dielectric nanoparticles with metal ones might be more appealing due to very fascinating features of plasmonic metal nanoparticle arrays in terms of both far field and near-field optical responses. In terms of far field, the imaginary

part of the lattice sum can become negative to partially cancel the single particle natural width [77], which results to dramatically reduced bandwidths of spectra. This can benefit refractive sensing [78]. In terms of near-field, plasmonic particle arrays combine desirable attributes of both photonic and plasmonic systems, *i.e.*, high near-field enhancements in large spatial extension with long lifetimes [79]. The highly enhanced fields are exploited for several applications, such as shape the fluorescent emission [80], achieve strong coupling with molecules [81], enhance SERS responses [82], improve light outcoupling in solid-state lighting [83], and plasmonic laser realization [84]. Incidentally, we want to point out that as a consequence of Babinet principle, reflection of a particle array is equal to transmission of its complementary hole array with orthogonal polarization. So, the same coupled dipole approximation theory also explains enhanced optical transmission of metal screens with hole arrays [85], which triggered a boost of the field of surface plasmons twenty years ago.

We have shown that properly designed dielectric nanoparticle arrays can totally reflect incident light. The same phenomenon can also be realized using 2D atom arrays with their seperations on the order of wavelength [86]. This interest in part comes from a long-standing goal that people want to enhance interaction between a flying photon and a localized quantum bit (*e.g.*, an atom), which is vital for quantum information processes. The intrinsic interaction is very small because of a big mismatch between wavelength and atom size. To this end, various methods have been developed including tightly focusing the light beam [87] and placing the atom inside a high fitness cavity [88]. In very recent years, it is found that the efficient coupling can also be reached by properly arranging atoms into regular 2D arrays [89, 86]. The physics behind lies in cooperative resonances similar to those in the nanoparticle case. Take a 2D square two-level atom array as an example. The electrostatic polarizability of the atom is $\alpha_{\mathrm{E}}^{\mathrm{es}}(\omega) = (2d^2\omega_0/\hbar)/(\omega_0^2 - \omega^2 - \mathrm{i}\gamma\omega)$, where d is dipole matrix element, ω_0 is transition angular frequency of the two-level atom, and $\gamma \approx 0$ denotes nonradiative decay rate from excited state to ground state. When the detuning $\delta = \omega - \omega_0$ is zero, we have $\mathrm{Re}\{1/\alpha_{\mathrm{E}}(\omega_0)\} = \mathrm{Re}\{1/\alpha_{\mathrm{E}}^{\mathrm{es}}(\omega_0)\} = 0$. Combining it with Eq. (1.16), one obtain $r = 1$, when $G_{xx}(0) = 0$. The condition is satisfied when the ratio of lattice constant to wavelength is approximately 0.2 or 0.8. This is the key result in [86]. In Chapter 4, we present a study of light

scattering of 2D three-level atom arrays, showing that both large light absorption and amplification can occur and be manipulated.

1.5 Gain media

Typical plasmonic materials (*e.g.*, gold and silver) suffer from considerable dissipative losses especially in optical wavelength regimes. Incorporating gain media into the plasmonic structures constitutes a way to address the problem. The most simple way to describe a gain medium is to use a negative value of the imaginary part of its refractive index [90]. A more advanced approach, which includes dispersive effect, is to add an additional Lorentzian term to the dielectric response of the doped elements [91] (see details in section 2.2). If we want to go down to a microscopic picture of the gain medium, we need to describe active emitters (*e.g.*, dye molecules, quantum dots) quantum-mechanically. For example, equations of motions of polarization and population densities of the active emitter can be coupled to Maxwell's equations to form self-consistent equation systems and be solved numerically using finite-difference time-domain algorithms. The method are extensively used to study spatio-temporal resolved properties of amplification and laser systems [92, 93, 94, 95, 96, 97, 98, 99, 100], while their derivations are typically not presented in the publications. We show the detailed derivations in Appendix D, which provides in-depth insights of the light-matter interaction processes and the origin of gain. Wherein, we adopt 4-level system, in line with many aforementioned publications. In the following, we introduce one example [95] of its amplications.

Figure 1.6(a) shows the studied configuration. Two perforated silver films are embedded in a dielectric host material, which holds the four-level dye molecules (Rhodamine 800 dye). In the numerical experiment, a single unit (indicated by the white frame) of the periodic structure is firstly excited by a short and intense pump pulse (red line) of duration 2 ps. Then, after 7 ps short delay, a weak broadband probe pulse (blue line) of duration 12 fs is illuminated onto the structure. Standard retrieval method [30] is used to compute its effective refractive indices $n = n' + \mathrm{i}n''$ for various peak pump-field amplitudes (Fig. 1.6(b)). Also calculated are the absorption and the FOM$=-n'/n''$ (Fig. 1.6(c,d)). One can observe that when the pump strength continues to grow up and exceeds a threshold, n'' becomes negative

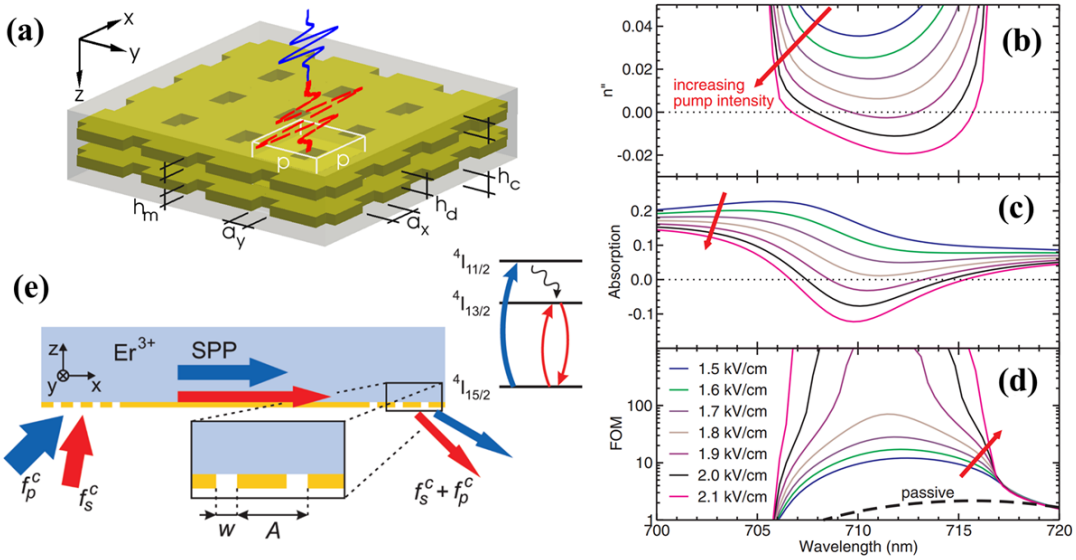

Figure 1.6: (a) A sketch of the double-fishnet structure. Transparent grey part is a dielectric containing dye molecules. Red and blue lines, respectively, represent pump and probe light. (b,c,d) The imaginary part of the effective refractive index (b), the absorption (c), and the FOM (d) for different peak pump-field amplitudes as shown in (d). (e) A sketch of the configration for SPP-SPP modulation. The inset is a diagram of optically active states of an Er^{3+} ion. The plots (a-d) are taken from [95]. The plot (e) is taken from [101].

(Fig. 1.6(c)), when the system amplifies the probe light (Fig. 1.6(d)).

Apart from compensating the intrinsic losses to improve qualities of plasmonic devices (*e.g.*, see Fig. 1.6(c)), gain also introduces versatile functionalities in different fields including nanolasing [102], slow light [103], optical switching [104], absorption enhancement [105], and all-optical computing [106]. Especially, in the work discussed in Ref. [105], the authors investigated the absorption of metal nanoparticles coated with gain dielectric shells. The theoretical results show that the absorption can be largely enhanced when the gain strength is increased to partially compensate the large intrinsic loss of metal core. In section 2.2, we step further to utilize gain but combined with high-order optical modes to realize ultranarrow band absorption.

Gain media can also be used for optical signal modulations. Figure 1.6(e) show such an example of SPP-SPP modulation [101]. A planar metal surface is covered by a dielectric layer doped with Er^{3+} ions, whose optically active states form a three-level system (see inset). Two sets of gratings are etched at the two ends for in-couplings and out-couplings of both pump (blue arrows) and signal (signal arrows) SPPs. The population inversion between the states of $^4I_{13/2}$ and $^4I_{15/2}$, therefore the transmitted power of the signal SPPs, can be controlled through tuning the power of the pump SPPs. In chapter 4, we arrange this kind of three-level atoms into regular periodic arrays, and study optical modulation performance of these arrays free standing in air.

Chapter 2

Ultranarrow band absorbers

In this chapter, we present studies of two kinds of ultranarrow band absorbers and exploit their applications in sensing and thermal emission. One relies on delocalized resonances, while the other relies on localized resonances. In the first section, lamellar gratings are investigated via temporal coupled-mode theory and numerical simulations. Total absorption can be achieved by an optimized grating with shallow grooves under normal incidence and the FWHM is only 0.4 nm. For certain wavelengths, the structure shows high absorption only within an ultra-narrow angle, which suggests that it can be used as a highly directional thermal emitter according to Kirchhoff's law. Besides, the resonant wavelength is sensitive to the refractive index of the environmental dielectric. The large sensitivity (S=1400 nm/RIU) and simultaneous small FWHM result in a huge figure-of-merit (FOM=S/FWHM) of 2300 /RIU, which enables the structure to have great potential in plasmonic sensing. In the second section, We demonstrate the viability of using high-order modes in a localized optical resonance combined with a gain medium to dramatically reduce the linewidth of absorption spectra. Our theoretical study provides a rational design route for small footprint absorption with high quality factor, which is typically a tradeoff for plasmonic light absorbers. Specifically, we design and numerically investigate a MIM absorber coupled to a graphene Salisbury screen. We also study the potential application for sensing and achieve high performance compared with conventional sensors based on the fundamental mode. Our approach, which can readily operate in multiplex mode, has potential for sensing minute amounts of

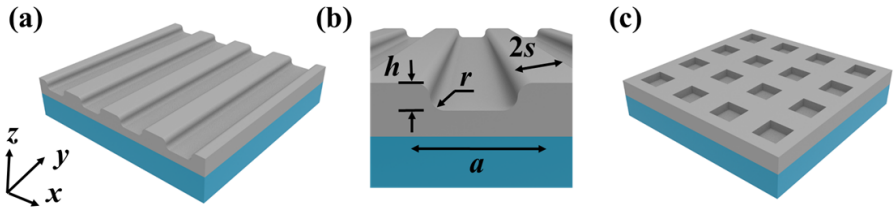

Figure 2.1: (a) Schematic of the 1D grating. The grey region is silver and the blue region is the substrate. (b) Cross-section of a unit cell, s represents half of the grating ridges, h denotes the depth of the grooves, $r = h/2$ is the radius of the fillets, and a is the period. (c) 2D crossed-grating extended from the 1D grating.

analytes with a high FOM.

2.1 Absorbers relying on delocalized resonances

In this section, we present a study that utilize guided modes supported by metal gratings to achieve ultranarrow band absorptions. Although grating is an old structure [107], it remains a hot topic even to date. Both broadband and narrowband absorption can be realized by varying grating's composites and geometrical profiles [108, 109, 110, 111]. Sharon *et al.* [108] proposed a grating-waveguide structure. A dielectric waveguide is superimposed on metal. Light confined in the waveguide is diffracted by grating upon it. A bandwidth of 0.1 nm is reported. In Ref. [112], the authors designed a tungsten grating with shallow grooves, which is demonstrated as a highly directional thermal emitter. The similar structures can be also regarded as light absorbers. Here, by directly constructing grating on a silver surface, a simpler absorber is designed with a subnanometer bandwidth. The resonant wavelength is easily tunable via geometrical scaling and ultrasensitive to the refractive index of the environmental dielectric.

The grating is superimposed on a substrate as illustrated in Fig. 2.1(a). Figure 2.1(b) shows its cross-section of a unit cell, where s, h, and a represent half of the grating ridges, the depth of the grooves, and the period, respectively. Note that absorbers based on onedimensional (1D) gratings are polarization-sensitive.

However, absorbers based on two-dimensional (2D) crossed-gratings, extended from the 1D gratings as shown in Fig. 2.1(c), are polarization insensitive. Here, we focus mainly on the 1D gratings as the results for the 2D crossed-gratings are qualitatively similar. In the following numerical calculations using commercial software COMSOL based on finite element methods, right angles are modified to fillets, whose radii are $r = h/2$, to avoid singular points and to consider practical fabrication process. The silver permittivity is taken from the experimental data by Johnson and Christy [28]. Only the TM wave (the magnetic field is parallel to the grooves) is considered here. Under light illumination with proper wavelength, SPPs will be excited. The energy of the excited surface wave is partially dissipated in metal as resistive heat described by resistive damping rate γ_{res}, and the other is coupled into free space in the form of radiation denoted by the radiative damping rate γ_{rad}. Both of γ_{res} and γ_{rad} can be varied by adjusting the geometrical parameters of the grating. The radiation coupled from SPPs will interact with light directly reflected from the metal surface, which determines reflectance, therefore absorbance of the grating, since the transmittance is zero. In the following, a time-saving approach based on temporal coupled-mode theory is first introduced and utilized to optimize geometrical parameters of the absorber. Then numerical simulations, which include incident light and require frequency scanning, are used to investigate the optimized absorber.

The temporal coupled-mode theory [113, 114, 32] provides an insightful analysis to the absorbance of nanostructure. In order to evaluate γ_{rad} and γ_{res}, we use the two-step method in [113, 114]. We start with the lossless case by assuming the imaginary part of silver permittivity to be zero. Computed complex eigenfrequency $\omega_0 + \mathrm{i}\gamma_{\mathrm{rad}}$ contains two parts, where ω_0 is the resonant angular frequency and γ_{rad} is the radiative damping rate. We then introduce metal loss by describing the silver with realistic permittivity. In this case, obtained complex eigenfrequency is $\omega_0 + \mathrm{i}\gamma_{\mathrm{tot}}$, where γ_{tot} is the total damping rate, which includes both the radiative and the resistive damping rates. The resistive damping rate is then obtained from $\gamma_{\mathrm{res}} = \gamma_{\mathrm{tot}} - \gamma_{\mathrm{rad}}$. The absorbance at angular frequency ω is given by [32]

$$A = \frac{4\gamma_{\mathrm{rad}}\gamma_{\mathrm{res}}}{(\omega - \omega_0)^2 + \gamma_{\mathrm{tot}}^2}. \tag{2.1}$$

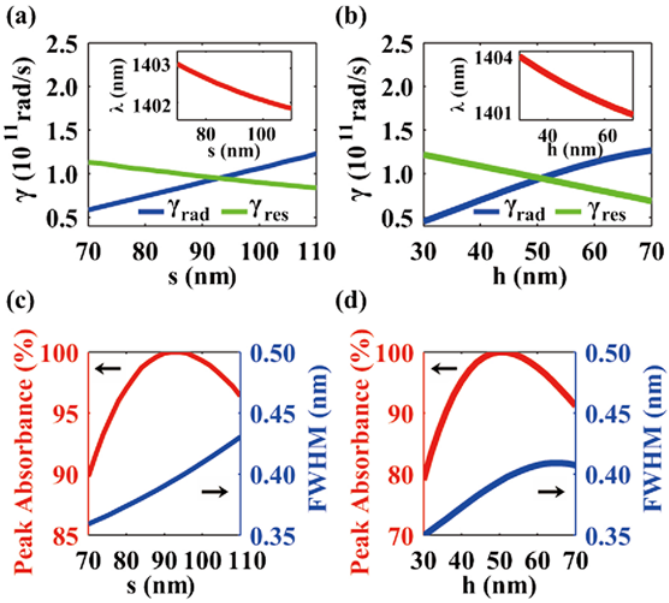

Figure 2.2: Radiative (γ_{rad}) and resistive (γ_{res}) damping rates of the eigenmodes as functions of (a) half of the grating ridges s, and (b) the depth of the grooves h. Insets: the resonant wavelength at each eigenmode. Peak absorbance and FWHMs of the corresponding eigenmodes are presented in (c) and (d). If not particularly specified, a=1400 nm, s=92 nm, and h=50 nm.

Peak absorbance is $4\gamma_{\text{rad}}\gamma_{\text{res}}/\gamma_{\text{tot}}^2$ at $\omega = \omega_0$. Critical coupling occurs when $\gamma_{\text{res}} = \gamma_{\text{rad}}$, leading to unity absorption ($A = 1$).

With grating period a=1400 nm fixed, as illustrated in Figs. 2.2(a, b), the other geometrical parameters are varied around s=90 nm and h=50 nm, respectively, to demonstrate how the radiative and resistive damping rates evolve under normal incidence. Insets show the resonant wavelengths $\lambda = 2\pi c/\omega_0$ of each eigenmode. The corresponding peak absorbance and FWHMs are presented in Figs. 2.2(c) and (d). The critical coupling condition at s=92 nm and h=50 nm can be obtained when energy coupled to the eigenmode is totally dissipated in metal through resistive loss without reflection. It is attributed to the complete destructive interference between light coupled from SPPs and light directly reflected from a metal surface. The resonant wavelength is 1402 nm and the FWHM is only 0.4 nm. It can be observed from Fig. 2.2 that the ultra-narrow band and high absorption are insensitive to variation of geometrical profile. In the studied regimes, the peak absorbance remains

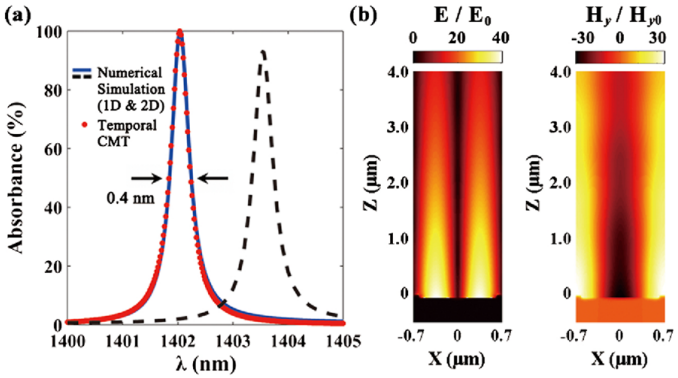

Figure 2.3: (a) Computed absorption spectra of the optimized grating and the crossed-grating using the numerical simulation and the temporal coupled-mode theory. Blue-solid and blackdashed lines correspond to the 1D grating and the 2D crossed-grating, respectively. (b) Electric and magnetic enhancements at resonant wavelength (1402 nm). E_0 and Hy_0 are excitation fields, E and Hy are total fields.

higher than 80 %, while the FWHMs stay under a half nanometer. The resonant wavelength is also stable, not exceeding 2 nm relative to 1402 nm. All these features are of importance to practical fabrication and applications. The temporal coupled-mode theory used here provides a time-saving method to optimize absorbers.

We proceed to use numerical simulations to validate the perfect absorption. The solid-blue and dotted-red lines in Fig. 2.3(a) demonstrate that absorption spectra calculated based on two methods agree well with each other. To excite SPPs, the momentum provided by the grating ($\beta = k_0 \sin\theta + n2\pi/a$) should match the propagation constant of SPPs (k_{spp}), where θ is the angle of incidence, n is an integer, and a is the structure's period. Since shallow grooves are small perturbations to the flat interface, k_{spp} of the grating should be approximately equal to that of a flat interface between metal and dielectric. We found that for the normal incidence, $\theta = 0°$, when $n = 1$, $\beta = 2\pi/a$ agrees with the k_{spp} of a flat metal-air interface, which $k_{\text{spp}} = 1.0034 \cdot (2\pi/a)$ at 1402 nm. Considering $a = 1400\,nm$ and $\lambda_0 = 1402$ nm, the wave vector component along normal direction $k_z = \sqrt{k_0^2 - k_{\text{spp}}^2}$ is almost zero. Therefore, the excited SPP field illustrated in Fig. 2.3(b) does not exhibit field confinement. The field is distributed above the grating with a very slow decay and only a small proportion of electromagnetic field penetrates into the metal, which implies a very small resistive rate. So the total damping rate under critical coupling

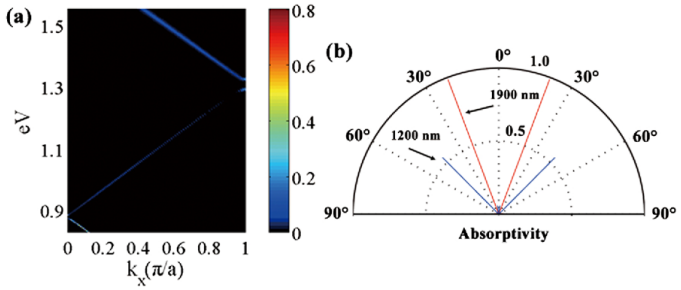

Figure 2.4: (a) Absorption at oblique incidence. $k_x = (2\pi/\lambda)\sin\theta$, λ is incident wavelength and θ is angle of incidence. k_x is normalized with respect to π/a. Photon energy $E = hc/\lambda$, h is the Planck constant, and c is the light speed in vacuum. (b) Absorptivity angular patterns at 1900 nm and 1200 nm of the perfect absorber.

condition (twice the resistive damping rate) is ultra-small, resulting in ultra-narrow band light dissipation of the perfect absorber.

The absorption spectrum of the crossed-grating at normal incidence is also calculated and presented in Fig. 2.3(a). The geometrical parameters are the same as those of the optimized grating. One can observe that it shows only a small redshift. High absorption (93 %) and ultra-narrow band (0.4 nm) still remain.

Absorption at oblique incidence is also studied and the spectra show abnormal characteristics. Figure 2.4(a) demonstrates absorptivity as functions of incident wavelength and angle of incidence. Coordinates are transformed to photon energy (unit: eV) and wavenumber along the x axis. The grating can be assumed to be a form of 1D photonic crystal. Figure 2.4(a) displays a profile of its band diagram, and two photonic bandgaps around 0.9 eV and 1.3 eV can be seen. To intuitively show the absorptivity as a function of the angle of incidence, absorption spectra at two given wavelengths are plotted in Fig. 2.4(b). At 1900 nm, it shows near unity absorbance only within an ultra-narrow angle (0.4 mrad). As we know, absorption and emission are two reciprocal processes. According to Kirchhoff's law, the absorptivity and the emissivity of a surface are equal for polarized directional light at the same wavelength [115]. So the perfect absorber can be regarded as a thermal emitter. The angular pattern of emissivity under the same condition is the same as that of absorptivity as shown in Fig. 2.4(b). One can observe that for certain wavelengths (1900 nm) the emissivity at a particular angle ($\approx 20°$) is extremely large compared with that at other angles. Besides, the enhanced emissivity is only located within

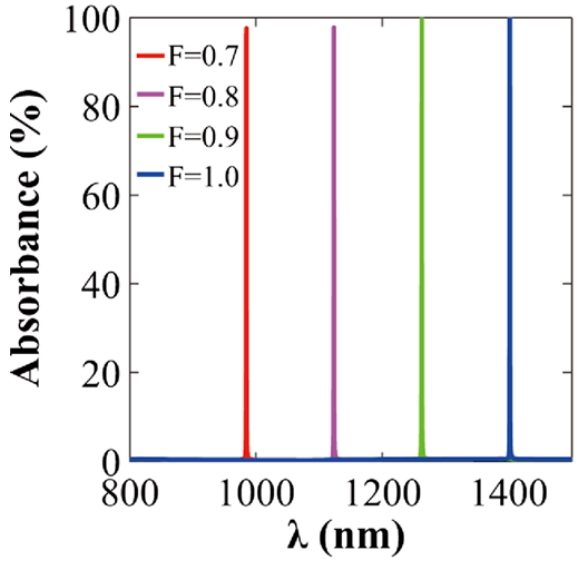

Figure 2.5: Absorption spectrum as a function of geometrical scaling factor F.

an ultra-small angular width (0.4 mrad), so it is a highly directional thermal emitter [112]. The narrow angular width is a signature of a large spatial coherence length ($l = \lambda/\theta = 2500\lambda = 4.75\,mm$) at the corresponding wavelength, which suggests high monochromatic in the near-field. The effect originates from thermally excited surface wave [55], which is in sharp contrast to the small spatial coherence length of the near-field of blackbody [116]. Figure 2.4(b) shows another interesting phenomenon; the emitter radiates light with different wavelengths at distinct angles, which has potential application in wavelength division.

Until now we focused on the structure operating resonantly at approximately 1400 nm at normal incidence. Further simulations exhibit that it is geometrically scalable. Every geometrical parameter (a, s, h, and r) is multiplied by scaling factor F, which starts from 0.7 with a step of 0.1. The results are presented in Fig. 2.5. The peak can be tuned at a range of hundreds of nanometers, while the maximum absorbance remains above 97 %, and FWHMs remain smaller than a half nanometer.

It is well known that for plasmonic nanometallic structures, resonant wavelength depends on the refractive index of the environmental dielectric. The effect can be utilized to construct different types of plasmonic sensors [117, 118], whose performances are usually described by sensitivity ($S = \Delta\lambda/\Delta n$) and FOM. But the

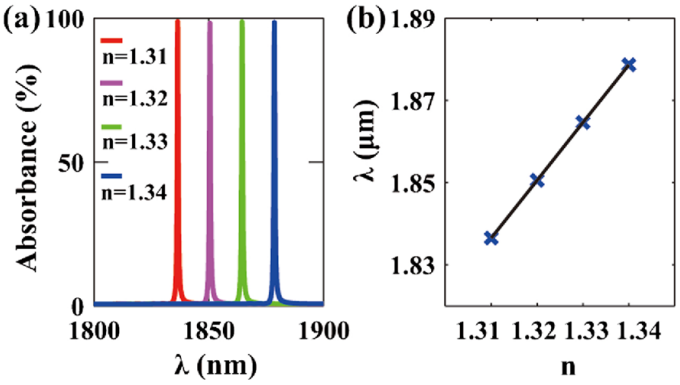

Figure 2.6: Dependence of (a) absorption spectra and (b) resonant wavelengths on the refractive index of the environmental dielectric.

reported FOM are typically less than 1000 /RIU in near infrared regime. Improving FOM by either increasing sensitivity or decreasing FWHM is still a challenge. In our simulations, the whole space over the absorber is filled by a dielectric with a refractive index n. Under normal illumination, dependence of absorption spectra on n is presented in Fig. 2.6(a). As n varies, the maximum absorptions remain near unity and FWHMs stay at 0.6 nm. The sensitivity is 1400 nm/RIU. Compared with a conventional absorber-based sensor, whose bandwidths are usually tens of nanometers, the bandwidth reported here is so small that the FOM can be as high as 2300 /RIU, paving the way for a highly sensitive plasmonic sensor. The peak wavelengths are extracted and plotted in Fig. 2.6(b), and good linearity is found. That is to say, the value of the variation of the peak wavelength divided by the variation of the refractive index is a constant.

It is worth noting that, in practice, it is inevitable that the incident light beam is composed of a range of incident angles, which will reshape the absorption spectra. Here the absorption spectrum with a Gaussian beam incidence is further investigated. In the simulations, the divergence of the Gaussian beam is chosen as 1°, and the waist of the beam is set at the very top of the structure. All other parameters are the same as those corresponding to the studied grating in Fig. 2.3(a). The result shows that although peak absorption drops from unity to about 55 %, the FWHM remains only 0.4 nm, which will not degrade its performance in sensor applications.

2.2 Absorbers relying on localized resonances

Relying on delocalized resonances to achieve ultranarrow band absorption makes it difficult to reduce the physical size of the structure in order to integrate multiple micropixels onto a single chip for hyperspectral related applications [119]. A similar tradeoff between the spatial extension of the structure and the spectral linewidth also applies to plasmonic sensing. While localized-resonance-based sensing down to a single nanofocus has been demonstrated [120, 121], the resulting spectra are broad owing to typically large ohmic and radiative losses. This limits the FOM, which is inversely proportional to the FWHM. When sensors with ultra-sensitivity are considered, they usually rely on lattice resonances [122, 123, 124]. Because their plasmonic-photonic hybrid-mode nature, they feature low dissipation rates, and therefore narrow bandwidths [27]. However, they demand considerable spatial extension of the sensor, as mentioned above for the absorber, which requires a relatively large amount of analyte and hinders parallel sensitive detection on tiny chips [125]. Consequently, high-performance light absorbers with a small footprint and an ultranarrow band are highly desirable.

From a different perspective, gain media show versatile functionalities in nanophotonics as discussed in section 1.5. Although it is well known that the bandwidth of a plasmonic system becomes smaller when it goes into an over-compensation regime, and even lasing action can occur with ultranarrow linewidth if the gain is large enough, much less attention has been paid to engineer the bandwidth before fully compensating the loss.

In this section, we propose to utilize high-order localized resonances combined with gain to realize high quality-factor perfect absorption within structures having small spatial extension. This strategy has two important benefits: (i) high-order optical modes exhibit much smaller coupling strength with external light compared with fundamental modes; and (ii) it is compatible with dielectric elements are doped with gain molecules or quantum dots to partially compensate the large ohmic loss associated with high-order modes, making resistive decay rate of the system similar in magnitude to the small radiative decay rate, thus realizing the condition of critical

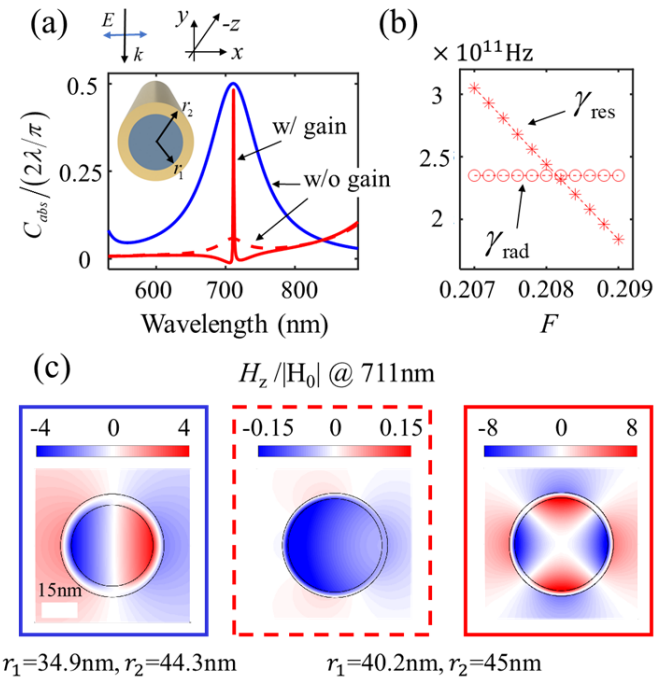

Figure 2.7: (a) Normalized absorption cross-sections of coreshell cylinders supporting a dipolar mode (blue curve), a quadrupolar mode without gain (red-dashed curve), or quadrupolar mode with gain (red-solid curve). The inset depicts the silica/gold coreshell structure. (b) Radiative and resistive decay rates of the quadrupolar mode at different gain level. (c) On-resonance normalized magnetic fields for the three different conditions considered in (a). The frames and the curves in (a) share the same color and line type codes. The radii of the two cylinders are indicated below the plots.

coupling needed for perfect absorption. In this way, the otherwise dark high-order modes are brought to be bright with maximum absorption according to coupled-mode theory. Specifically, we first demonstrate this idea in a simple nanocylinders geometry, which are followed by two other widely studied absorbers: MIM absorbers operating in the visible range; and a graphene Salisbury screen operating in the MIR region. The potential application in small footprint improved sensing is further discussed. Although we focus on 2D structures in all three cases for simplicity, we note that it is straightforward to extend our results to 3D geometries, which can be made polarization-independent.

The inset of Fig. 2.7(a) shows the cylinder under consideration, encompassing a

gold shell. Its relative permittivity is approximated using a Drude model based on experimental data in the investigated spectral range [28], $\varepsilon_{\mathrm{m}} = 1 - \omega_{\mathrm{p}}^2/(\omega^2 + \mathrm{i}\omega\gamma_{\mathrm{p}})$, where $\hbar\omega_{\mathrm{p}} = 6.98\,\mathrm{eV}$, $\gamma_{\mathrm{p}} = 0.11\,\mathrm{eV}$. The core is a dielectric, which can be further doped with various gain materials. Then the total electric response is $\varepsilon_{\mathrm{d}} = \varepsilon_{\mathrm{b}} + \varepsilon_{\mathrm{gain}}$ with a background term $\varepsilon_{\mathrm{b}} = 2.25$ (i.e., silica) and a Lorentzian gain term [91, 126] $\varepsilon_{\mathrm{gain}} = F\gamma_0/(\omega - \omega_0 + \mathrm{i}\gamma_0)$. Here, ω_0 and γ_0 are the gain frequency and bandwidth, respectively. We focus on Rhodamine 800 to provide the gain effect, whose emission wavelength $\lambda_0\,(= 2\pi c/\omega_0)$ is 711 nm, and $\gamma_0 = 0.04\omega_0$ [126]. Additionally, F is a factor that proportional to the population inversion of the gain material, therefore reflecting the gain level. Incidentally, we set $F = 0$ when we want to exclude gain.

Modes with different orders (*e.g.*, dipolar, quadrupolar mode, and other higher-order modes) can be excited by an external plane wave with its magnetic field polarized along the cylinder axis. Each mode is associated with a radiative decay rate (γ_{rad}) and a resistive decay rate (γ_{res}) that characterize the energy dissipation rate through coupling to the far-field and transformation into Joule heat in metal, respectively. The absorption can reach a maximum value when the two decay rates are equal [34], a condition generally known as critical coupling. Specifically, for the cylinder discussed here, we have the absorption cross-section of a single mode as [127]

$$C_{\mathrm{abs}} = 2\frac{2\lambda}{\pi}\frac{\gamma_{\mathrm{rad}}\gamma_{\mathrm{res}}}{(\omega - \omega_0)^2 + (\gamma_{\mathrm{rad}} + \gamma_{\mathrm{res}})^2}, \tag{2.2}$$

where the pre-factor of 2 accounts for two degenerate sub-modes because of rotational symmetry. One can find that the upper limit is $C_{\mathrm{abs,max}} = (2\lambda/\pi)/2$, which can be achieved when both critical coupling and on-resonance conditions are satisfied. Typically, the fundamental dipolar mode is preferred and no gain medium is involved. Because the mode has large coupling strength with the external light, it is therefore easily accessible. The blue curve in Fig. 2.7(a) and the left panel of Fig. 2.7(c) illustrate such a case, with $r_1 = 34.9\,\mathrm{nm}$, $r_2 = 44.3\,\mathrm{nm}$. Maximum absorption is achieved at 711 nm. But the bandwidth is large with FWHM=85 nm, resulting in a low Q factor (≈8). This limits its performance for sensing and photon detection. In order to improve the Q factor, utilizing destructive interference in complex structures to reduce radiative damping has been tried [128]. A straightforward

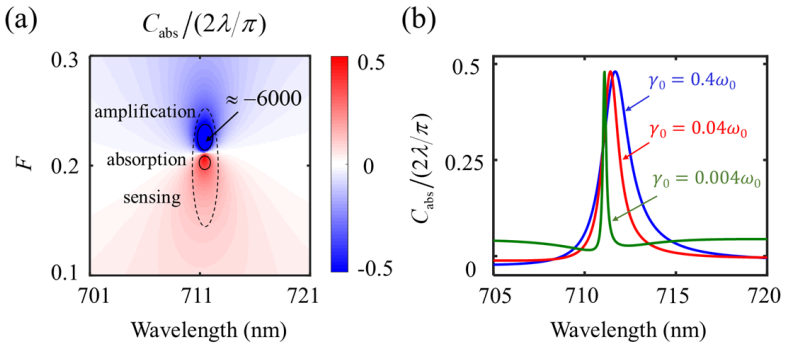

Figure 2.8: (a) Normalized absorption cross-sections at different wavelengths and gain levels. (b) Normalized absorption cross-section spectra when the gain bandwidth of the gain medium takes different values.

way to suppress radiative damping consists in rely on high-order modes. Using the eigenmode solver in COMSOL, we find that a coreshell cylinder with $r_1 = 40.2\,\text{nm}$, $r_2 = 45.0\,\text{nm}$ holds quadrupolar mode at 711 nm. However, this mode is difficult to excite from the far-field, as evidenced by the red dashed curve in Fig. 2.7(a) and the middle panel of Fig. 2.7(c). The associated absorption is very low, and the scattered field distribution is far from a well-defined quadrupolar mode. The reason lies in a big mismatch between the energy decay rates of the two channels. Doping the silica core with gain medium and finely tuning the gain level can address the problem. Figure 2.7(b) displays the dependences of γ_{rad} and γ_{res} for the quadrupolar mode on F. The detailed computation method of the decay rates is described in the last section. One can see that the resistive decay rate decreases with increasing gain. Critical coupling is realized when F takes the value about 0.208, leading to nearly perfect absorption ($C_{\text{abs}}/(2\lambda/\pi) = 0.48$) with a FWHM as small as 1 nm, as shown by the red solid curve in Fig. 2.7(a). The reason why the peak absorption is slightly below the upper limit (*i.e.*, 0.5) is that absorption is dominant, but it does not fully originate in the quadrupolar mode, as it is also influenced by the nearby dipolar mode. The right panel of Fig. 2.7(c) confirms an efficient excitation of the quadrupole mode assisted by gain. By comparing the field enhancements in the blue and the red solid borders, it is interesting to note that apart from the appealing feature of ultranarrow band, the high-order mode provides a stronger near-field.

Additionally, we simulate spectra with a wider range of F, as shown in Fig.

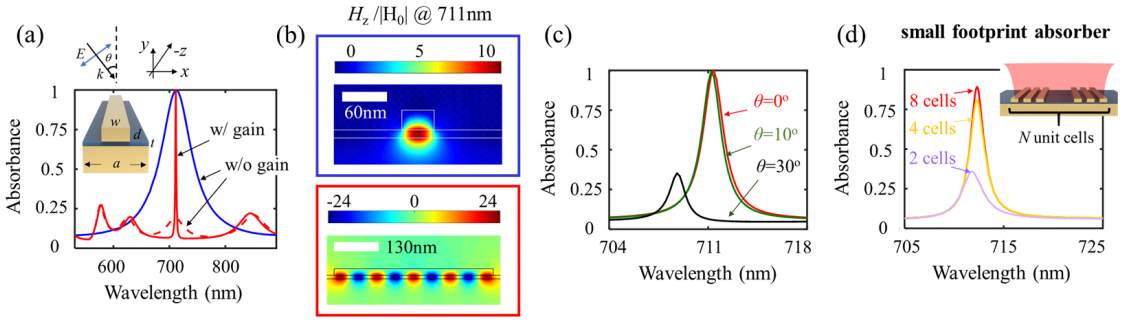

Figure 2.9: Absorption properties of infinite 1D arrays illuminated by plane waves (a-c) and finite arrays illuminated by Gaussian beams (d). (a) Absorption spectra of the absorbers supporting a fundamental mode (blue curve), a high-order mode without gain (red-dashed curve), or a high-order mode with gain (red-solid curve). The inset depicts the structure. (b) On-resonance normalized magnetic fields under the two different conditions considered in (a). The frames and the curves in (a) share the same color code. (c) Absorption spectra at different incidence angles. (d) Absorption spectra for finite arrays of different size (*i.e.*, number of unit cells). Both of (c) and (d) are for high-order mode structures.

2.8(a). All the involved parameters, except those indicated in the figure, keep the same. One can observe that at the resonant wavelength (*i.e.*, 711 nm), the normalized absorption cross-section first reaches an upper limit value of 0.5 with increasing gain, and subsequently, when going over a critical value of F, the absorption becomes negative, which means light amplification. The negative part is saturated by -0.5 for visual clarity. In some region, the amplification can be extremely large, as pointed out by an arrow. The structure with different gain levels can find different functions as indicated in the plot. Structures operating in under or over compensation regions can be both used for sensing. For the gain width, we adopt a practical value of Rhodamine 800 $\gamma_0 = 0.04\omega_0$, as used in the literature [126]. Figure 2.8(b) displays absorption spectra with artificially increased and decreased values. It is clear that the ultranarrow band feature can be influenced, but not dominated, by the gain width. The FWHM remains below 2 nm, even with a considerably large $\gamma_0 = 0.4\omega_0$ rate is used. This reveals that the ultranarrow band is a unique advantage, mainly resulting from the combination of a high-order mode and gain, rather than from the small gain bandwidth.

Now, we apply the same idea to solid-state planar absorbers. As discussed in

the last section, unity absorbance can be achieved on resonance under the critical-coupling condition. Firstly, we focus on the popular MIM absorbers. The inset of Fig. 2.9(a) shows the cross-section of a single period: a dielectric spacer ($\varepsilon_{\mathrm{b}} = 1.75^2$, *i.e.*, Al_2O_3) with thickness t is sandwiched between a continuous gold film and a gold strip. The width and the height of the strip are w and d, respectively. Also, a denotes the period. The upper and lower metal elements can interact strongly if the dielectric layer is thin enough. When carefully designed, the impinging plane wave with magnetic field along the strip can induce anti-parallel electrical currents in the two metal elements, therefore generating a remarkable magnetic resonance in the gap [129, 16]. Researchers normally use a fundamental mode as displayed by the field profile in the upper panel of Fig. 2.9(b). Its absorbance is indicated by the blue curve in Fig. 2.9(a), with complete absorption at 711 nm. The geometric parameters are: $w = 48\,\mathrm{nm}$, $d = 30\,\mathrm{nm}$, $t = 12\,\mathrm{nm}$ and $a = 250\,\mathrm{nm}$. We note that the large FWHM (≈70nm) leads to a fairly low Q factor (≈10). In order to achieve high-Q perfect absorption, we switch to a structure that holds a high-order resonance and is doped with the same dye molecules (*i.e.*, Rhodamine 800) as in its dielectric spacer. Its geometric parameters are: $w = 476\,\mathrm{nm}$, $d = 20\,\mathrm{nm}$, $t = 10\,\mathrm{nm}$ and $a = 520\,\mathrm{nm}$. Complete absorption with FWHM=2 nm is achieved at 711 nm when F is tuned to 0.171 (red solid curve in Fig. 2.9(a)), enhancing the Q factor by up to ≈356. The on-resonance field distribution is displayed in the lower panel of Fig. 2.9(b). If no gain medium is involved (*i.e.*, $F = 0$), the peak absorbance dramatically drops to about 0.2, as shown by the red dashed curve in Fig. 2.9(a). Figure 2.9(c) shows the angle-dependence absorption. The resonance blue-shifts and becomes much weaker when the incidence angle is increased to 30° because of the spatially extended optical resonance mode compared with the light wavelength.

We have so far investigated absorbers with an infinite period, in line with many previously published numerical studies. Now, using high-Q localized resonance we can also realize small footprint ultranarrow band absorbers. We simulate finite arrays to demonstrate this concept. The inset of Fig. 2.9(d) presents the configuration under study, in which a Gaussian beam is normally illuminating an absorber with its beam waist placed at the dielectric layer. The waist radius is equal to the resonant wavelength, 711 nm. All geometric and material parameters are the same as in the previous infinite arrays. We can observe from the yellow curve that a small-area ab-

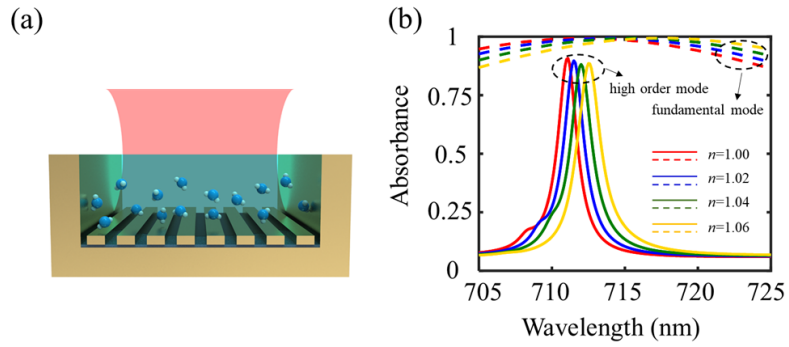

Figure 2.10: (a) A schematic view of a nanodevice for gas sensing. The grooves are filled with the targeted gas, featuring a refractive index n. (b) Absorption spectra when the gas takes different indices. The solid (dashed) curves correspond to the structure utilizing a high-order (fundamental) mode.

sorber, which is around 1.5 times the beam waist, can dissipate 80% of the incoming light energy with a bandwidth less than 3 nm.

These properties are useful for sensing small volume analyte with higher FOM compared with using the fundamental resonance. Figure 2.10(a) presents a sketch of the designed sensor. The absorber, which consists of 8 unit cells, is integrated onto the bottom of a gold groove. The depth of the groove is 1 μm. The detected gas with refractive index n is assumed to fill the groove spaces. The Gaussian beam is coming from the air side. All involved parameters are maintained the same as above. The solid curves in Fig. 2.10(b) illustrate the dependence of the absorption spectra on the gas refractive index (see figure legend). For comparison, we show calculations for an absorber based on the fundamental mode (dashed curves) as described in Fig. 2.9(a, b) without changing other parameters (*i.e.*, the depth and width of the groove). We find that while the sensitivity of the high-order mode structure, which is 25 nm/RIU, is smaller than the one based on the fundamental mode, which is 83 nm/RIU, its FOM is one order of magnitude larger. The FOMs of the high-order-mode and the fundamental-mode structures are 8.3 /RIU and 0.8 /RIU, respectively.

Apart from the visible range, absorbers working in MIR region are of great interest as well, especially for applications in sensing of molecular vibrational bonds and thermal imaging [130]. In this context, graphene plasmons have raised huge expectations owing to their outstanding optical properties in this spectral range

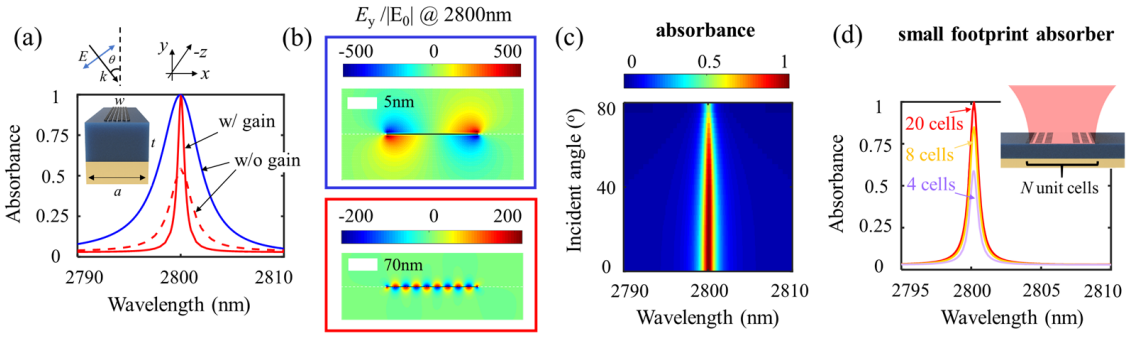

Figure 2.11: Absorption properties of infinite 1D arrays illuminated by plane waves (a-c) and finite arrays illuminated by Gaussian beams (d). (a) Absorption spectra of absorbers supporting a fundamental mode (blue curve), a high-order mode without gain (red-dashed curve), or a high-order mode with gain (red-solid curve). The inset depicts the structure under consideration. (b) On-resonance normalized magnetic fields under the two different conditions examined in (a). The frames and the curves in (a) share the same color code. (c) Absorbance as a function of incidence angle and wavelength. (d) Absorption spectra for finite arrays of different size (*i.e.*, number of unit cells). Both of (c) and (d) are for high-order mode structures.

[37, 38]. Perfect absorption has been demonstrated both theoretically [39] and experimentally [40]. Here, we shift our focus from the conventionally used dipolar resonance to higher-order resonances, showing that narrower linewidths are possible. A unit cell of the structure, which incorporates a Salisbury screen, is presented in the inset of Fig. 2.11(a). A thick dielectric layer with thickness t ($\varepsilon_b = 2$, *i.e.*, GaF_2) separates a graphene nanoribbon and a gold film. The surface conductivity of the graphene layer is described by a Drude model $\sigma = (e^2/\pi\hbar^2)\mathrm{i}E_\mathrm{F}(\omega + \mathrm{i}\tau^{-1})$, where $\tau = \mu E_\mathrm{F}/e\nu_\mathrm{F}^2$ is the intrinsic inelastic lifetime. In the simulation, we assume $E_\mathrm{F} = 0.8\,\mathrm{eV}$, $\mu = 2.5 \times 10^4\,\mathrm{cm^2 \cdot V^{-1} \cdot s^{-1}}$ and $\nu_\mathrm{F} = 10^6\,\mathrm{m \cdot s^{-1}}$. Besides, we set the filling fraction of the graphene ribbon area to be 0.5 (*i.e.*, $w = a/2$). when w, a and t take values of 16 nm, 32 nm and 885 nm, respectively. a normally incoming plane wave with its magnetic field along the ribbon excites the dipolar resonance as shown in the upper panel of Fig. 2.11(b). The blue curve in Fig. 2.11(a) shows the absorbance. Perfect absorption is achieved at 2800 nm with a FWHM of 5 nm. Then, we reconfigure the absorber with $w = 214\,\mathrm{nm}$, $a = 428\,\mathrm{nm}$ and $t = 481\,\mathrm{nm}$, so that it holds a high-order resonance at the same wavelength. Additionally, we introduce a dielectric layer doped with Er^{3+} ions, whose emission wavelength is $\lambda_0 = 2800\,\mathrm{nm}$

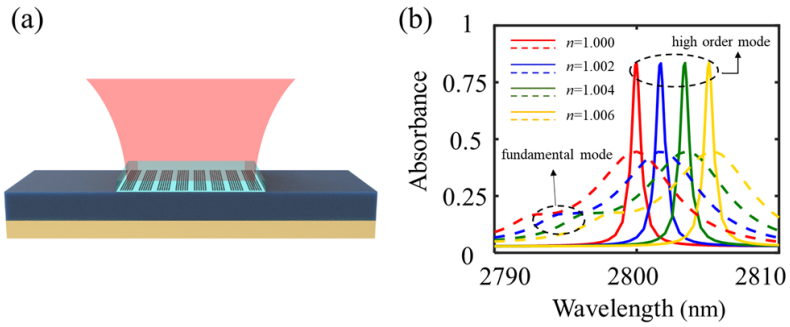

Figure 2.12: (a) Schematic view of a nanodevice for thin molecular layer sensing. The molecular layer with thickness of 10 nm is characterized by a refractive index n. (b) Absorption spectra for different molecular layer indices. The solid (dashed) curves correspond to the structure utilizing the high-order (fundamental) resonance.

and whose gain bandwidth is $\gamma_0 = 0.03\omega_0$ [126]. When the gain level is tuned to $F = 0.0018$, perfect absorption is recovered with a narrower linewidth of FWHM equal to 0.8 nm. The lower panel of Fig. 2.11(b) represents its on-resonance field distribution. If there is no gain involved, the peak absorbance drops to around 0.5 (red dashed curve). Figure 2.11(c) presents the dependence of the absorbance on wavelength and incidence angle. One can observe that the ultranarrow band feature is robust over a large angular range. The absorbance remains at a level close to 0.5 when the angle is increased to 80°. In the same way as for the configuration in Fig. 2.9(d) discussed in the last section, Figure 2.11(d) recovers explicitly the absorption performance of a finite array. All the parameters are maintained the same as in the infinitely extended structure. Here, the waist radius of the Gaussian beam is equal to the resonant wavelength, 2800 nm. Thanks to the large optical cross-section and wide-angle features of the graphene ribbon, 20 unit cells, which span about 1.53 times the beam waist, are enough to fully dissipate the incoming light.

The ultra-confinement of the near-field provided by the graphene plasmons renders this material particularly promising for molecular sensing [36, 131]. We show that the structure supporting a high-order resonance improves the FOM compared with its counterpart relying on a fundamental resonance. A schematic view of the sensing device is illustrated in Fig. 2.12(a). For the high-order resonance sensor, the structure consists of 8 unit cells. The cells are covered by a 10 nm-thick molecular layer, which is simply described by a refractive index that increases with increas-

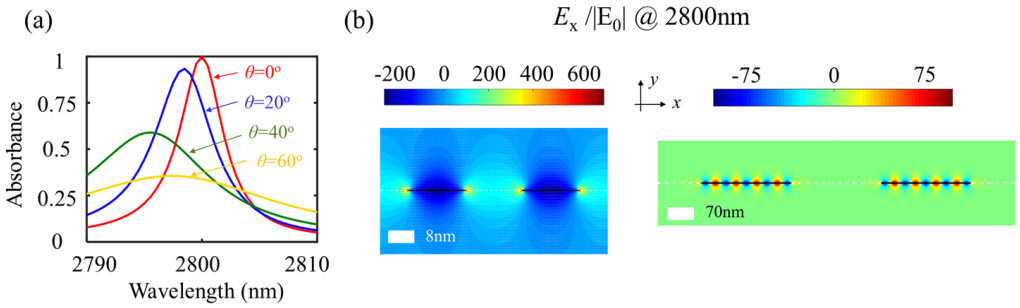

Figure 2.13: (a) Absorption spectra of a graphene Salisbury screen consisting of infinite arrays at various incidence angles. (b) Normalized electric fields of infinite arrays, supporting a fundamental dipolar resonance (left panel) and a high-order resonance (right panel) under normal incidence.

ing molecular density [132]. For comparison, we replace the high-order resonance absorber with the fundamental resonance one, maintaining the width of the ribbon array, as well as that of the molecular layer, approximately the same. Figure 2.12(b) displays their absorption spectra with various layer indices in the 1 to 1.006 range. Although their sensitivities are almost the same, the high-order-resonance-based sensor holds a large FOM (944 /RIU) compared with its fundamental-mode counterpart, whose FOM is 131 /RIU.

Comparing the blue curve in Fig. 2.11(a) and the dashed lines in Fig. 2.12(b), we find that the peak absorbance drops from unity for an infinite array to less than 0.5 for a finite array. We attribute this effect to the partial lattice resonance nature in the absorber, supporting a dipolar resonance at 2.8 μm. Figure 2.13(a) shows the dependence of the absorption spectra on the incidence angle for the infinite array, which illustrates a large group velocity of the optical mode propagating along the x direction, and therefore a large propagation length [119]. As a result, a very large finite array should be required to approach the performance of an infinite array. The left panel of Fig. 2.13(b) confirms the lattice resonance in the array based on strong optical coupling between two adjacent ribbons. This is in sharp contrast to the high-order resonance scenario discussed in Fig. 2.13(b). The well localized mode leads to omnidirectional absorption of an infinite array (Fig. 2.11(c)) and unity absorbance for a finite array (Fig. 2.11(d)). Incidentally, we also note that the strong coupling between individual ribbons originally results from the short light wavelength that

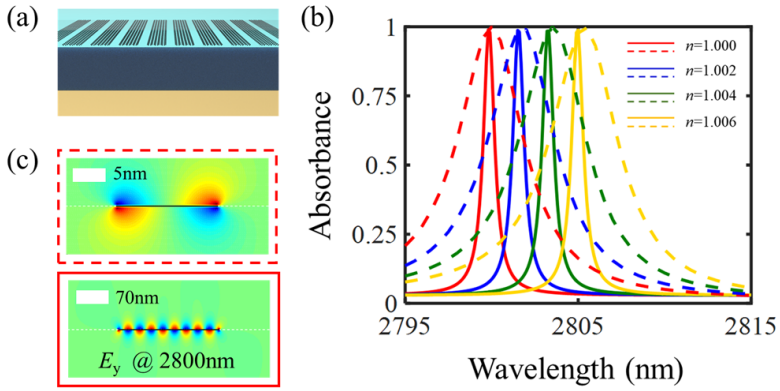

Figure 2.14: (a) Schematic view of an infinitely large graphene Salisbury screen covered by a 10 nm-thick molecular layer. (b) Absorption spectra with different diffraction indices of the molecular layer. Solid (dashed) curves correspond to the structure that holds high-order (fundamental) resonance. The relevant geometrical parameters of the two structures are the same as in Fig. 2.11(a). (c) On-resonance field patterns of the high-order and fundamental resonances with $n = 1$. They are copies of Fig. 2.11(b). The frames and the curves in (b) share the same color and line type codes.

we are considering. The interaction can be made weaker if operating at longer wavelengths.

We carry out additional simulations using extended graphene Salisbury screens for sensing. We conclude that the structure holding a high-order resonance operates much better than a structure operating based on its fundamental mode. Fig. 2.14(a) depicts the extended screens, which is covered by a 10 nm-thick molecular layer (bright blue part). The solid (dashed) curves in Fig. 2.14(b) correspond to structures with a high-order (fundamental) resonance with various layer indices in the 1 to 1.006 range. All the needed geometrical parameters of the two structures keep the same as in Fig. 2.11(a). The upper (lower) panel of Fig. 2.14(c) illustrates the on-resonance field distribution of the fundamental (high-order) mode when the layer index is assumed to be 1. We find the FOM associated with the high-order-resonance structure to be 1083 /RIU, which is larger than that of the conventional structure operating based on its fundamental mode (183 /RIU).

2.3 Conclusions

In summary, in this chapter, we first design and investigate a lamellar grating with shallow grooves, which shows perfect absorption and ultra-narrow band (0.4 nm) dissipation under normal incidence. High absorption (93 %) and ultra-narrow band maintain when extending the optimized 1D grating to 2D crossed grating. According to Kirchhoff's law, the perfect absorber can be considered as a highly directional thermal emitter with an angular width of 0.4 mrad at 1900 nm. The absorption spectra of the perfect absorber are highly sensitive to the refractive index of the environmental dielectric. The sensitivity and FOM are as high as 1400 nm/RIU and 2300 /RIU, respectively. The structure presented here has great potential as a perfect absorber or high performance plasmonic sensor. Reported ultranarrow band absorbers usually rely on delocalized resonances like in this case. Minimize the size of the structure at the meantime maintain the high Q property is a desired goal. We propose a general route in the second part of this chapter to address this issue. It is realized through using high-order optical resonances combined with a proper gain, pumped by either light or electrical means. We demonstrate this strategy through numerically simulations for three different structures based on different absorption mechanisms. The sizes of the absorbers can be made small, comparable with the Gaussian beam waists. The absorption peaks are nearly perfect and the bandwidths are much smaller than their counterparts. We further exploit these results to achieve improved performance in refractive-index sensing. The present work will stimulate further investigations for applying the method to customize absorption in other plasmonic systems. Finally, we expect this idea can also benefit ultra-high-quality-factor absorber/emitter designs in dielectric nanophotonics [133], where a gain medium is perhaps not needed because of the low intrinsic loss, although it could also be employed to compensate radiative losses. Nevertheless, plasmonic systems have unique advantages for some applications such as hot-electron generation with small-footprint structures, as well as switchable photodetectors.

Chapter 3

Light scattering on coreshell/multilayer nanospheres

In the preceding section 2.2, we have discussed how to add gain media into the 2D coreshell nanocylinders to realize ultranarrow band absorption. In this chapter, we study 3D metallodielectric coreshell and multilayer nanospheres. In the first section, we explore how to use the coreshell nanoparticles to enhance emission intensities of upconversion nanoparticles (UCNPs) located in the center. Simulations based on Mie theory combined with a predictive theory based on rate equations point out optimal structures under different pump conditions. In the remaining sections, we investigate some unique properties of field enhancement, photothermal effect, and internal pressure lift of multilayer nanoparticles. These kinds of nanoparticles are capable of hosting collective plasmon oscillations distributed among different metallic layers, which result in large near-field enhancement at specific regions of the structure, where light absorption is maximized. In section 3.2, we exploit this capability of multishell nanoparticles, combined with thermal boundary resistances and spatial tailoring of the optical near-fields, to design plasmonic nano-ovens capable of achieving high temperatures at the core region using moderate illumination intensities, as well as large optical intensity enhancement $\sim 10^4$ over a relatively broad core region. This provides an unusual thermal environment, which together with the

high thermal induced pressures $\sim 10^5$ atm (see section 3.3), holds great potential for exploring physical and chemical processes under extreme optical/thermal/pressure conditions in confined nanoscale spaces.

3.1 Coreshell nanospheres for upconversion processes

UCNP is a kind of nonlinear nanocrystal, which has capability for sequentially absorbing two or more low energy photons and radiating high energy ones. They are typically composed of lanthanide ions (*e.g.*, Er^{3+} and Yb^{3+}) embedded within an inorganic crystalline host matrix (*e.g.*, $NaYF_4$) [134]. Compared with conventional luminescent nanomaterials (*e.g.*, dye molecules and quantum dots), UCNPs have remarkable advantages including superior photostability, long lifetimes, tunable emission bands, and low cytotoxicity. Therefore, they have strong potential for bioapplications, and have emerged as a hot topic in recent years [135, 136]. However, the low emission intensity is a barrier on the road to large scale practical use. A promising way to address this problem is to place the UCNPs in the vicinity of plasmonic nanostructures, using either the enhanced fields at pump wavelengths to increase the excitation rates of lanthanide ions or the increased local density of optical states (LDOS) at the emission wavelengths to speed up their radiative decay rates. Various structures based on them have been proposed [137, 138, 139, 140]. In this section, we are interested in UCNP@silica@gold nanospheres as shown in Fig. 3.1(a). In the following, we firstly present a theory, which identifies dominant factors of the gold shell to influence the emission intensities under different pump strengths. Then, an accurate and fast analytical method is used to carry out extensive simulations of the emission intensity enhancements over a wide range of geometrical parameters. Combining theory and simulations, we predict optimal structures under different pump conditions.

We start from a rate equation of the UCNP,

$$\frac{dp}{dt} = I_0 \cdot \mathrm{FE} \cdot \sigma \left(1 - p\right) - \mathrm{LDOS} \cdot g_0 \cdot p, \tag{3.1}$$

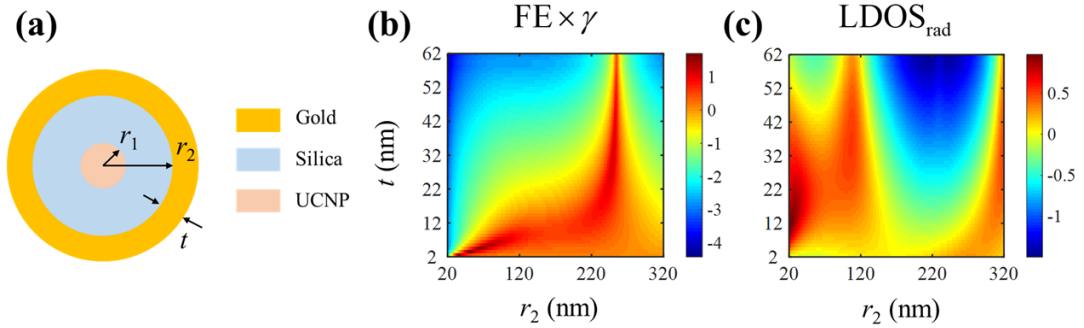

Figure 3.1: (a) Schematic view of a UCNP@silica@gold nanosphere. (b) Product of field enhancement at pump wavelength and yield at emission wavelength as a function of gold shell thickness and silica radius. (c) Radiative part of the LDOS at the emission wavelength as a function of gold shell thickness and silica radius.

where p describes the fraction of the UCNP ions that are excited by the pump light at a given time and I_0 is the pump intensity. FE denotes the average field intensity enhancement over the UCNP volume and σ is a coefficient proportional to the cross-section for excitation of the UCNP complex without coating. In this section, the LDOS (as well as $\mathrm{LDOS_{rad}}$ below) specifically refers to a volume-averaged values in the UCNP normalized to that in air (see details in Appendix B). Also, g_0 is the intrinsic decay rate without coating. Under cw conditions (*i.e.*, $dp/dt = 0$), one has $p = 1/(1 + \mathrm{LDOS} \cdot g_0/(I_0 \cdot \mathrm{FE} \cdot \sigma))$. We use $\mathrm{LDOS_{rad}}$ to refer to the radiative contribution of the LDOS. Because the emission intensity enhancement is $I_{\mathrm{em}} = \mathrm{LDOS_{rad}} \cdot p$, We finially have

$$I_{\mathrm{em}} = \frac{\gamma}{1/\mathrm{LDOS} + g_0/\left(I_0 \cdot \mathrm{FE} \cdot \sigma\right)}, \tag{3.2}$$

where $\gamma = \mathrm{LDOS_{rad}}/\mathrm{LDOS}$. When the pump intensity is in the saturation regime, $I_{\mathrm{em}} = \mathrm{LDOS_{rad}}$. In contrast, when the pump light is very weak, $I_{\mathrm{em}} = C \cdot \mathrm{FE} \cdot \gamma$, where $C = I_0\sigma/g_0$.

Here, we focus on these two limiting regimes. The nanoparticles are assumed to be in air. The diameter of the UCNPs takes a constant value of 32 nm. The refractive indices of both the host lattice of the UCNP and the silica shell are set to 1.475. The dielectric permittivity of gold is taken from experimental data [28]. The average field enhancements are computed at 980 nm. The average LDOS, $\mathrm{LDOS_{rad}}$,

and γ are computed at 540 nm (see Appendix B for detailed methods). Figure 3.1(b) and (c), respectively, display FE $\cdot\, \gamma$ and $\mathrm{LDOS_{rad}}$. The data are presented in log scale. In Fig. 3.1(b), one can observe that there are two hot regions. The lower left one is induced by dipolar resonances supported by the gold shells and the other one corresponds to cavity resonances. So, we can conclude that if one can experimentally synthesize small coreshell nanoparticles with good control on the shell thickness, it is preferable to utilize the dipolar resonances, as they provide higher enhancement. But, if one can only produce relatively large coreshell particles, it it better to adopt the cavity resonances. Figure 3.1(c) shows a similar pattern. Properly designed small coreshell nanoparticles ($r_2 \approx$20 nm, $t \approx$15 nm) hold dipolar resonances, while the larger ones can hold cavity resonances. A difference is that because 540 nm (Fig. 3.1(c)) is much shorter than 980 nm (Fig. 3.1(c)), apart from the fundamental mode, there is a high-order mode appearing in the investigated parameter ranges.

3.2 Field enhancement and temperature distribution in multilayer nanospheres

In this work, we combine optical Mie theory and a two-temperature model, including the influence of the temperature-dependent thermal boundary conductance (TBC, also known as Kapitza conductances [141, 142, 143, 144]), to efficiently design a plasmonic nano-oven, in which we optimize both optical and thermal responses. Especifically, we show that nanoscale thermal management can be achieved by simultaneously engineering multiple thermal boundary barriers and plasmonic near-field enhancement. Our nano-oven designs simultaneously feature three appealing properties: (i) it efficiently concentrates the electric field into the core region as a result of electrostatic cascading [145], reaching a relative intensity enhancement $> 10^4$; (ii) the optical field enhancement at the core region, accompanied by multiple thermal barriers originating in the TBC at the interfaces between metal and dielectric [146], render high core temperatures with relatively moderate illumination intensities.

Figure 3.2(a) presents a sketch of a metallodielectric multishell nanoparticle that

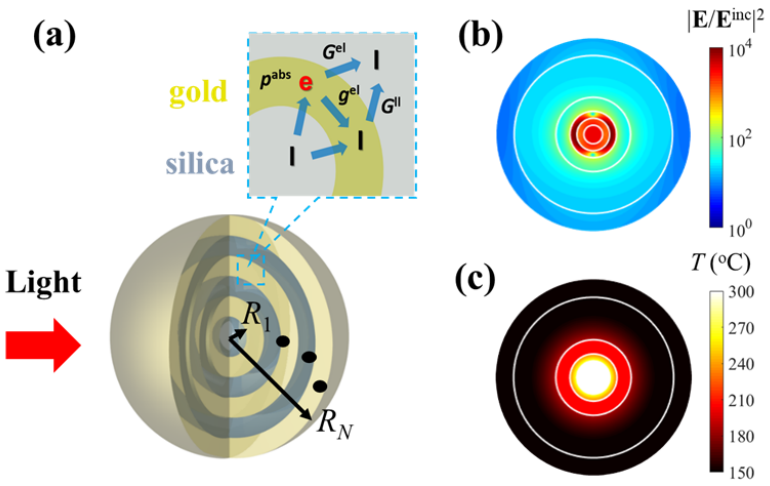

Figure 3.2: (a) Schematic view of a multishell nanoparticle made of alternating metallic and dielectric layers. The inset shows different heat transfer channels: coupling between electrons (e) and lattice modes (l) inside a metal layer (mediated by the volumetric transfer coefficient g^{el}) and coupling between these degrees of freedom and lattice modes in the surrounding dielectrics through thermal boundary conductances (TBCs) G^{el} and G^{ll} (see Appendix C). (b-c) We illustrate the large optical field enhancement (b), and efficient temperature increase (c) in a plasmonic nano-oven composed of $N = 3$ gold layers intercalated with silica and immersed in water under ambient conditions. The incident light has an intensity of $1\,\mathrm{GW/m^2}$ and a wavelength of 690 nm.

acts as a nano-oven. It is formed by alternating gold and silica shells, embedded in a water environment. We aim at simultaneously exciting plasmon dipolar modes of several of the gold shells in a constructive manner, so that inner layers are exposed to stronger optical fields and the core sees a large light intensity. This type of geometry has been previously explored for near-field concentration in multishells [147]. This is a cascading effect similar to the one previously studied for self-similar particle chains [145]. The increase in field intensity is also accompanied by higher absorption due to Joule losses, therefore resulting in an increase of temperature at the core of the structure, which is the main task of the nano-oven. This heat is eventually dissipated through the thermal conduction of the layers, until it is eventually released to the surrounding water. We remark that there is a beneficial effect arising from the presence of multiple metal/dielectric interfaces: each of them presents some resistance to the passage of heat, thus resulting in an efficient barrier that prevents heat at the core from rapidly escaping from the structure.

In order to simulate the optical and thermal responses of the nano-oven, we construct semi-analytical models, as discussed in detail in the Appendix C. The optical response is expressed as a generalization of Mie theory [148, 149] adapted to multishell spheres. This approach is fast and accurate compared with alternative numerical methods, thus allowing us to explore a large number of geometrical configurations.

The thermal response is formulated as a set of analytical nonlinear equations (see Appendix C) that describe heat exchange processes in a layer by layer fashion. We consider a monochromatic cw external illumination, so that the structure operates under steady-state conditions. We adopt the two-temperature model and define electron and lattice temperatures at each of the metallic layers. For simplicity, and because the thermal conductivity is large in gold compared with the surrounding silica and water media, we assume these two temperatures to be uniform within each layer. The temperatures are the unknowns of our set of nonlinear equations, together with the dielectric and water temperatures right at their interfaces with the metal.

Heat flow within the nano-oven is mediated by several key processes that are sketched in the inset of Figure 3.2(a). First of all, light is absorbed at the metallic

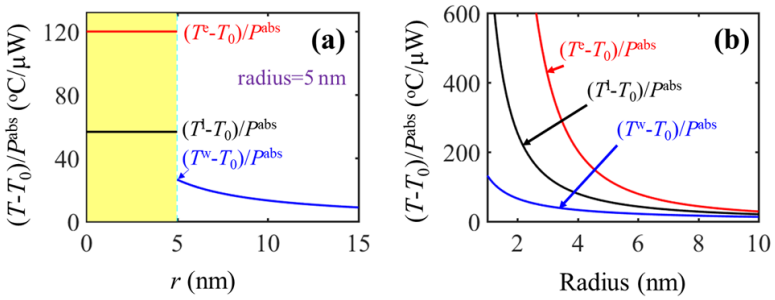

Figure 3.3: Thermal response of small metal nanoparticles. (a) Radial distribution of the temperature for a gold nanosphere in water (5 nm radius) normalized to the optically absorbed power. The environment temperature $T_0 = 300$ K. (b) Under the same conditions as in (a), dependence of various temperatures on particle radius: electron and lattice gold temperatures T^e and T^l, and water temperature right outside the particle T^w.

layers, resulting in a position-dependent heat power density given by

$$p^{abs}(\mathbf{r}) = \frac{\omega}{2\pi}\mathrm{Im}\left\{\epsilon(\mathbf{r},\omega)\right\}\left|\mathbf{E}(\mathbf{r})\right|^2, \tag{3.3}$$

where $\epsilon(\mathbf{r},\omega)$ is the position- and light-frequency-dependent permittivity, while $\mathbf{E}(\mathbf{r})$ is the amplitude of the optical electric field (*i.e.*, $\mathbf{E}(\mathbf{r})e^{-i\omega t} + \mathbf{E}^*(\mathbf{r})e^{i\omega t}$ gives the full time-dependence of the electric field); Eq (3.3) reveals that only the gold can directly couple optical energy into heat through its nonvanishing $\mathrm{Im}\{\epsilon\}$, dominated by electronic excitations. Coupling between electronic and lattice (phonons) degrees of freedom at each gold layer is described through a coefficient g^{el} [150]. Finally, the noted thermal barriers at each metal/dielectric interface are described through the TBCs G^{el} and G^{ll} associated with two different channels, involving the coupling of electronic (G^{el}) and lattice (G^{ll}) heat in the metal to lattice heat in the dielectric. All of these parameters are incorporated in our model, as discussed in detail in Appendix C.

Before discussing the multishell nano-oven, it is instructive to examine the steady-state thermal performance of a homogeneous gold sphere in water (Figure 3.3). We use a similar analysis as in Methods, which extends the results of previous work [71] in order to incorporate thermal barriers [151, 72, 152]. Three combined effects contribute to create a high temperature in both the lattice (T^l) and electrons

(T^{e}) subsystems of the gold: (i) the small surface area limits the rate of heat evacuation, thus resulting in a jump of temperature T^{w} in the water right outside the particle relative to ambient temperature T^0 given by [71]

$$T^{\mathrm{w}} - T_0 = \frac{P^{\mathrm{abs}}}{4\pi R \kappa_{\mathrm{water}}},$$

which scales linearly with the total absorbed power P^{abs} and is inversely proportional to the particle radius R and the thermal water conductivity $\kappa_{\mathrm{water}} = 0.6\,\mathrm{W\,m^{-1}\,K^{-1}}$; (ii) additionally, the thermal barrier at the interface produces a jump in the gold lattice temperature T^{l}, expressed in terms of the gold/water TBC [153] $G_{\mathrm{gold/water}} = 105\,\mathrm{MW\,m^{-2}\,K^{-1}}$ as

$$T^{\mathrm{l}} - T^{\mathrm{w}} = \frac{P^{\mathrm{abs}}}{4\pi R^2 G_{\mathrm{gold/water}}};$$

(iii) finally, the electron-lattice coupling, described through the coefficient [150] $g^{\mathrm{el}}_{\mathrm{gold}} = 3 \times 10^{16}\,\mathrm{W\,m^{-3}\,K^{-1}}$, produces an additional jump

$$T^{\mathrm{e}} - T^{\mathrm{l}} = \frac{3P^{\mathrm{abs}}}{4\pi R^3 g^{\mathrm{el}}_{\mathrm{gold}}}.$$

Notice that under steady-state conditions the absorbed power is conserved in this expressions during its flow from the light to the electrons, then to the lattice, and finally to the water. The temperature jump can be significant even for a gold nanoparticle of 5 nm radius (Figure 3.3(a)), while it is boosted as the radius becomes smaller (Figure 3.3(b)). This is an effect that deserves further investigation from the experimental viewpoint.

The temperature jumps in Figure 3.3 are normalized to the absorbed power, which for a sufficiently small sphere is given by the electrostatic expression

$$P^{\mathrm{abs}} = 24\pi^2 (R^3/\lambda) \epsilon^{3/2}_{\mathrm{water}}\, I_0\, \mathrm{Im}\left\{-1/(\epsilon_{\mathrm{gold}} + 2\epsilon_{\mathrm{water}})\right\}$$

in terms of the light intensity I_0 and the permittivities of gold and water (*e.g.*, $P^{\mathrm{abs}} \approx 1\,\mu\mathrm{W}$ for $R = 5\,\mathrm{nm}$, $I_0 = 4\,\mathrm{GW/m^2}$, and a resonant light wavelength $\lambda = 522\,\mathrm{nm}$). The same three mechanisms are at work in the nano-oven, operating in a contructive concatenation through the multiple shells, and supplemented

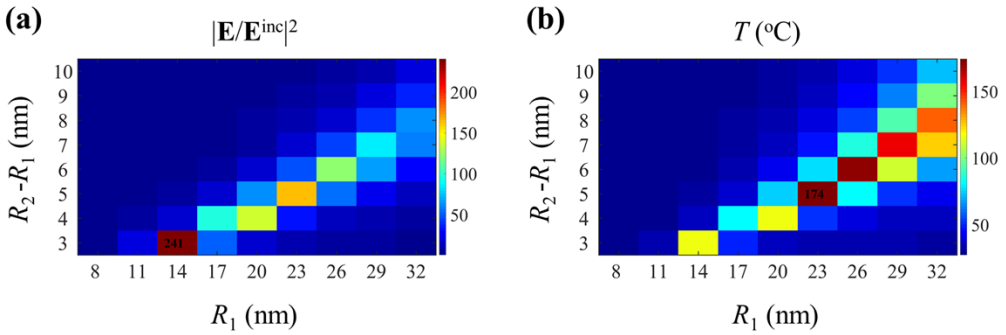

Figure 3.4: Optimization of optical and thermal parameters in a gold/silica coreshell structure. (a) Average electric field intensity enhancement and (b) temperature increase at the core of a nanoparticle as a function of the silica core radius R_1 and the gold shell thickness $R_2 - R_1$. The intensity of the external pump is $1\,\mathrm{GW/m^2}$.

by the noted optical cascading effect, which contributes to accumulate more light absorption near the nano-oven core, as we show next.

We now return to the nano-oven structure and use the thicknesses of the different gold and silica layers as geometrical parameters that allow us to optimize its performance. Focusing on a nano-oven consisting of three gold layers intercalated with silica, after a thorough examination of these parameters, with the additional constraint that metal layers are at least 3 nm in thickness, we obtain the optimized structure considered in Fig. 3.2(b) and (c) (see radii below), operating at a light wavelength of 690 nm. Figure 3.2(b) illustrates that this structure is capable of concentrating the optical field near the core region, where the field-intensity enhancement exceeds 10^4. This is remarkable considering that light is impinging from outside the structure, so that it has to cross several metal layers to reach the core region. Incidentally, the intensity profile suggests a dominant effect of dipolar modes. As expected, this results in a substantial increase in temperature (Figure 3.2(c)), despite the fact that we are considering a moderate pump intensity of $1\,\mathrm{GW/m^2}$.

We note that this is an optimum structure from the thermal viewpoint, but it is not necessarily optimum from the optical view point. As an example, for the simple gold/silica coreshell nanoparticle depicted in Fig. 3.5(a), the radii of the optically-optimized structure are R_1=14 nm and R_2=17 nm, as shown in Fig. 3.4(a). However, the thermally-optimized structure corresponds to radii R_1=23 nm and R_2=28 nm, as shown in Fig. 3.4(b). As a further manifestation of the lack of direct connec-

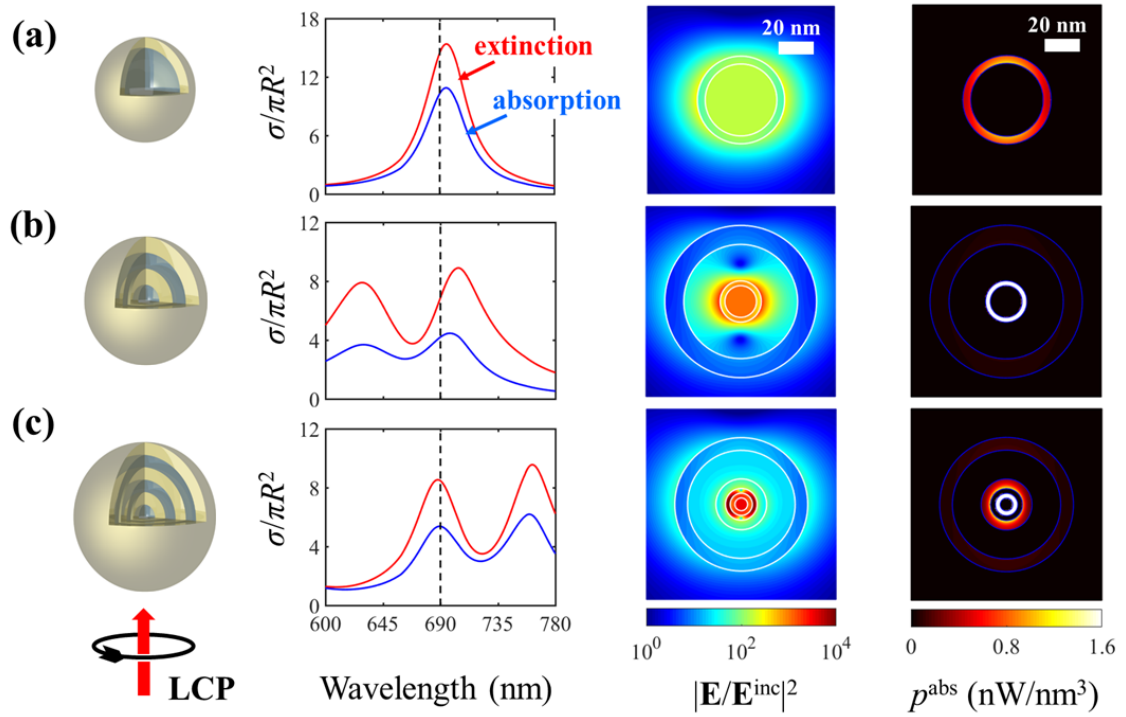

Figure 3.5: Optical and thermal properties of optimized nanoparticles with single (a), double (b), and triple (c) gold shells. In each row, we show from left to right a scheme of the nanoparticle, normalized extinction and absorption cross-section spectra, the electric near-field intensity distribution under plane-wave illumination at a wavelength of 690 nm, and the absorption power density p^{abs} generated at the same wavelength with a pump intensity of 1 GW/m^2. The power color scale is saturated at 1.6 nW/nm^3 for clarity.

tion between optimum heating and maximum field enhancement, we observe that the inner gold layer is the hottest one in Figure 3.2, but this is not where the field enhancement reaches its maximum.

Further insight into the effect of multiple layers can be gained by examining the behavior of systems with an increasing number of shells. We consider particles with $N = 1 - 3$ gold shells in Figure 3.5, optimized to operate at a fixed light wavelength of 690 nm. The radial distances at the gold/silica interfaces correspond to the numerical labels indicated in horizontal axes of Figure 3.7(a-c). The normalized extinction and absorption cross-sections (curves in Fig. 3.5) show that all three nanostructures present optical resonances around the targeted wavelength (vertical

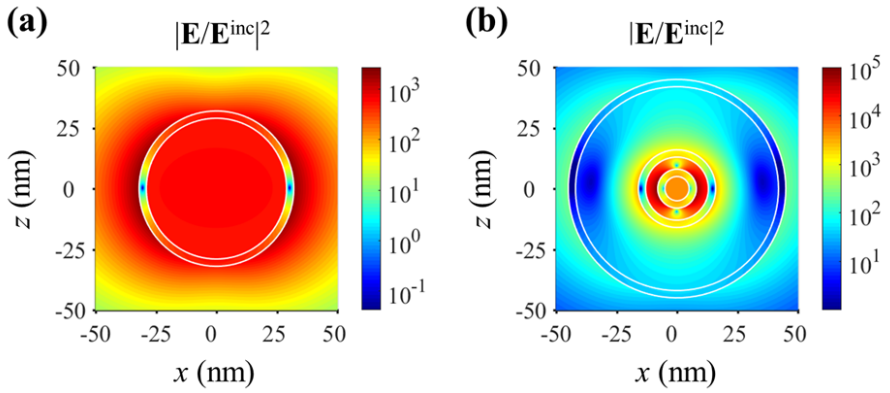

Figure 3.6: Optical field enhancement in silver/silica structures. We show the electric near-field intensity distributions at a wavelength of 690 nm for two optimized structures: a coreshell (a) and a multishell consisting of 3 silver layers (b).

dashed line). Inspection of the electric near-field distributions reveal that these are dipolar modes. Due to the cascading effect mentioned above, the maximum field enhancement increases with the number of gold shells, reaching a maximum $> 10^4$ for $N = 3$.

Incidentally, similar results are obtained by replaying gold by silver, but with much enhanced field enhancement. We show in Fig. 3.6 the electric near-field intensity distributions for a silver/silica coreshell and a $N = 3$ multishell, optimized to render maximum enhancement at a wavelength of 690 nm. The silver/silica interfaces are placed at radial distances of 29 nm and 32 nm in the coreshell, and 5 nm, 8 nm, 13 nm, 16 nm, 42 nm, and 45 nm in the multishell. Compared with the gold/silica structures of Fig. 3.5, we observe larger intensity enhancement using silver, reaching a maximum $> 10^5$. This ∼10-fold increase in intensity enhancement when moving from gold to silver is consistent with the ∼3-fold increase in Drude lifetime τ, and the scaling of the resonance near-field peak intensity as $\propto \tau^2$.

From the near-field intensity distributions, we readily calculate the generated heat power density using Eq (3.3). The results are shown in the rightmost plots of Figure 3.5 for a pump intensity of $1\,\mathrm{GW/m^2}$. The maximum of p^{abs} is ∼1-7-22 $\mathrm{nW/nm^3}$ for the $N = 1 - 2 - 3$ structures, demonstrating the expected cascading increase in heat power density with increasing N. This high heat power density, supplemented by the thermal barriers of the alternate metal/dielectric interfaces,

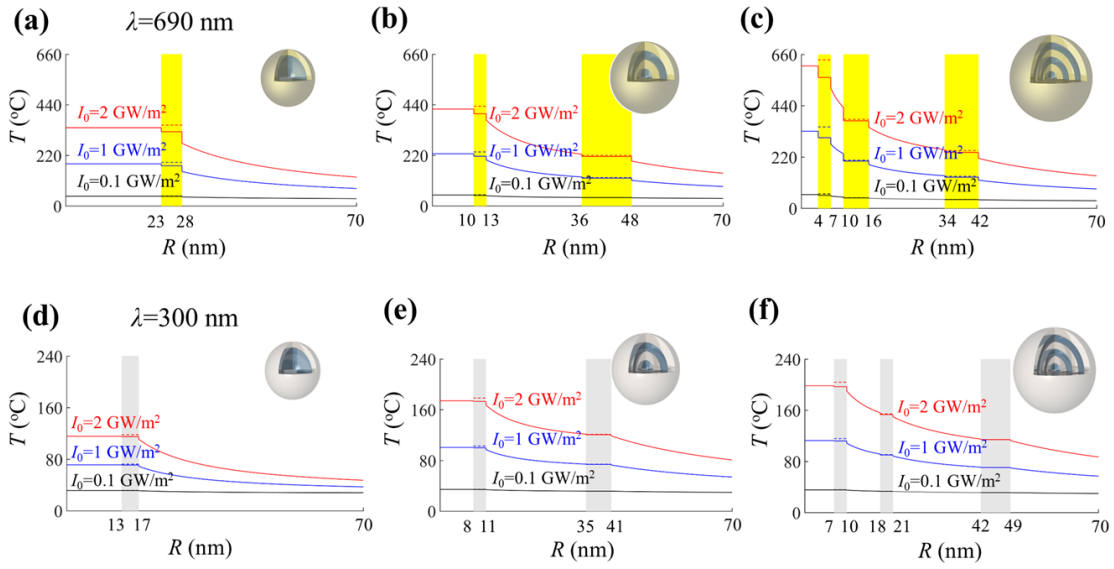

Figure 3.7: Temperature profiles of optimized nanospheres with single (a,d), double (b,e), and triple (c,f) metal shells under different external pump intensities. We show results for multishells made of gold (a-c) and aluminum (d-f), illuminated at a resonant light wavelegth of 690 nm and 300 nm, respectively. The electron (dashed curves) and phonon (solid curves) temperatures are assumed to be uniform within each metal shell (shadowed regions).

contributes to produce large temperature increase at the core.

In Fig. 3.7(a-c), we present calculated temperature profiles for the same three gold/silica nanoparticles as in Figure 3.5. Under constant pump power, the maximum temperature increases with the number of metal layers, leading to $\sim 600\,^{\circ}\mathrm{C}$ at the core of the $N = 3$ structure for a moderate pump intensity of $2\,\mathrm{GW/m^2}$ (Figure 3.7(c), red curve). Additionally, we observe a clear difference ($\sim 80\,^{\circ}\mathrm{C}$) between electron and temperatures in the innermost gold shell.

Smaller nanoparticles typically produce larger field enhancement, and therefore, also larger heat power generation; now, enlarging the size of the structure causes a reduction in field enhancement, which is however compensated by the increase in particle volume, leading to in some cases to higher total heat power. In order to make clear of these two competitive factors, we study in Fig. 3.8 the influence of the nano-oven geometrical parameters on its average field-intensity enhancement over the volume of the central silica core. More specifically, all the geometrical param-

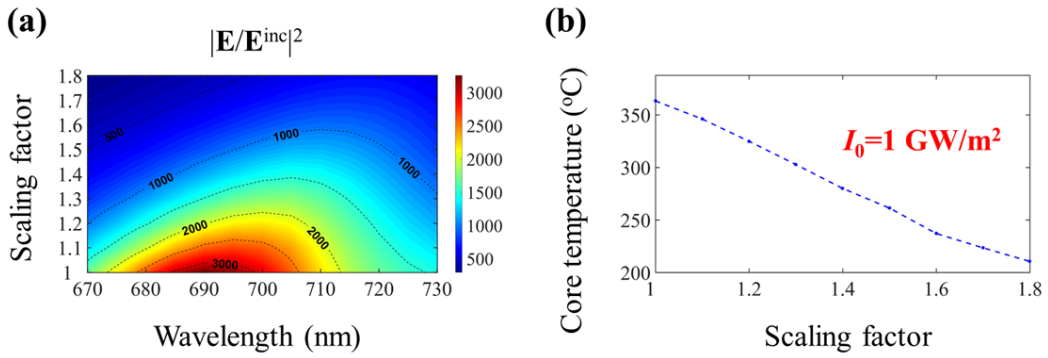

Figure 3.8: Dependence of the optical and thermal performances on particle size. (a) Electric-field-intensity enhancement averaged over the volume of the central silica core for nano-ovens like the one shown in Fig. 3.7(c), with all radii multiplied by a common scaling factor (vertical axis). (b) Temperature increase at the center of the nano-oven as a function of the scaling factor under an external pump intensity of 1 GW/m^2, tuned to the scaling-factor-dependent wavelength for which the enhancement is maximum.

eters of the nano-oven shown in Fig. 3.7(c) are scaled by a common factor ranging from 1 to 1.8. As the scaling factor increases, the resonance wavelength redshifts and the maximum value of the enhancement decreases. As a result, the temperature in the center of the nano-oven also decreases, even though the wavelength is tuned to the maximum value for each scaling factor.

Recently, aluminum has attracted much attention as a plasmonic material [154, 155, 156, 157] because it is abundant, low-cost, CMOS compatible, and operating at shorter wavelengths that can reach the UV regime, which can be important for photocatalytic processes [158, 159]. We present in Fig. 3.9 a similar study as in Fig. 3.5, but replacing gold by aluminum, and considering a new resonant incident light wavelength of 300 nm. We conclude that the field enhancements in the aluminum multishells are much weaker than those of their gold counterparts. Additionally, we find that both the central and outer aluminum shells operate more actively on the quadrupole modes, rather than the dipole modes. Because the TBC of aluminum/silica interfaces is much larger ($\sim$ 7-fold increase with respect to gold, see details in Appendix C), the temperature variations at multiple interfaces play a smaller role, so a bigger structure (no longer subwavelength) containing thicker dielectric shells would be needed to optimize the thermal performance. We further

examine in Figure 3.7(d-f) the performance of nano-ovens formed by aluminum/silica structures. The obtained temperature increase is lower than for gold under constant pump power, an effect that we attribute to both the weaker capability to of aluminum to confine the electric field and the large TBC. As shown in Figure 3.7(d-f), the high efficiency of heat conduction across the aluminum/silica interfaces substantially reduces the temperature jumps, and therefore, the temperature increase at the core mainly originates in the poor thermal conductance of the silica shells. Although the central temperature of the aluminum $N = 3$ nano-oven reaches $200\,^{\circ}\mathrm{C}$ under a pump power of $2\,\mathrm{GW/m^2}$, which is only one third of that in the gold nano-oven, it is still much higher than that in the aluminum coreshell structure, thus demonstrating its advantage to enhance the photothermal effect in the UV regime.

We anticipate that comparison of model calculations and future experiments could shed light into the different thermal parameters involved in the nano-oven, including the effect of nanostructuration and the role played by the detailed phonon dispersion relations [160]. Additionally, as shown in Fig. 3.10, we find our simulations to be rather robust with respect to two details of the thermal dissipation model: the assumption of two different temperatures in the electron and lattice systems of the metal; and the temperature dependence of the electron-lattice TBCs in the metal/dielectric interfaces. Figure 3.10(a) is copied from Fig. 3.7(c). In Fig. 3.10(b) we present results from a one-temperature model, obtained by setting the electron and lattice temperatures equal in the metal. The two- and one-temperature models lead to similar temperature profiles, and in particular, they predict a similar increase in temperature at the core region. Finally, because the experimental determination of TBCs is sensitive to sample preparation [161] and interfacial imperfections [162], possibly leading to smaller TBCs than those assumed in this work (see Appendix C fow the details), we analyze in Fig. 3.10(c) the effect of eliminating the temperature dependence in electron-lattice TBC by making these coefficients equal to a constant value, so that the total TBCs are given by $187\,\mathrm{MW\,m^{-2}\,K^{-1}}$, taken from Ref. [68]. Using this assumption together with the one-temperature model, a higher increase in temperature is predicted at the core region, as shown in Fig. 3.10(c), although the effect is not dramatic.

Beyond this work, we expect that there is plenty of room to further improve the performance of nano-ovens in terms of thermal management. For example, by

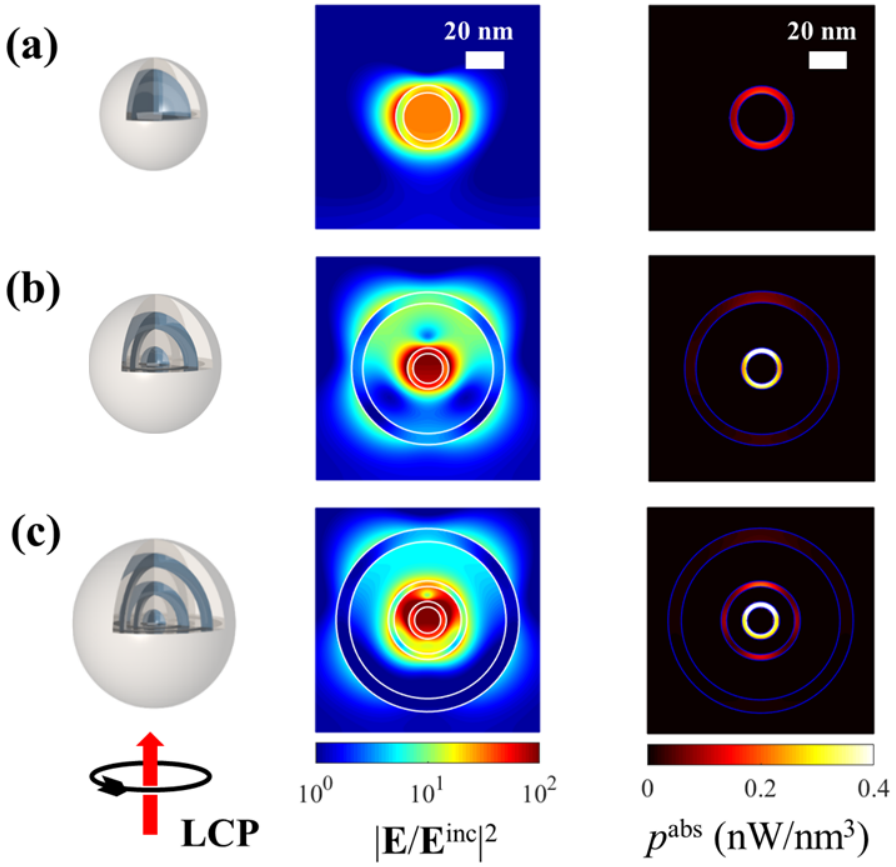

Figure 3.9: Optical and thermal properties of aluminum-based nano-ovens. We show results for optimized nanoparticles with single (a), double (b), and triple (c) aluminium shells for the same geometrical parameters as in Fig. 3.7(d-f). In each row, we show from left to right a scheme of the nanoparticle, the electric near-field intensity distribution under plane-wave illumination at a wavelength of 300 nm, and the absorption power density p_{abs} generated at the same wavelength with a pump intensity of $1\,\mathrm{GW/m^2}$.

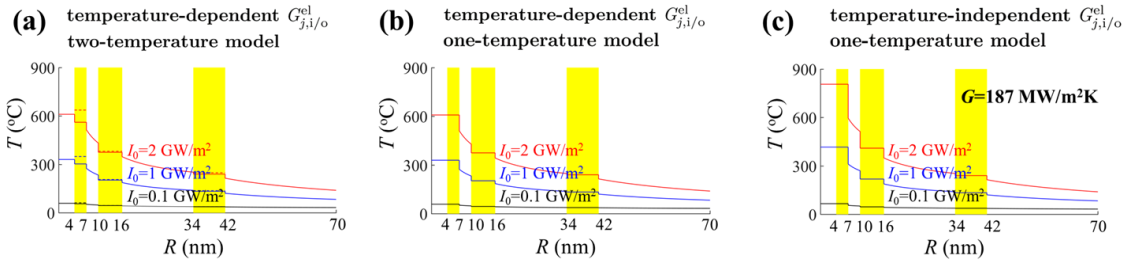

Figure 3.10: Model dependence of the calculated temperature profiles. We show calculated temperature profiles under different external pump intensities (see labels) for a gold/silica nano-oven using different models: (a) two-temperature model with temperature-dependent electron-lattice TBCs at the gold-silica interfaces (this panel is the same as Fig. 3.7(c)); (b) one-temperature model (*i.e.*, the electron and lattice temperatures are set equal in the metal regions) with temperature-dependent electron-lattice TBCs; (c) one-temperature model with a temperature-independent total TBCs of 187 $\mathrm{MW\,m^{-2}\,K^{-1}}$.

making rough interfaces [163] or by inserting organic molecules between otherwise closely attached metal/dielectric layers [164], one can significantly reduce the TBC, thus leading to higher temperature increases under constant light pumping intensity. A similar effect could be exploited in the outermost metal/water interface, for example by decorating it with hydrophobic groups [165, 166]. Additionally, the TBCs of interfaces formed by plasmonic metals and other dielectric materials beyond silica are only poorly known, thus demanding further exploration of their performance as nano-oven dielectrics, which could contribute to elucidate their thermal properties with application in the optimization of heat management in nanoscale devices.

3.3 Enhancement of the internal pressure

Each curved interface introduces a pressure difference due to the surface tension. For solid-liquid and liquid-liquid interfaces, this is the so-called Laplace pressure, the increase of which at the interface between media 1 and 2 is given by $2\gamma_{12}/R_{12}$, where R_{12} is the radius of curvature of the interface and γ_{12} is the interfacial energy. Instead, we are dealing with solid-solid interfaces, for which the expression above needs to be changed to $\Delta p_{\mathrm{intrinsic}} = 2\gamma_{12}/R_{12} + C$, where both C and γ_{12} can be

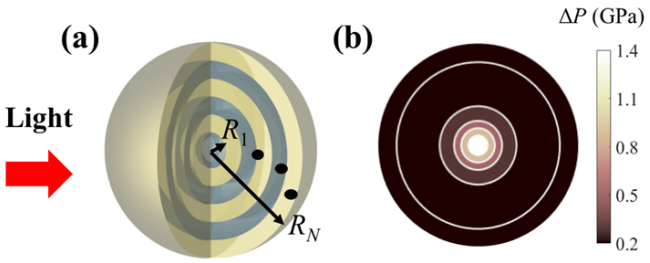

Figure 3.11: (a) Schematic view of the plasmonic nano-oven. (b) Lifted internal pressure. The incident light has an intensity of $1\,\mathrm{GW/m^2}$ and a wavelength of 690 nm.

expressed in terms of the shear modulus of the outer medium G, the bulk modulus of the inner medium K, and the stress of the interface h, as discussed in the literature [167, 168]. More precisely, $\gamma_{12} = mh$, where $m = 1/(1 + 4G/3K)$, while $C = 4m\varepsilon G$ originates in the deformation of the interface, with a characteristic strain that depends on actual size [168] (we take $\varepsilon \sim -0.0017$ as an average value valid for the nanometer-sized layers). Plugging values for gold [169] ($G_{\mathrm{gold}} = 27\,\mathrm{GPa}$, $K_{\mathrm{gold}} = 180\,\mathrm{GPa}$) and silica [170] ($G_{\mathrm{silica}} = 31\,\mathrm{GPa}$, $K_{\mathrm{silica}} = 37\,\mathrm{GPa}$), and using a typical stress $h \sim 1\,\mathrm{N/m}$ [168], we find $\gamma_{12} = 0.8\,\mathrm{N/m}$ and $C = -0.2\,\mathrm{GPa}$ for a gold/silica (inner/outer) interface, and $\gamma_{12} = 0.5\,\mathrm{N/m}$ and $C = -0.1\,\mathrm{GPa}$ for a silica/gold one. Both the constant and the $1/R_{12}$ terms of this intrinsic pressure contribute with values of the order of the GPa. Another major source of pressure originates in thermal stress, which has been recently measured in core-sell nanoparticles [171]. Because the linear thermal expansion coefficient β is about 25 times larger in gold than in silica, we can neglect the effect of the dielectric and estimate this source of pressure increase as $\Delta p_{\mathrm{thermal}} = 3\beta_{\mathrm{gold}}(T_{\mathrm{gold}} - T_0)K_{\mathrm{gold}}$ using $\beta_{\mathrm{Au}} = 14.2 \times 10^{-6}\,\mathrm{K^{-1}}$ [171] (*e.g.*, we have $\Delta p_{\mathrm{thermal}} \sim 4\,\mathrm{GPa}$ for $T_{\mathrm{gold}} - T_0 = 500\,\mathrm{K}$). The expression $\Delta p_{\mathrm{intrinsic}} + \Delta p_{\mathrm{thermal}}$ is used in this work to estimate the concatenated increases of pressure in Figure 3.11. Incidentally, $\Delta p_{\mathrm{thermal}}$ is dismissed for the outermost layer because it can freely expand.

The large internal pressure combined with the high temperature can has important potential applications. As a specific example, the polymerization of cyanogen, which is a rather toxic substance in its standard phase, requires high pressure (∼GPa) and temperature (∼ 400 °C), which are typically achieved in a

diamond anvil cell (DAC) [172, 173]. When using the nano-oven, the reaction of cyanogen polymerization could take place inside the core region, which is isolated from the environment. Importantly, this reaction could be triggered using a moderate input light power, thus resulting in higher energy efficiency than with DAC-based methods.

3.4 Conclusions

In summary, in the first part of this chapter, we explore using dielectric@metal coreshell nanoparticles to enhance the emission intensities of UCNPs located in the center of dielectric cores. Optimal structures are found under different pump conditions with realistic parameters. This study can guide the rational synthesis of interested structures in experiments.

In the second part, we have designed an optimized plasmonic nano-oven based upon gold/silica multishells driven by visible light. Compared with a conventional coreshell nanoparticle, our proposed nano-oven is capable of simultaneously producing a huge electric field enhancement, a large temperature increase under moderate pump intensities, and a large pressure in the core region. The extreme conditions created at the core of nano-ovens provide a fantastic platform for the study of physical and chemical processes in which cooperative optical-field-, temperature-, and pressure-driven effects can take place [174, 175, 176, 177]. For example, band gaps and fluorescence intensities of organic and inorganic crystals can be tuned by applying different levels of pressure [174, 175, 176]. Also some phase transitions occur under extreme pressure and temperature conditions [177]. These effects could have potential application to optical memories, as already explored for homogeneous gallium nanoparticles [178]. The study of these types of transitions taking place at the core of nano-ovens could be facilitated by the availability of colloid methods for the synthesis of the multishells under consideration [179]. As a related direction for exploration, phase transitions in the multishells themselves should result in even more dramatic changes in pressure. Similar to what has been recently demonstrated for larger multi-particle structures [73, 74], a single multishell could eventually explode like a nanobomb, ignited for example by an intense pump laser pulse, which could be used to kill cancer cells.

Chapter 4

Control of light scattering using atom arrays

In this chapter, we explore the ability of two-dimensional periodic atom arrays to control light scattering, and specifically produce light amplification. We develop an analytical theory for three-level scatterers, which reveals a rich interplay between lattice and atomic resonances. Our results provide a general background to understand interaction between light and periodic atomic arrays, with promising applications in the manipulation and control of coherent photon states at the nanoscale. In the following, we first present an introduction that motivates this study, which is followed by detailed computations of light reflection and transmission of three-level atom arrays.

4.1 Introduction

As partially mentioned in the introduction of this thesis, section 1.4, periodic arrays of light scatterers have the ability to enhance the optical near-field intensity due to the accumulation of in-phase scattering wave components. This is neatly illustrated by an infinite linear array of point scatterers illuminated with a plane wave of momentum and electric field both perpendicular to the array direction [180]: the field induced on any given scatterer by the rest of the array diverges as the series $1 + 1/2 + 1/3 + \dots$ when the wavelength is equal to the period; this divergence

prevents the induction of polarization on the scatterers, thus rendering the array invisible under these conditions. Such types of lattice-sum divergences lead to Wood's anomalies [107, 181], extraordinary optical transmission [85], complete optical reflection, and large near-field enhancement, which are phenomena generally describable in terms of lattice resonances [27]. Interestingly, complete reflection is observed even in the limit of small scatterers at the cost of narrowing down the spectral features and lowering their tolerance to structural defects [182, 183].

A good example of small scatterers is provided by lossless quantum emitters incorporating two nondegenerate electronic levels, which are well-known to offer an optical cross-section $3\lambda^2/2\pi$ for light of wavelength λ. For a properly designed focused light beam, an individual atom is predicted to produce complete reflection [184], while an experimental realization of this idea has achieved $> 10\%$ extinction by an individual 2-level molecule [185]. A similar effect takes place in one-dimensional waveguides, where a single 2-level scatterer also leads to complete reflection [186]. Likewise, the ability of two-dimensional (2D) arrays of small scatterers to produce complete reflection [182] has been theoretically illustrated by considering 2-level quantum emitters [86], again relying on lattice resonances [27].

In a different context, optical gain, as introduced in section 1.5, has attracted great interests in nanophotonic community. There are lots of works in studying interactions between assembles of active quantum emitters and plasmonic nanostructures in a macroscopic manner [92, 93, 94, 95, 96, 97, 98, 99, 100]. Arranging these microscopic active emitters into regular arrays should produce interesting interplay between lattice and atomic resonances with gain.

In the following, we investigate light scattering in 2D periodic arrays of externally-pumped 3-level atoms. Specifically, we calculate light reflection and transmission coefficients, revealing rich phenomena with various pump strengths and lattice periods. We reach these results by formulating an analytical model in which the atoms are described through their polarizability obtained from a density-matrix formalism including gain, while the array periodicity enters through dipole-dipole lattice sums.

4.2 Light reflection/transmission on atom arrays

In this work, we consider 3-level identical atoms (electronic energies $\hbar\varepsilon_1 < \hbar\varepsilon_2 < \hbar\varepsilon_3$, see Fig. 4.1(b)) arranged into a rangular 2D array (see Fig. 4.1(a)) under resonant pump illumination at frequency $\omega' = \varepsilon_3 - \varepsilon_1$. Following pumping from level 1 to 3, we assume the system to rapidly decay nonradiatively from 3 to 2. We are interested in the subsequent radiative decay from 2 to the ground state 1, which affects the scattering of light near the resonance frequency $\omega_0 = \varepsilon_2 - \varepsilon_1$.

A general quantum mechanical method to describle atoms interacting with photons have been introduced in Appendix D. Here, for completeness, we will recall it in a brief manner. Then, the lattice sum and a derivation of reflection coefficient are presented. Combine these knowledges with polarizability of atoms as well as electromagnetic Green tensor in Appendix E, we proceed to compute light reflectance, transmittance, and absorbance of 2D atom arrays.

The internal temporal dynamics of the atoms in the array is governed by the Hamiltonian $\mathcal{H}(t) = \mathcal{H}^{\rm at} + \mathcal{H}^{\rm rad} + \mathcal{H}^{\rm at-rad} + \mathcal{H}^{\rm ext}(t)$, where $\mathcal{H}^{\rm at} = \hbar\sum_{li}\varepsilon_i|li\rangle\langle li|$ and $\mathcal{H}^{\rm rad} = \hbar\sum_n \omega_n a_n^\dagger a_n$ describe the free atoms (electronic states $|li\rangle$ with $i = 1-3$ for each of the atoms l at positions $\mathbf{r}_l$) and radiation (photon modes n with creation and annihilation operators $a_n^\dagger$ and a_n), the term $\mathcal{H}^{\rm at-rad} = \sum_{nlii'}(g^*_{nlii'}a_n^\dagger + g_{nlii'}a_n)(\sigma^\dagger_{lii'} + \sigma_{lii'})$ accounts for light-atom interaction (coupling coefficients $g_{nlii'}$), $\mathcal{H}^{\rm ext}(t) = -\sum_{lii'}\mathbf{d}_{ii'}\cdot\mathbf{E}^{\rm ext}_l(t)(\sigma^\dagger_{lii'} + \sigma_{lii'})$ represents the interaction with the external field $\mathbf{E}^{\rm ext}_l(t) = \mathbf{E}^{\rm pump}(\mathbf{r}_l)\mathrm{e}^{-\mathrm{i}\omega' t} + \mathbf{E}^{\rm probe}_l\mathrm{e}^{-\mathrm{i}\omega t} + \text{c.c.}$ [pump and local probe at frequencies ω' and ω], and we have defined atomic-transition operators $\sigma_{lii'} = |li\rangle\langle li'|$ and their corresponding dipole elements $\mathbf{d}_{ii'} = -e\langle li|\mathbf{r} - \mathbf{r}_l|li'\rangle$ (independent of l).

We treat the external field semi-classically and assume that the emitted photons are excited into coherent states [187, 188, 189] (see section 1.5 for more details). This approximation allows us to factorize the density matrix of the entire system as the product of radiation and atomic subsystems $\rho = \rho^{\rm rad}\otimes\Pi_l\rho_l^{\rm at}$, substitute the photon operators by their complex-number expectation values, and write a self-contained equation of motion for each atom l as $\dot\rho_l^{\rm at} = (\mathrm{i}/\hbar)[\rho_l^{\rm at}, \mathcal{H}(t)] + \mathcal{L}[\rho_l^{\rm at}]$, where the Lindblad term $\mathcal{L}[\rho_l^{\rm at}] = \sum_{ii'}(\gamma_{ii'}/2)\left(2\sigma_{li'i}\rho_l^{\rm at}\sigma^\dagger_{li'i} - \sigma^\dagger_{li'i}\sigma_{li'i}\rho_l^{\rm at} - \rho_l^{\rm at}\sigma^\dagger_{li'i}\sigma_{li'i}\right)$ describes

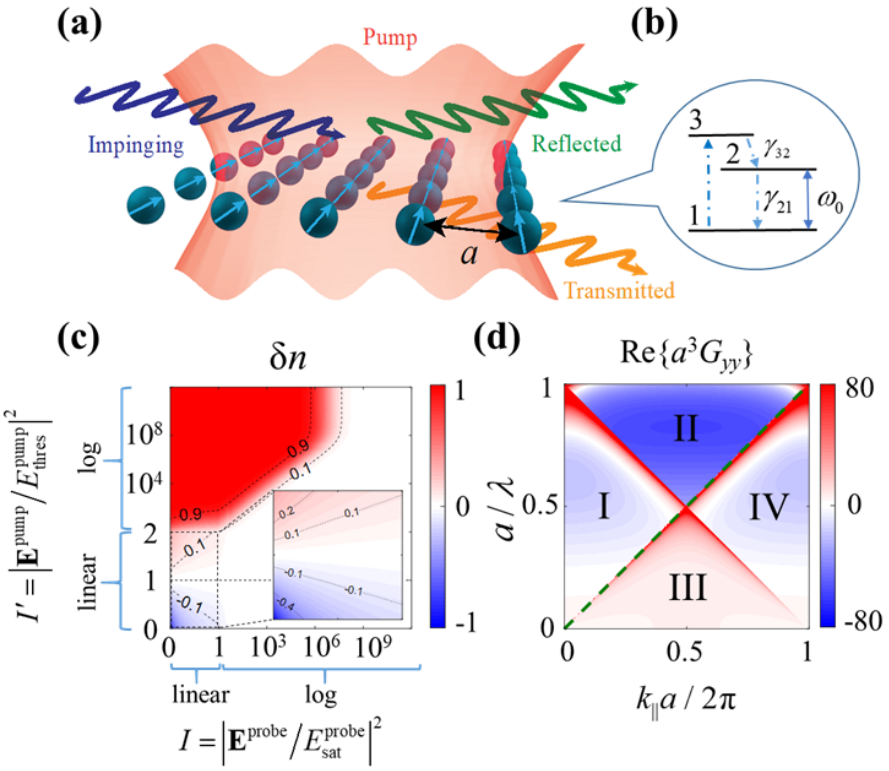

Figure 4.1: (a) Schematic view of a 2D square array (period a) of point scatterers with gain, pumped and probed with light plane waves of field amplitudes $\mathbf{E}^{\text{pump}}$ and $\mathbf{E}^{\text{probe}}$, respectively. (b) Energy diagram of a 3-level individual emitter defining the optical transition of frequency ω_0 and the nonradiative damping rates γ_{21} and γ_{32}. c Population difference δn of the system in (b) as a function of normalized pump and probe intensities. The inset is a zoom of the low-intensity region. d Dipole lattice sum $\text{Re}\{a^3 G_{yy}(\mathbf{k}_{||}, \omega)$ for polarization along y as a function of light wavelength λ and parallel wave vector $\mathbf{k}_{||} = k_{||}\hat{\mathbf{x}}$ along the x direction.

nonradiative $i \to i'$ transitions (in practice, we only include $3 \to 2$ and $2 \to 1$ at rates γ_{32} and γ_{21}, see Fig. 4.1(b)).

At this point, we assume a uniform pump acting with the same strength on all atoms and an incident probe plane wave having a wave vector component $\mathbf{k}_{||}$ parallel to the array [1]. This wave vector is inherited by the linearly induced dipoles $\mathbf{p}_l$, where the dependence on in-plane atom position $\mathbf{r}_l = (x_l, y_l, 0)$ comes from both the spatial variation of the external field and the relative atomic arrangement. Following a well-established procedure [27, 39], the component of the induced dipoles at the probe frequency ω reduces to $\mathbf{p}_l = \mathbf{p}\, \mathrm{e}^{\mathrm{i}\mathbf{k}_{||}\cdot\mathbf{r}_l - \mathrm{i}\omega t} + \text{c.c.}$, where $\mathbf{p} = \alpha(\omega) \cdot \mathbf{E}_0^{\mathrm{loc}}$ is a position-independent dipole amplitude (evaluated from the local probe field acting on the atom at position $\mathbf{r}_{l=0} = 0$) and $\alpha(\omega)$ is the atomic polarizability tensor. Additionally, $\mathbf{E}_0^{\mathrm{loc}}$ is the sum of the incident probe $\mathbf{E}^{\mathrm{probe}}(0)$ and the field induced by the rest of the atoms, which admits the self-consistent form [27, 39] $\mathbf{E}_0^{\mathrm{loc}} = \Big[1 - G(\mathbf{k}_{||}, \omega) \cdot \alpha(\omega)\Big]^{-1} \cdot \mathbf{E}^{\mathrm{probe}}(0)$, where $G(\mathbf{k}_{||}, \omega) = \sum_{l\neq 0} [\omega^2/c^2 + \nabla_{\mathbf{r}_l} \otimes \nabla_{\mathbf{r}_l}] \mathrm{e}^{\mathrm{i}\mathbf{k}_{||}\cdot\mathbf{r}_l}/r_l$ is a lattice sum that describes the electromagnetic dipole-dipole interactions, excluding self interactions ($l = 0$ term).

The atomic polarizability is affected by the pump through changes in the population difference $\delta n = \rho_{22}^{\mathrm{at}} - \rho_{11}^{\mathrm{at}}$. (Note that under the assumed conditions all atoms are equally pumped, so their populations are independent of l.) A detailed nonperturbative solution of the equations of motion for the component of frequency ω under the rotating-wave approximation and neglecting higher-order harmonics allows us to obtain the induced dipoles directly from the expectation values $\mathbf{p} = \sum_{ii'} \mathbf{d}_{ii'} \mathrm{tr}\{\rho_{l=0}^{\mathrm{at}} (\sigma_{ii'}^{\dagger} + \sigma_{ii'})\}$, from which the atomic polarizability is found to be (see Appendix D for a detailed derivation)

$$\alpha^{-1}(\omega) = \left[\frac{2\omega_0 \delta n}{\hbar} \frac{\mathbf{d}_{12} \otimes \mathbf{d}_{12}}{(\omega + \mathrm{i}\gamma_{21}/2)^2 - \omega_0^2}\right]^{-1} - \frac{2\mathrm{i}\omega^3}{3c^3},$$

where the last term originates in the imaginary part of the dipole self-interaction, while the real part of this term is effectively absorbed as a vacuum resonance-frequency shift [190]. The population difference admits an involved analytical expression that is derived in the Appendix D. It is however illustrative to consider

[1] We neglect interatomic interactions at the pump frequency because the corresponing atomic polarizability issmall under the assumption of large γ_{32}.

the $\gamma_{32} \gg \gamma_{21}$ limit near resonant probe illumination conditions ($\delta = \omega - \omega_0 \ll \omega_0$), which permits us to write

$$\delta n = \frac{-1 + \mathcal{I}'}{1 + 8\mathcal{I}(1 + 3\mathcal{I}'\gamma_{21}/2\gamma_{32})/(1 + 4\delta^2/\gamma_{21}^2) + \mathcal{I}'}.$$

Here, $\mathcal{I}' = |\mathbf{E}^{\rm pump}/E_{\rm thres}^{\rm pump}|^2$ and $\mathcal{I} = \left|\mathbf{E}^{\rm probe}/E_{\rm sat}^{\rm probe}\right|^2$ are the pump and local probe field intensities normalized to their respective threshold and saturation values $E_{\rm thres}^{\rm pump} = 2\hbar\sqrt{\gamma_{21}\gamma_{32}}/d_{13}$ and $E_{\rm sat}^{\rm probe} = \hbar\gamma_{21}/d_{12}$, respectively. We plot δn for $\omega = \omega_0$ in Fig. 4.1(c), which shows that the full range $\delta n \in [-1, 1]$ is reached. In what follows, we use δn as an input parameter controlled by the combination of pump and probe intensities.

For concreteness, we consider a planar atom array sitting in the $z = 0$ plane and having specular symmetry relative to the $x = 0$ plane. For simplicity, we assume that the atoms can only be polarized along y (*i.e.*, all induced dipoles $\mathbf{p}_l = p_l\,\hat{\mathbf{y}}$ are collinear and oriented along y). Under illumination by a plane wave, we then need to consider the incident electric-field component in the $z = 0$ plane $E_y^{\rm probe}(x, y, 0, t) = E_y^{\rm probe} \mathrm{e}^{\mathrm{i}\mathbf{k}_{||}\cdot\mathbf{R} - \mathrm{i}\omega t} + \text{c.c.}$, where ω is the frequency, $\mathbf{k}_{||} = (k_x, k_y)$ is the parallel component of the wave vector, and we use the notation $\mathbf{R} = (x, y)$.

Using Eq. (E.17) and the methods described in more detail in Refs. [27, 39], the induced dipole moment can be written as $p_l = p\,\mathrm{e}^{\mathrm{i}\mathbf{k}_{||}\cdot\mathbf{R}_l}$ with amplitude

$$p = \frac{E^{\rm probe}}{1/\alpha(\omega) - G_{yy}(\mathbf{k}_{||}, \omega)}, \tag{4.1}$$

where $G_{yy}(\mathbf{k}_{||}, \omega)$ is the yy component of

$$G(\mathbf{k}_{||}, \omega) = \sum_{l \neq 0} \mathcal{G}(\mathbf{R}_l)\,\mathrm{e}^{-\mathrm{i}\mathbf{k}_{||}\cdot\mathbf{R}_l}, \tag{4.2}$$

in which the sum runs over atomic lattice sites $\mathbf{R}_l$, omitting the atom at the origin $\mathbf{R}_{l=0} = 0$. We now introduce the identities

$$\frac{\mathrm{e}^{\mathrm{i}kr}}{r} = \mathrm{i}\int \frac{d^2\mathbf{Q}}{2\pi k_\perp^Q}\mathrm{e}^{\mathrm{i}\mathbf{Q}\cdot\mathbf{R}+\mathrm{i}k_\perp^Q|z|}, \tag{4.3a}$$

$$\sum_l \mathrm{e}^{\mathrm{i}\mathbf{Q}\cdot\mathbf{R}_l} = \frac{(2\pi)^2}{A}\sum_{\mathbf{g}}\delta(\mathbf{Q}-\mathbf{g}), \tag{4.3b}$$

where $\mathbf{Q} = (Q_x, Q_y)$ is a 2D wave vector, $\mathbf{g}$ runs over 2D reciprocal lattice vectors, A is the unit-cell area,

$$k_\perp^Q = \sqrt{k^2 - Q^2 + i0^+},$$

and the square root is taken to yield a positive imaginary part. Making use of Eqs. (E.16) and 4.3 for the evaluation of Eq. (4.2), we find [27, 39]

$$G_{yy}(\mathbf{k}_{||},\omega) = \lim_{z\to 0}\left[\sum_{\mathbf{g}}\frac{2\pi\mathrm{i}}{Ak_\perp^{|\mathbf{k}_{||}+\mathbf{g}|}}\exp\left(\mathrm{i}k_\perp^{|\mathbf{k}_{||}+\mathbf{g}|}|z|\right)\left[k^2-(k_y+g_y)^2\right] - \mathrm{i}\int\frac{d^2\mathbf{Q}}{2\pi k_\perp^Q}\mathrm{e}^{\mathrm{i}k_\perp^Q|z|}(k^2-Q_y^2)\right]. \tag{4.4}$$

Upon inspection of Eq. (4.4), we find that the imaginary part of $G_{yy}(\mathbf{k}_{||},\omega)$ can be obtained analytically [27, 39] as

$$\mathrm{Im}\{G_{yy}(\mathbf{k}_{||},\omega)\} = \frac{2\pi}{A}\sum_{\mathbf{g}}\mathrm{Re}\left\{\frac{[k^2-(k_y+g_y)^2]}{\sqrt{k^2-|\mathbf{k}_{||}+\mathbf{g}|^2}}\right\} - 2k^3/3, \tag{4.5}$$

while the remaining real part needs to be calculated numerically. The convergence of the series in Eq. (4.2) is however slow, so we use the dedicated methods developed by Kambe [191] in the context of low-energy electron diffraction.

The reflectance of the array can be now obtained by noticing that the electric field generated by an individual dipole $\mathbf{p}$ placed at the origin is given by

$$\mathbf{E}^{\mathrm{dip}} = [k^2\mathbf{p} + (\mathbf{p}\cdot\nabla)\nabla]\frac{\mathrm{e}^{\mathrm{i}kr}}{r} \tag{4.6}$$

(see Eq. (E.16)). Summing over all dipoles in the array and using Eqs. (4.3), the reflected field reduces to

$$\begin{aligned}\mathbf{E}^{\text{ref}} &= \mathrm{i}p \sum_l \int \frac{d^2\mathbf{Q}}{2\pi k_\perp^Q} \mathrm{e}^{\mathrm{i}\mathbf{Q}\cdot(\mathbf{R}-\mathbf{R}_l)+\mathrm{i}k_\perp^Q|z|} \mathrm{e}^{\mathrm{i}\mathbf{k}_{||}\cdot\mathbf{E}_l} \left[k^2\hat{\mathbf{y}} - Q_y\left(\mathbf{Q} + \mathrm{sign}\{z\}k_\perp^Q\hat{\mathbf{z}}\right)\right] \\ &= \mathrm{i}p \sum_{\mathbf{g}} \mathbf{S}_{\mathbf{g}} \exp\left[\mathrm{i}(\mathbf{k}_{||}+\mathbf{g})\cdot\mathbf{R} + \mathrm{i}k_\perp^{|\mathbf{k}_{||}+\mathbf{g}|}|z|\right],\end{aligned}$$

where

$$\mathbf{S}_{\mathbf{g}} = \frac{2\pi}{Ak_\perp^{|\mathbf{k}_{||}+\mathbf{g}|}} \left[k^2\hat{\mathbf{y}} - (k_y+g_y)\left(\mathbf{k}_{||}+\mathbf{g}+\mathrm{sign}\{z\}k_\perp^{|\mathbf{k}_{||}+\mathbf{g}|}\hat{\mathbf{z}}\right)\right].$$

For specular reflection ($\mathbf{g}=0$), we have

$$\mathbf{S}_0 = \frac{2\pi}{Ak_\perp^{k_{||}}} \left[k^2\hat{\mathbf{y}} - k_y(\mathbf{k}_{||} + \mathrm{sign}zk_\perp^{k_{||}}\hat{\mathbf{z}})\right].$$

Because the dipoles are all oriented along y regardless of the orientation of the incidence field, the array will reflect cross-polarized beams in general, unless $\mathbf{k}_{||}$ is directed along a symmetry direction of the array. For in/out s-polarization, the reflection coefficient reduces to

$$r = \frac{\mathrm{i}S}{1/\alpha(\omega) - G_{yy}(\mathbf{k}_{||},\omega)}, \tag{4.7}$$

where $S = 2\pi k^2/Ak_\perp^{k_{||}}$. The transmission coefficient $t = 1+r$, and absorbance $A = 1-|r|^2-|t|^2$. These coefficients are dominated by the $\omega=\omega_0$ pole of $\alpha(\omega)$ and the lattice resonances of $G_{yy}(\mathbf{k}_{||},\omega)$, the real part of which is plotted in Fig. 4.1(d).

We plot in Fig. 4.2(a,b,c), respectively, reflectance ($R=|r|^2$), transmittance ($T=|t|^2$), and absorbance under normal incidence as a function of δn and a/λ_0. We assume a small nonradiative decay rate $\gamma_{21} = 0.01\,\gamma_0$ compared with the natural radiative decay rate $\gamma_0 = 4\omega_0^3 d_{12}^2/3\hbar c^3$. The shared colorbar is shown in Fig. 4.2(a). It is saturated at -2 and 2 for visual convenience. Figure 4.2(d,e,f) show the values at vertical cut lines in Fig. 4.2(a,b,c) with the same color codes. We can conclude that by tuning the population inversion δn via the external pump light strength, the scattering properties of probe light can be dynamically controlled. Specifically,

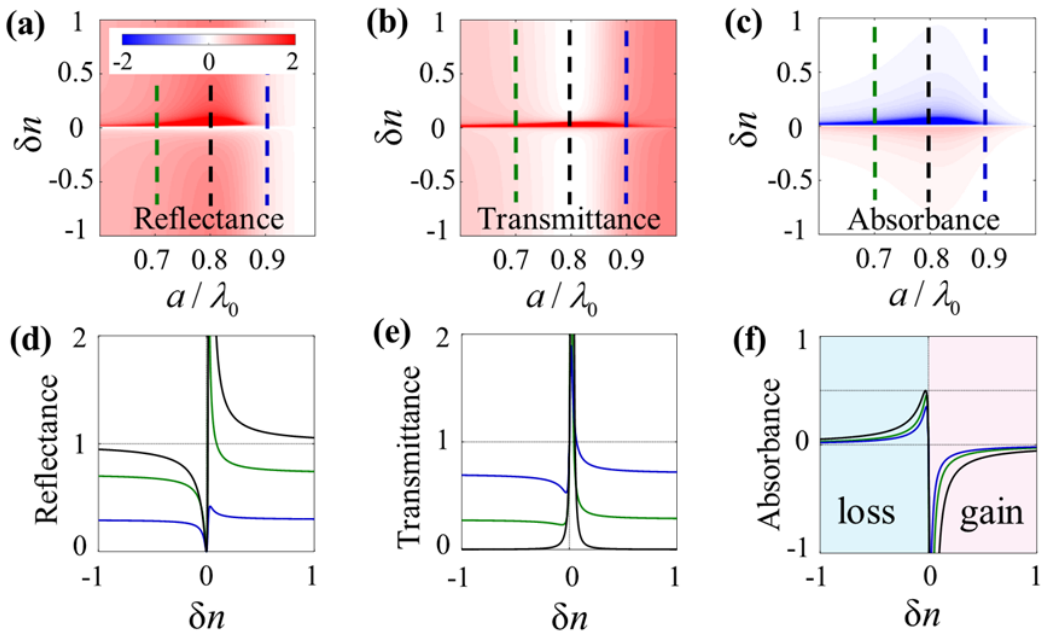

Figure 4.2: (a-c) Reflectance, transmittance, and absorbance under normal-incidence resonant-wavelength ($\lambda = \lambda_0 = 2\pi c/\omega_0$) probe illumination conditions as a function of population difference δn and period-to-wavelength ratio a/λ_0. (d-f) Cuts through (a-c) along the indicated vertical dashed lines with the same color code. We take the ratio between nonradiative and radiative scatterer decay rates to be $\gamma_{21}/\gamma_0 = 0.01$ in all plots.

when the pump light is relatively samll ($-1 < \delta n < 0$), the system is dissipative for probe light. Both the values of R and T are within [0,1], and the values of A are within [0,0.5]. We emphasis that nearly perfect reflection is reached when $\delta n = -1$, *i.e.*, no pump light. In this condition, the three-level atoms behave like two-level atoms. Incidentally, complete reflection can be realized if γ_{21} is assumed to be zero, which is the key result in Ref. [86]. Also, 0.5 is the upper limit of absorbance of a free-standing optically thin material [39]. When the pump strength is enhanced to make the system enter into gain region (see Fig. 4.2(f)), both the R and T can be highly amplified, leading to a peak of negative absorbance. This is signalled by a minimum of $|1/\alpha - G_{yy}|$ (*i.e.*, a lattice resonance, see Eq. (4.7)).

4.3 Conclusions

Our study demonstrates a vivid picture of interplay between lattice resonance and externally pumped atoms. Interesting phenomena for probe light, such as nearly total reflection, maximum absorption, complete transmission, and large amplification can be realized in a single platform by tuning pump intensity. These results have general applicability to 3-level ultracold atoms trapped in arrays, which can now be configured on demand [192]. Also, they can be readily extended to other atomic electronic structures, or even to particles containing a large number N of optically pumped atoms, for which the effective atomic radiative decay rate γ_0 is simply multiplied by a factor N. In a different context, atomically thin transition metal dichalcogenides (TMDs) host strong localized quantum emitters [193, 194] that could be eventually arranged in periodic arrays to provide a robust implementation of these ideas. A different possibility could rely on the strong scattering offered by single-layer TMD excitons [195, 196], in which periodic modulation could be introduced through defects [197], electrical gating [198], or structured optical pumping. Quantum dots offer yet another platform, which can also be strain-induced periodically [199]. A more classical realization would consist of macroscopic metamaterials operating at lower frequencies [200], which could incorporate gain through active electronic circuits (meta-atoms).

Chapter 5

Conclusions

In this thesis, we have carried out several theoretical studies of geometrical and gain effects in nanophotonics. We present an overall conclusion of these works and discuss related perspective in this final chapter.

In Chapter 1, we start with theoretical descriptions of both SPPs and LSPs, which are followed by introductions covering various topics (*i.e.*, absorber, photothermal effect, particle array, and gain) on which this thesis focuses.

In the first part of Chapter 2, we design a grating with shallow grooves that perfectly dissipates incoming light within an ultranarrow band. We further demonstrate it as a coherent thermal emitter and recover its potential application for very sensitive index sensing. This grating-based absorber as well as many other kinds of ultra-narrow band absorbers rely on delocalized resonances, which limit minimization of their spatial sizes. In order to address this problem, in the second part of the chapter, we propose a general method to guide rational design of narrow band absorbers but with small footprints. The method is assisted by incorporating gain media to partially compensate the loss in metal constituents, which provide the possibility to dynamically tune the performance via pumping. We apply it in designing three absorbers with different absorption mechanisms. The advantage of their applications for sensing compared with their fundamental-mode counterparts are also discussed. Beyond the scope of this work, we anticipate that adopting pure dielectric structures might eliminate the use of gain, which will make devices simpler.

In the first part of Chapter 3, we study the strategy of using metallodielectric

coreshell nanospheres to enhance emission intensities of upconversion nanoparticles embedded in the core. Optimized structures are identified under different excitation power regimes using realistic material parameters. In the second part, we proceed to investigate more complex multilayer nanospheres. Remarkable properties of field enhancements and internal temperature/pressure increases are revealed. Particularly, we include thermal boundary conductance (TBC) in the study of photothermal effect, and point out its important role. But, the reliable data of TBC of different materials in different temperature regimes is scarce. So, in the future, more accurate measurements of TBC values of nanostructures that chemically synthesized are highly needed. In addition, experimental implementations of the theoretical work are desired to test some appealing predictions, such as nanobomb for cancer therapy.

In Chapter 4, we study probe light interacting with externally pumped regular three-level atom arrays. We treat the electric field semi-classically and the atoms quantum-mechanically. A rich interplay between lattice and atomic resonances is predicted. It is found that for certain values of the lattice constant, an atom array can dynamically display nearly perfect reflection, maximum absorption, complete transmission, and large amplification of probe light, which is realized through tuning the pump strength, and therefore through the population inversion. Now, researchers are already able to manipulate atoms in vacuum and arrange them into regular arrays, therefore suggesting a possible venue for the demonstration of our ideas. In a different context, periodic quantum emitters in two-dimensional materials and periodic meta-atoms with gain might provide another two simpler platforms to test our theory and realize atomically-thin light amplifiers.

Appendix A

Generalized Mie theory

A.1 Interaction between multilayer cylinders and plane waves

In this section, we present an analytical method to study the interaction between coreshell/multilayer cylinders and plane waves. This method is used in section 2.2 to fastly optimize absorption cross-sections of the coreshell cylinders. Here, we are only interested in TM modes, *i.e.*, the impinging light has its magnetic field aligned with the cylinder axis. Figure A.1 is a sketch of a general cylindrical interface with radius a. The inside/outside refractive index is denoted by $n_{\mathrm{i/o}}$. Also, $H_z^{\mathrm{i/o}}$ is the inside/outside magnetic field, and $E_\theta^{\mathrm{i/o}}$ is θ component of the

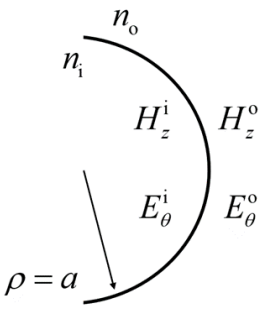

Figure A.1: A sketch of electromagnetic fields at a cylindrical interface.

electric field inside/outside. The magnetic field can be written as $H_z^{\mathrm{i/o}}(\rho,\theta) = \sum_{m=-\infty}^{+\infty} H_z^{m,\mathrm{i/o}}(\rho)\exp(\mathrm{i}m\theta)$, where m takes integer values. Each order can be expressed as a superposition of Bessel and first kind Hankel functions

$$H_z^{m,\mathrm{i/o}}(\rho) = a_m^{\mathrm{i/o}} J_m(k_{\mathrm{i/o}}\rho) + b_m^{\mathrm{i/o}} H_m^{(1)}(k_{\mathrm{i/o}}\rho). \tag{A.1}$$

Because $E_\theta = (1/\mathrm{i}\omega\varepsilon\varepsilon_0)(\partial H_z/\partial\rho)$, so, the corresponding electric field is

$$E_\theta^{m,\mathrm{i/o}}(\rho) = \frac{k}{\mathrm{i}\omega\varepsilon_0}\frac{1}{n_{\mathrm{i/o}}}\left[a_m^{\mathrm{i/o}} J_m'(k_{\mathrm{i/o}}\rho) + b_m^{\mathrm{i/o}} H_m^{(1)'}(k_{\mathrm{i/o}}\rho)\right]. \tag{A.2}$$

By applying the continuity conditions of the electric and magnetic fields at the interface (*i.e.*, $H_z^{m,\mathrm{i}} = H_z^{m,\mathrm{o}}$ and $E_\theta^{m,\mathrm{i}} = E_\theta^{m,\mathrm{o}}$), one gets the scattering matrix as

$$\begin{pmatrix} a_m^{\mathrm{o}} \\ b_m^{\mathrm{o}} \end{pmatrix} = (D^m)^{-1} \cdot \begin{pmatrix} M_{11}^m & M_{12}^m \\ M_{21}^m & M_{22}^m \end{pmatrix} \begin{pmatrix} a_m^{\mathrm{i}} \\ b_m^{\mathrm{i}} \end{pmatrix},$$

where

$$\begin{aligned}
D^m &= n_{\mathrm{i}} J_m'(k_{\mathrm{o}}a) H_{\mathrm{m}}^{(1)}(k_{\mathrm{o}}a) - n_i J_m(k_{\mathrm{o}}a) H_m^{(1)'}(k_{\mathrm{o}}a), \\
M_{11}^m &= n_{\mathrm{o}} J_m'(k_{\mathrm{i}}a) H_m^{(1)}(k_{\mathrm{o}}a) - n_{\mathrm{i}} J_m(k_{\mathrm{i}}a) H_m^{(1)'}(k_{\mathrm{o}}a), \\
M_{12}^m &= n_{\mathrm{o}} H_m^{(1)'}(k_{\mathrm{i}}a) H_m^{(1)}(k_{\mathrm{o}}a) - n_{\mathrm{i}} H_m^{(1)}(k_{\mathrm{i}}a) H_m^{(1)'}(k_{\mathrm{o}}a), \\
M_{21}^m &= n_{\mathrm{i}} J_m(k_{\mathrm{i}}a) J_m'(k_{\mathrm{o}}a) - n_{\mathrm{o}} J_m'(k_{\mathrm{i}}a) J_m(k_{\mathrm{o}}a), \\
M_{22}^m &= n_{\mathrm{i}} H_m^{(1)}(k_{\mathrm{i}}a) J_m'(k_{\mathrm{o}}a) - n_{\mathrm{o}} H_m^{(1)'}(k_{\mathrm{i}}a) J_m(k_{\mathrm{o}}a).
\end{aligned}$$

The prime denotes differentiation with respect to the argument.

A plane wave with unity amplitude in 2D can be written as $\exp(\mathrm{i}\mathbf{k}\cdot\mathbf{r}) = \sum_{m=-\infty}^{+\infty} \mathrm{i}^m J_m(k\rho)\mathrm{e}^{\mathrm{i}m\theta}$. Combining the external source with the scattering matrix, one can finally have the full field distributions in 2D space, as well as the absorption cross-section of the cylinder [113]

$$C_{\mathrm{abs}} = -\frac{2\lambda}{\pi}\sum_m \left[|b_m^{\mathrm{h}}|^2 + \mathrm{Re}\left\{(-\mathrm{i})^m b_m^{\mathrm{h}}\right\}\right], \tag{A.3}$$

where the superscript h of b_m^{h} refers to the host medium.

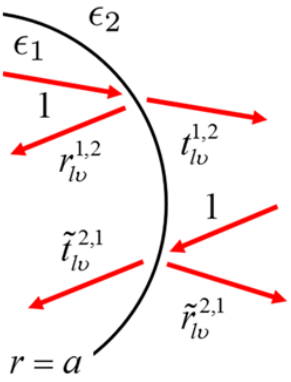

Figure A.2: Mie scattering coefficients at a spherical interface.

A.2 Interaction between multilayer spheres and plane waves

In this section, we present an analytical method to compute electric field distributions of multilayer nanospheres illuminated by external plane waves. The method is used in section 3.1 and 3.2. We extend the Mie theory [148, 149] to rigorously simulate the optical response of multishell nanoparticles. This analytical method allows us to carry out fast calculations in order to search for optimized structures. More precisely, we focus on monochromatic light of frequency ω and consider the spherical waves hosted by each homogeneous spherical layer n in the multishell. We have outgoing spherical waves [201, 202],

$$\mathbf{E}_{lm\mathrm{M}}^{n,\mathrm{o}}(\mathbf{r}) = \mathrm{i}^l \mathbf{L}\, h_l^{(+)}(k_n r) Y_{lm}(\hat{\mathbf{r}}), \tag{A.4}$$

$$\mathbf{E}_{lm\mathrm{E}}^{n,\mathrm{o}}(\mathbf{r}) = -\frac{\mathrm{i}^{l+1}}{k} \nabla \times \mathbf{L}\, h_l^{(+)}(k_n r) Y_{lm}(\hat{\mathbf{r}}), \tag{A.5}$$

and incident spherical waves,

$$\mathbf{E}_{lm\mathrm{M}}^{n,\mathrm{i}}(\mathbf{r}) = \mathrm{i}^l \mathbf{L}\, j_l(k_n r) Y_{lm}(\hat{\mathbf{r}}), \tag{A.6}$$

$$\mathbf{E}_{lm\mathrm{E}}^{n,\mathrm{i}}(\mathbf{r}) = -\frac{\mathrm{i}^{l+1}}{k} \nabla \times \mathbf{L}\, j_l(k_n r) Y_{lm}(\hat{\mathbf{r}}), \tag{A.7}$$

which we label with orbital angular momentum numbers $l = 1, 2, \ldots$ and $m = -l, \cdots, l$, as well as with an index $\nu =$ E and M for transverse electric and magnetic polarization, respectively. Here, $\mathbf{L} = -\mathrm{i}\mathbf{r} \times \nabla$ is the angular momentum operator, $h_l^{(+)} = -y_l + \mathrm{i}j_l$ and j_l are spherical Hankel and Bessel functions [203], Y_{lm} are spherical harmonics, $k_n = (\omega/c)\sqrt{\epsilon_n}$ is the light wave vector in the medium, and ϵ_n is the permittivity. Scattering at a spherical interface ($r = a$) formed between media n (for $r < a$) and $n+1$ (for $r > a$) can be easily described in terms of Mie scattering coefficients $r_{l\nu}^{n,n+1}$, $t_{l\nu}^{n,n+1}$, $\tilde{r}_{l\nu}^{n+1,n}$, and $\tilde{t}_{l\nu}^{n+1,n}$, implicitly defined through the expressions for the electric field produced upon incidence from either the inner or the outer side of the interface (see Figure A.2):

$$\left[\mathbf{E}_{lm\nu}^{n,\mathrm{o}} + r_{l\nu}^{n,n+1}\mathbf{E}_{lm,\nu}^{n,\mathrm{i}}\right]\theta(a-r) = t_{l\nu}^{n,n+1}\mathbf{E}_{lm\nu}^{n+1,\mathrm{o}}\theta(r-a),$$
$$\tilde{t}_{l\nu}^{n+1,n}\mathbf{E}_{lm\nu}^{n,\mathrm{i}}\theta(a-r) = \left[\mathbf{E}_{lm\nu}^{n+1,\mathrm{i}} + \tilde{r}_{l\nu}^{n+1,n}\mathbf{E}_{lm\nu}^{n+1,\mathrm{o}}\right]\theta(r-a).$$

Notice that l, m, and ν are conserved upon reflection or transmission at the interface. Additionally, the scattering coefficients are independent of m. They are obtained from the continuity of the parallel electric and magnetic field components at the interface. Their detailed expressions for the $r = a$ interface separating generic media 1 (within $r < a$) and 2 (within $r > a$) are as follows:

$$\begin{aligned}
r_{l\mathrm{M}}^{12} &= A\ \left\{\rho_2 h_l^{(+)}(\rho_1)[h_l^{(+)}(\rho_2)]' - \rho_1 h_l^{(+)}(\rho_2)[h_l^{(+)}(\rho_1)]'\right\}\\
t_{l\mathrm{M}}^{12} &= A\,\rho_1\ \left\{h_l^{(+)}(\rho_1)j_l'(\rho_1) - j_l(\rho_1)[h_l^{(+)}(\rho_1)]'\right\}\\
r_{l\mathrm{E}}^{12} &= B\ \left\{\epsilon_1 h_l^{(+)}(\rho_1)[\rho_2 h_l^{(+)}(\rho_2)]' - \epsilon_2 h_l^{(+)}(\rho_2)[\rho_1 h_l^{(+)}(\rho_1)]'\right\}\\
t_{l\mathrm{E}}^{12} &= B\,\epsilon_1\rho_1\ \left\{h_l^{(+)}(\rho_1)j_l'(\rho_1) - j_l(\rho_1)[h_l^{(+)}(\rho_1)]'\right\}\\
\tilde{r}_{l\mathrm{M}}^{21} &= A\ \left\{\rho_2 j_l(\rho_1)j_l'(\rho_2) - \rho_1 j_l(\rho_2)j_l'(\rho_1)\right\}\\
\tilde{t}_{l\mathrm{M}}^{21} &= A\,\rho_2\ \left\{h_l^{(+)}(\rho_2)j_l'(\rho_2) - j_l(\rho_2)[h_l^{(+)}(\rho_2)]'\right\}\\
\tilde{r}_{l\mathrm{E}}^{21} &= B\ \left\{\epsilon_1 j_l(\rho_1)[\rho_2 j_l(\rho_2)]' - \epsilon_2 j_l(\rho_2)[\rho_1 j_l(\rho_1)]'\right\}\\
\tilde{t}_{l\mathrm{E}}^{21} &= B\,\epsilon_2\rho_2\ \left\{h_l^{(+)}(\rho_2)j_l'(\rho_2) - j_l(\rho_2)[h_l^{(+)}(\rho_2)]'\right\}
\end{aligned}$$

where

$$A = \left[\rho_1 h_l^{(+)}(\rho_2) j_l'(\rho_1) - \rho_2 j_l(\rho_1)[h_l^{(+)}(\rho_2)]'\right]^{-1},$$
$$B = \left[\epsilon_2 h_l^{(+)}(\rho_2)[\rho_1 j_l(\rho_1)]' - \epsilon_1 j_l(\rho_1)[\rho_2 h_l^{(+)}(\rho_2)]'\right]^{-1},$$

$\rho_1 = (\omega a/c)\sqrt{\epsilon_1}$, $\rho_2 = (\omega a/c)\sqrt{\epsilon_2}$, and the prime denotes differentiation with respect to ρ_1 and ρ_2.

The electric field within each layer n is then expanded as a sum over the above spherical waves. We use the convention $\mathbf{E}(\mathbf{r},t) = \mathbf{E}(\mathbf{r})\mathrm{e}^{-\mathrm{i}\omega t} + \mathbf{E}^*(\mathbf{r})\mathrm{e}^{\mathrm{i}\omega t}$, with the field amplitude written as

$$\mathbf{E}(\mathbf{r}) = \sum_{lm\nu} \left[a_{lm\nu}^n \mathbf{E}_{lm\nu}^{n,\mathrm{o}}(\mathbf{r}) + b_{lm\nu}^n \mathbf{E}_{lm\nu}^{n,\mathrm{i}}(\mathbf{r})\right].$$

We obtain the expansion coefficients $a_{lm\nu}^n$ and $b_{lm\nu}^n$ by solving the linear set of equations

$$b_{lm\nu}^n = r_{l\nu}^{n,n+1} a_{lm\nu}^n + \tilde{t}_{l\nu}^{n+1,n} b_{lm\nu}^{n+1},$$
$$a_{lm\nu}^{n+1} = t_{l\nu}^{n,n+1} a_{lm\nu}^n + \tilde{r}_{l\nu}^{n+1,n} b_{lm\nu}^{n+1},$$

resulting from expressing the components leaving the $n/(n+1)$ interface in terms of the scattering of the waves coming into it. The source is provided by the external illumination in the surrounding medium, for which we consider an incident plane wave, whose spherical-wave decomposition is as follows [202].

We consider the electric field of the incident wave is written as [149]

$$\mathbf{E}^{\mathrm{ext}} = \vec{\epsilon}\mathrm{e}^{\mathrm{i}\mathbf{K}\cdot\mathbf{r}}, \tag{A.8}$$

where $\vec{\epsilon}$ is the polarization vector with $|\vec{\epsilon}| = 1$, and $\mathbf{K}$ is the momentum of the impinging light with $|\mathbf{K}_i| = (\omega/c)\sqrt{\varepsilon_h \mu_h}$, where the subscript h refers to the host medium. The multipole coefficients of the spherical waves decomposed from the

plane wave are [201]

$$b_{lmM} = \left[4\pi \mathrm{e}^{\mathrm{i}\mathbf{K}\cdot\mathbf{r}}/l/(l+1)\right] \cdot \vec{\zeta}^{*}_{lm}(\Omega) \cdot \vec{\epsilon},$$
$$b_{lmM} = \left[4\pi \mathrm{e}^{\mathrm{i}\mathbf{K}\cdot\mathbf{r}}/l/(l+1)\right] \cdot \vec{\zeta}^{*}_{lm}(\Omega) \cdot (\vec{\epsilon} \times \mathbf{K})/(k\varepsilon_0\mu_0),$$

where Ω denotes the polar angle of $\mathbf{K}$,

$$\begin{aligned}\vec{\zeta}_{lm}(\Omega) &= \mathbf{L}Y_{lm}(\Omega) \\ &= \left[C_+ Y_{lm+1}(\Omega)/2 + C_- Y_{lm-1}(\Omega)/2, -\mathrm{i}C_+ Y_{lm+1}(\Omega)/2 + \mathrm{i}C_- Y_{lm-1}(\Omega)/2, mY_{lm}(\Omega)\right],\end{aligned}$$

and $C_\pm = \sqrt{(l \pm m + 1)(l \mp m)}$. Note that the plane wave is only the superposition of different orders of spherical waves generated by the sperical Bessel function j_l.

Appendix B

Interaction between multilayer spheres and point electric dipoles

In this section, we describe a method to compute the interaction between a multilayer nanosphere and a point electric dipole located in the core, which is used in section 3.1. Figure B.1 is a schematic view of the considered configuration. The dipole is located at any position in the core with any orientation. The first step is to use the multipole sperical waves to express the dipole fields in terms of them. Through some algebra, we can find the expressions of three mutual-orthogonal unit dipoles,

$$\begin{aligned}
\mathbf{E}^{\hat{z}}_{\mathrm{dip}}(\mathbf{r}) &= -\mathrm{i}k^3\sqrt{\frac{4\pi}{3}}\mathbf{E}^{h}_{1,0,\mathrm{E}}(\mathbf{r}),\\
\mathbf{E}^{\hat{x}}_{\mathrm{dip}}(\mathbf{r}) &= -\mathrm{i}k^3\sqrt{\frac{4\pi}{3}}\frac{1}{\sqrt{2}}\left[\mathbf{E}^{h}_{1,-1,\mathrm{E}}(\mathbf{r}) - \mathbf{E}^{h}_{1,1,\mathrm{E}}(\mathbf{r})\right],\\
\mathbf{E}^{\hat{y}}_{\mathrm{dip}}(\mathbf{r}) &= -\mathrm{i}k^3\sqrt{\frac{4\pi}{3}}\frac{1}{\sqrt{2}}\left[\mathbf{E}^{h}_{1,-1,\mathrm{E}}(\mathbf{r}) + \mathbf{E}^{h}_{1,1,\mathrm{E}}(\mathbf{r})\right],
\end{aligned}$$

where the superscripts of the left sides $\hat{i}$ $(i = x, y, z)$ denote unit dipoles along x, y, z directions. The sperical waves have been defined in Eq. (A.5). In this section, the superscripts o and i are replaced by h and j, respectively, to explicitly show that they are generated by spherical Hankel or spherical Bessel functions.

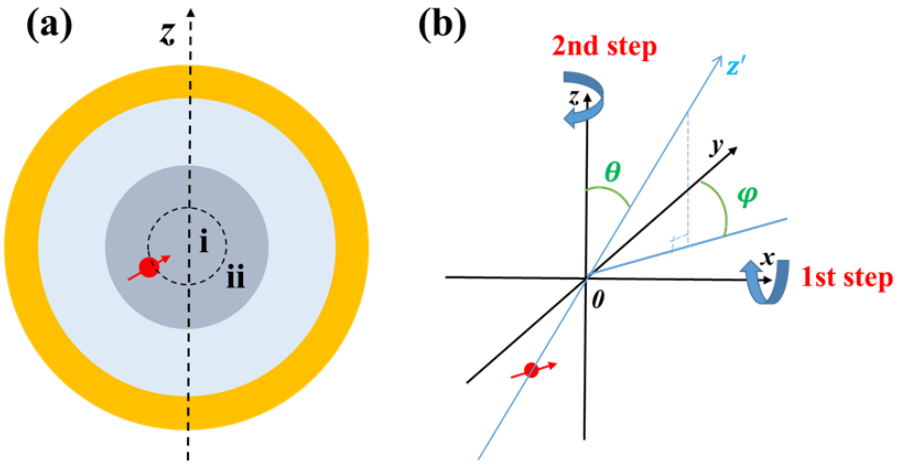

Figure B.1: (a) An electric dipole located in the dielectric core coated by an additional dielectric layer and a metal shell. (b) Transformation from the lab coordinates to the dipole coordinates.

The centers of the above harmonics are located at the dipole positions. So, the second step is to decompose them into sums of a series of sperical waves, whose centers should be at the origin of the coordinate. We follow methods similar to those of Ref. [202]. For simplicity, we will assume the dipoles are located at the negative part of the z axis.

For $\mathbf{E}^h_{1,\pm1,\mathrm{E}}(\mathbf{r})$, in region i, we have $\mathbf{E}^h_{1,\pm1,\mathrm{E}}(\mathbf{r}) = \sum_{l'} \left[\varphi^j_{l',\pm1,\mathrm{E}}\mathbf{E}^j_{l',\pm1,\mathrm{E}}(\mathbf{r}) + \varphi^j_{l',\pm1,\mathrm{M}}\mathbf{E}^j_{l',\pm1,\mathrm{M}}(\mathbf{r})\right]$, where $\varphi^j_{l'm,\mathrm{E/M}} = \sum_l T^{\mathrm{E/M,E}}_{l'mlm} G^{hj}_{1mlm}$. l' takes integers counting from 1 to a maximum value $l'_{\max}$. Also, l takes values of l' and $l' \pm 1$ (all other values lead to trivial results, see the expressions for T below). The Green function can be written as [204]

$$G^{hj}_{l'mlm} = \sqrt{4\pi} \sum_{l''=|l-l'|}^{l'+l} \mathrm{i}^{l''} \sqrt{2l''+1} h^{(+)}_{l''}(k_i d) < l'm|l''0|lm >, \tag{B.1}$$

where $< l'm'|l''m''|lm >= \int d\Omega Y^*_{l'm'}(\Omega) Y_{l''m''}(\omega) Y_{lm}(\Omega)$ is the so-called Gaunt integral.

The translation operator is written as

$$T^{\mathrm{EE}}_{l',m,l,m} = \delta_{ll'} + kdp_{ll'm},$$
$$T^{\mathrm{ME}}_{l',m,l,m} = kdq_{ll'm}\sqrt{\varepsilon_i},$$

where $p_{ll'm} = \delta_{l+1,l'} D_{l+1,m} - \delta_{l-1,l'} D_{lm}$, $D_{lm} = (\mathrm{i}/l)\sqrt{(l^2-m^2)/(4l^2-1)}$, and $q_{ll'm} = m\delta_{ll'}/l/(l+1)$.

In region ii, the field is decomposed as a series of spherical waves generated by sperical Hankel functions. $\mathbf{E}^h_{1,\pm1,\mathrm{E}}(\mathbf{r}) = \sum_{l'} \left[\varphi^h_{l',\pm1,\mathrm{E}} \mathbf{E}^h_{l',\pm1,\mathrm{E}}(\mathbf{r}) + \varphi^h_{l',\pm1,\mathrm{M}} \mathbf{E}^h_{l',\pm1,\mathrm{M}}(\mathbf{r})\right]$, where $\varphi^h_{l'm,\mathrm{E/M}} = \sum_l T^{\mathrm{E/M,E}}_{l'mlm} G^{hh}_{1mlm}$, and

$$G^{hh}_{l'mlm} = \sqrt{4\pi} \sum_{l''=|l-l'|}^{l'+l} \mathrm{i}^{l''} \sqrt{2l''+1} j_{l''}(k_i d) < l'm|l''0|lm > . \tag{B.2}$$

For $\mathbf{E}^h_{1,0,\mathrm{E}}(\mathbf{r})$, in region i, $\mathbf{E}^h_{1,0,\mathrm{E}}(\mathbf{r}) = \sum_{l'} \varphi^j_{l'0\mathrm{E}} \mathbf{E}^j_{l',0,\mathrm{E}}(\mathbf{r})$. In region ii, $\mathbf{E}^h_{1,0,\mathrm{E}}(\mathbf{r}) = \sum_{l'} \varphi^h_{l'0\mathrm{E}} \mathbf{E}^h_{l',0,\mathrm{E}}(\mathbf{r})$.

After knowing the sperical waves, whose centers are at the origin, as sources plus their scattering coefficients at the multiple spherical interfaces as presented in section A.2, we can obtain the induced field $\mathbf{E}_{\mathrm{ind}}$. Then, we know coupling strength between the electric dipole and the electromagnetic modes acting on it through calculating the total decay rate [21, 205]

$$\Gamma = \Gamma_0 + \frac{2}{\hbar} \mathrm{Im}\left\{\mathbf{d}^* \cdot \mathbf{E}_{\mathrm{ind}}\right\}, \tag{B.3}$$

where d is the transition dipole matrix element, $\Gamma_0 = 4k^3|\mathbf{d}|^2/3/\hbar$ is the decay rate in free space. The normalized LDOS presented in section 3.1 is equal to Γ/Γ_0. The radiative part of the total decay rate $\Gamma_{\mathrm{emission}}$ can be computed by intergrating the Poynting vector at a surface enclosing the whole structure. Also, the normalized $\mathrm{LDOS}_{\mathrm{rad}}$ is equal to $\Gamma_{\mathrm{emission}}/\Gamma_0$. When the dipole is oriented along the z axis, we have

$$\mathrm{LDOS}_{\mathrm{rad}} = \frac{1}{2} \sum_l l(l+1) |a^{\mathrm{h}}_{l,0,\mathrm{E}}|^2 \sqrt{\varepsilon_{\mathrm{h}}}. \tag{B.4}$$

When the dipole is along the x or y directions, we find

$$\mathrm{LDOS}_{\mathrm{rad}} = \frac{1}{4} \sum_l l(l+1) \left[|a^{\mathrm{h}}_{l,\pm1,\mathrm{E}}|^2 \sqrt{\varepsilon_{\mathrm{h}}} + |a^{\mathrm{h}}_{l,\pm1,\mathrm{M}}|^2 / \sqrt{\varepsilon_{\mathrm{h}}}\right], \tag{B.5}$$

where ε_{h} is relative permittivity of the host media.

For an electric dipole with any orientation (*e.g.*, it is along the $z\prime$ axis in Fig. B.1(b)), we just need to firstly project it onto axies as $p_x = p \cdot \sin\theta \cdot \sin\varphi$, $p_y = p \cdot \sin\theta \cdot \cos\varphi$, and $p_z = p \cdot \cos\theta$. Then, we calculate the induced fields of each of these components, respectively, and sum them up at last.

So far, we always consider the dipole to be located in the negative part of z axis. For a dipole with any position in 3D space, we just need to rotate the lab coordinates to make the dipole sit on the z axis of the new coordinates, which are named dipole coordinates (see Fig. B.1(b)). Then, we do all the computations in the dipole coordinates. Finally, we transform the values of the electric fields back to the lab coordinates. Specifically, as shown by Fig. B.1(b), the rotation consists of two steps. First, we rotate around the x axis by θ. Second, we rotate around the z axis by φ. These rotations can be described by two 3×3 matrices $\mathbf{R}_x$ and $\mathbf{R}_z$, respectively. So, the relation between dipole moment $\mathbf{p}'$ in the dipole coordinates and dipole moment $\mathbf{p}$ in the lab coordiantes is expressed as $\mathbf{p}' = \mathbf{R}_z\mathbf{R}_x\mathbf{p}$. The relation between electric fields in the two coordinates is $\mathbf{E} = (\mathbf{R}_z\mathbf{R}_x)^{-1}\mathbf{E}'$. The expressions of the two matrices are as follows:

$$\mathbf{R}_x = \begin{pmatrix} 1 & 0 & 0 \\ 0 & \cos\theta & -\sin\theta \\ 0 & \sin\theta & \cos\theta \end{pmatrix},$$

$$\mathbf{R}_z = \begin{pmatrix} \cos\varphi & -\cos\theta\sin\varphi & -\sin\theta\sin\varphi \\ \cos\theta\sin\varphi & \cos\varphi + \sin^2\theta(1-\cos\varphi) & -\sin\theta\cos\theta(1-\cos\varphi) \\ \sin\theta\sin\varphi & -\sin\theta\cos\theta(1-\cos\varphi) & \cos\varphi + \cos^2\theta(1-\cos\varphi) \end{pmatrix}.$$

Appendix C

Heat transfer simulations in multishell spheres

In this section, we present the detailed heat transfer simulation methods used in section 3.2. We evaluate the photothermal response of multishell nanostructures immersed in water similar to the one depicted in Fig. 3.2(a) by adopting the two-temperature model and incorporating temperature-dependent TBCs. We focus on either gold or aluminum metal intercalated with silica layers. Under cw illumination conditions, light energy is absorbed by the electrons in the metallic shells and then partially transferred from those electrons to the atomic lattice (*i.e.*, phonons) of both the metal and the adjacent dielectric layers. Additionally, phonons of the metal and dielectric regions exchange energy until a steady-state thermal distribution is established. The parameters that control these processes are illustrated in Fig. C.1(a) for a generic metallic shell j flanked by two dielectric layers. They are as follows:

- *Geometrical parameters.* Each metal layer j has inner and outer radii $R_{j,\mathrm{i}}$ and $R_{j,\mathrm{o}}$, while the corresponding metal/dielectric interfaces have areas $S_{j,\mathrm{i/o}} = 4\pi R_{j,\mathrm{i/o}}^2$ and the metal layer volume is $V_j = (4\pi/3)\left(R_{j,\mathrm{o}}^3 - R_{j,\mathrm{i}}^3\right)$.

- *Temperatures.* We consider the electron and lattice temperatures, T_j^{e} and T_j^{l}, as well as the temperatures at the dielectrics right outside the inner and outer interfaces with the metal, $T_{j,\mathrm{i}}^{\mathrm{d}}$ and $T_{j,\mathrm{o}}^{\mathrm{d}}$, respectively. The temperatures are

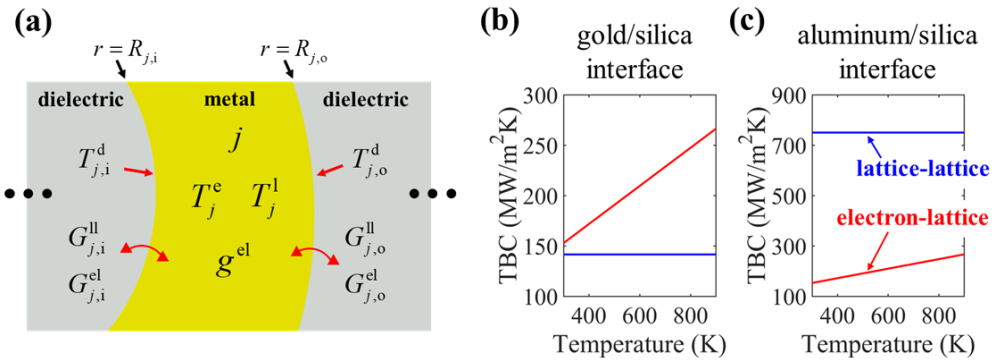

Figure C.1: (a) Parameters used for the modeling of the thermal response of multishells. We show one of the metal layers (j), along with its corresponding radii, temperatures, and TBCs. (b, c) Temperature-dependence of the TBCs in gold-silica (b) and aluminum-silica (c) interfaces. The temperature is taken as that of the metal conduction electrons.

assumed to be uniform within each metal layer because of its high thermal conductivity. In contrast, the temperature varies with radial distance in each dielectric layer (see below).

- *Thermal boundary conductances.* When a temperature difference exists between both sides of an interface, heat flows through it with a power per unit area that is proportional to that difference. The coefficient of proportionality is the TBC, also known as Kapitza conductance [141, 142, 143, 144]. Two different channels of conductance are known to exist at metal/dielectric interfaces[206]: metal electrons coupling to the dielectric lattice (el); and metal lattice coupling to the dielectric lattice (ll). We denote the corresponding TBCs as $G^{el}_{j,i/o}$ and $G^{ll}_{j,i/o}$, respectively, where the i and o subscripts refer to the inner and outer metal/dielectric interfaces. The $G^{ll}_{j,i/o}$ conductances for the lattice-lattice channel are obtained by relying on the commonly used diffuse mismatch model [160, 207], which results in a temperature-independent value $G^{ll}_{j,i/o} = 141.5\,\mathrm{MW\,m^{-2}\,K^{-1}}$ ($750\,\mathrm{MW\,m^{-2}\,K^{-1}}$) for interfaces formed between gold (aluminum) and silica [206]. The lattice-lattice channel is usually regarded to be dominant over the electron-lattice one [208]. Additionally, the TBCs are sensitive to the synthesis procedure [209, 210], so that several previous works consider a temperature-independent total TBC as a simplifying

assumption [160, 207, 209, 210, 211, 212, 213]. Only a few experimental works isolate the effect of the electron-lattice channel [214, 215, 216], which combined with additional theoretical works [206, 217], show that it plays an important role in metal/dielectric systems such as the ones here considered. We thus use an experimentally fitted function for the electron-lattice conductance of the interface between silica and gold [206, 215]:

$$G^{\mathrm{el}}_{j,\mathrm{i/o}} = \left(96.12 + 0.189\, T^{\mathrm{e}}_j\right)\ \mathrm{MW\,m^{-2}\,K^{-1}} \tag{C.1}$$

(see Fig. C.1(b,c)). Due to the scarcity of data for aluminum, we use the same expression for this material, which should provide a qualitative level of description. Finally, considering a total of N metal layers, we assume the outermost of them ($j = N$) to be metallic and in contact with the surrounding water environment. The corresponding TBC between the metal and water is assumed to have a temperature-independent value $G^{\mathrm{ll}}_{N,\mathrm{o}} = 105\,\mathrm{MW\,m^{-2}\,K^{-1}}$ ($753\,\mathrm{MW\,m^{-2}\,K^{-1}}$) for gold[153] (aluminum[218]).

- *Electron-lattice coupling inside the metal.* We assume an electron-lattice coupling at the bulk of the metal proportional to the difference between electron and lattice temperatures, resulting in a power-density transfer $g^{\mathrm{el}}(T^{\mathrm{e}}_j - T^{\mathrm{l}}_j)$, with $g^{\mathrm{el}} = 3\times10^{16}\,\mathrm{W\,m^{-3}\,K^{-1}}$ ($3\times10^{17}\,\mathrm{W\,m^{-3}\,K^{-1}}$) for gold (aluminum).[150]

- *Bulk thermal conductivity.* We take the conductivities of silica and water as $\kappa_{\mathrm{silica}} = 1.0\,\mathrm{W\,m^{-1}\,K^{-1}}$ and $\kappa_{\mathrm{water}} = 0.6\,\mathrm{W\,m^{-1}\,K^{-1}}$. The metal conductivity is orders of magnitude larger (*e.g.*, $\kappa_{\mathrm{gold}} = 318\,\mathrm{W\,m^{-1}\,K^{-1}}$), so we assume a uniform temperature inside each homogeneous metal region.

With these parameters, we now write a self-consistent set of equations that express the condition of steady-state temperature distribution. First of all, the optical power P_j absorbed by electrons in the metal layer j,

$$P_j = g^{\mathrm{el}} V_j (T^{\mathrm{e}}_j - T^{\mathrm{l}}_j) + G^{\mathrm{el}}_{j,\mathrm{i}} S_{j,\mathrm{i}} (T^{\mathrm{e}}_j - T^{\mathrm{d}}_{j,\mathrm{i}}) + G^{\mathrm{el}}_{j,\mathrm{o}} S_{j,\mathrm{o}} (T^{\mathrm{e}}_j - T^{\mathrm{d}}_{j,\mathrm{o}}), \tag{C.2}$$

must be equal to the rate of heat transferred from the metal electrons to the lattices of both the metal (first term in the right-hand side of Eq (C.2) and the adjacent

dielectrics (rightmost two terms). The energy deposited by the electrons into the lattice of layer j,

$$g^{\mathrm{el}}V_j(T_j^{\mathrm{e}} - T_j^{\mathrm{l}}) = G_{j,\mathrm{i}}^{\mathrm{ll}}S_{j,\mathrm{i}}(T_j^{\mathrm{l}} - T_{j,\mathrm{i}}^{\mathrm{d}}) + G_{j,\mathrm{o}}^{\mathrm{ll}}S_{j,\mathrm{o}}(T_j^{\mathrm{l}} - T_{j,\mathrm{o}}^{\mathrm{d}}), \tag{C.3}$$

is now exchanged with the adjacent dielectrics through the lattice-lattice TBC channel (right-hand side of eq (C.3)). A similar balance applies to each dielectric layer, leading to

$$\begin{aligned} &S_{j,\mathrm{o}}\left[G_{j,\mathrm{o}}^{\mathrm{el}}(T_j^{\mathrm{e}} - T_{j,\mathrm{o}}^{\mathrm{d}}) + G_{j,\mathrm{o}}^{\mathrm{ll}}(T_j^{\mathrm{l}} - T_{j,\mathrm{o}}^{\mathrm{d}})\right] \\ &= -S_{j+1,\mathrm{i}}\left[G_{j+1,\mathrm{i}}^{\mathrm{el}}(T_{j+1}^{\mathrm{e}} - T_{j+1,\mathrm{i}}^{\mathrm{d}}) + G_{j+1,\mathrm{i}}^{\mathrm{ll}}(T_{j+1}^{\mathrm{l}} - T_{j+1,\mathrm{i}}^{\mathrm{d}})\right], \end{aligned} \tag{C.4}$$

where each side of the equation describes the power transferred from each of the two dielectric-metal interfaces. The condition of flux conservation across each dielectric layer leads to yet another set of equations: under stationary conditions the temperature obeys the Poisson equation [219], and thus, its radial dependence within a homogeneous dielectric layer has the form $A + B/r$, resulting in a diffused heat power $4\pi B\kappa_{\mathrm{silica}}$; the coefficients A and B are directly related to the temperatures at the dielectric interfaces (*i.e.*, at the radial distances $R_{j,\mathrm{o}}$ and $R_{j+1,\mathrm{i}}$ for the dielectric layer sandwiched in between metal layers j and $j+1$; see Fig. C.1(a)), whereas heat dissipation has to account for all of the light absorption in the metal layers surrounded by the dielectric shell under consideration ($\sum_{j'=1}^{j} P_{j'}$); we find

$$\sum_{j'=1}^{j} P_{j'} = \frac{4\pi\kappa_{\mathrm{silica}}R_{j+1,\mathrm{i}}R_{j,\mathrm{o}}}{R_{j+1,\mathrm{i}} - R_{j,\mathrm{o}}}(T_{j,\mathrm{o}}^{\mathrm{d}} - T_{j+1,\mathrm{i}}^{\mathrm{d}}). \tag{C.5}$$

In the work presented in chapter 3.2, we consider multishells formed by $N = 1 - 3$ metal layers, with a dielectric core and with an outermost metal layer directly in contact with the surrounding water medium. We then have to find the $4N$ temperatures T_j^{e}, T_j^{l}, $T_{j,\mathrm{i}}^{\mathrm{d}}$, and $T_{j,\mathrm{o}}^{\mathrm{d}}$ associated with each metal layer $j = 1, \ldots, N$ and its surrounding dielectrics. These are the unknowns in the above equations. The number of equations are N in each set of Eqs (C.2) and (C.3) (one per metal layer) and $N-1$ in each set of Eqs (C.4) and (C.5) (one per dielectric layer flanked by two metal layers), resulting in a total of $4N-2$ equations. The remaining two equations

are provided by (i) heat balance of the entire particle, which determines the water temperature $T^{\mathrm{d}}_{N,\mathrm{o}}$ right at the interface with the multishell according to [219]

$$\sum_{j=1}^{N} P_j = 4\pi\kappa_{\mathrm{water}} R_{N,\mathrm{o}} (T^{\mathrm{d}}_{N,\mathrm{o}} - T_0), \tag{C.6}$$

where $T_0 = 300\,\mathrm{K}$ is the temperature of the environment; and (ii) the specialization of Eq (C.4) to the dielectric core,

$$G^{\mathrm{el}}_{1,\mathrm{i}}(T^{\mathrm{e}}_1 - T^{\mathrm{d}}_{1,\mathrm{i}}) + G^{\mathrm{ll}}_{1,\mathrm{i}}(T^{\mathrm{l}}_1 - T^{\mathrm{d}}_{1,\mathrm{i}}) = 0. \tag{C.7}$$

Equations (C.2)-(C.7) thus form a nonlinear set of equations (notice the temperature dependence of $G^{\mathrm{el}}_{j,\mathrm{i/o}}$ through Eq (C.1) that we solve using the Newton-Raphson iteration method.

Appendix D

Quantum-mechanical description of four-level atoms

We discuss, in this appendix, the general method to describe the interaction between 4-level optical emitters and pump/probe light waves. Also, we present the detailed derivations of the motion equations of their polarization and population densities, which are frequently used in many publications about the gain media as mentioned in section 1.5.

The 4-level optical emitters (labeled by l) are coupled to a bath of photons (boson modes labeled by n). The temporal dynamics of this system can be generally

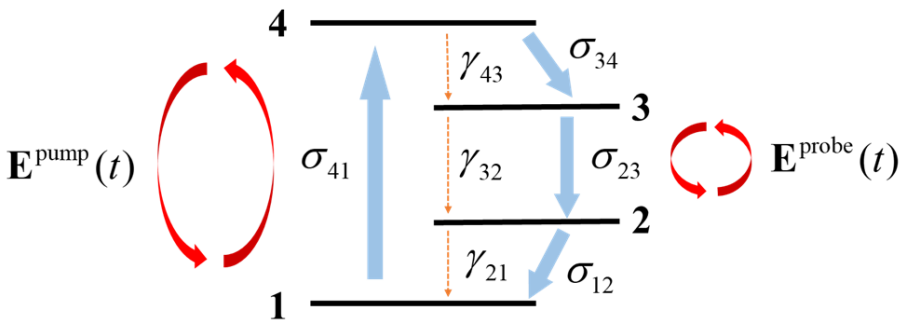

Figure D.1: Sketch of a 4-level system interacting with pump and probe light.

described through the time-dependent Hamiltonian

$$\mathcal{H} = \hbar \sum_{li} \varepsilon_i |li\rangle\langle li| + \hbar \sum_n \omega_n a_n^\dagger a_n + \sum_{nlii'} \left(g^*_{nlii'} a_n^\dagger + g_{nlii'} a_n \right) \left(\sigma^\dagger_{lii'} + \sigma_{lii'} \right) - \sum_{lii'} \mathbf{d}_{ii'} \cdot \mathbf{E}_l^{\text{ext}}(t) \left(\sigma^\dagger_{lii'} + \sigma_{lii'} \right), \tag{D.1}$$

where the index $i = 1 - 4$ runs over the emitter levels of energies $\hbar\varepsilon_i$; the operators $\sigma_{lii'} = |li\rangle\langle li'|$ describe $i' \to i$ atomic transitions of the emitter l at the position $\mathbf{r}_l$; the operators $a_n^\dagger$ and a_n account for the creation and annihilation of photons with energy $\hbar\omega_n$; the complex coupling coefficients $g_{nlii'}$ connect photons in mode n and the levels i and i' in emitter l; the compex vectors $\mathbf{d}_{ii'}$ are the corresponding emitter dipole moments; and $\mathbf{E}_l^{\text{ext}}(t) = \mathbf{E}^{\text{pump}}(\mathbf{r}_l)\mathrm{e}^{-\mathrm{i}\omega' t} + \mathbf{E}^{\text{probe}}(\mathbf{r}_l)\mathrm{e}^{-\mathrm{i}\omega t} + \text{c.c.}$ is the time-dependent external field at the position $\mathbf{r}_l$ given by the superposition of pump and probe fields with amplitudes $\mathbf{E}^{\text{pump}}(\mathbf{r}_l)$ and $\mathbf{E}^{\text{probe}}(\mathbf{r}_l)$, oscillating with frequencies ω' and ω, respectively. Incidentally, $\sigma^\dagger_{lii'} = \sigma_{li'i}$, so in the double sums over ii' throughout this document we only consider terms $i > i'$ in order to avoid counting these transitions twice. The temporal evolution of the total density matrix $\rho(t)$ is governed by the equation of motion

$$\dot{\rho} = -\frac{\mathrm{i}}{\hbar}[\mathcal{H}(t), \rho] + \mathcal{L}[\rho], \tag{D.2}$$

in which the commutator $[\mathcal{H}(t), \rho]$ describes the coherent temporal evolution of the system, complemented by nonradiative incoherent transitions introduced through the Lindblad operator

$$\mathcal{L}[\rho] = \sum_{lii'} \frac{\gamma_{ii'}}{2} \left(2\sigma_{lii'} \rho \sigma^\dagger_{lii'} - \sigma^\dagger_{lii'} \sigma_{lii'} \rho - \rho \sigma^\dagger_{lii'} \sigma_{lii'} \right) + \sum_n \frac{\Gamma_n}{2} \left(2a_n \rho a_n^\dagger - a_n^\dagger a_n \rho - \rho a_n^\dagger a_n \right), \tag{D.3}$$

with inelastic rates $\gamma_{ii'}$ for the atoms (see sketch in Fig. D.1) and Γ_n for the photon mode n.

At this point, we approximate the density matrix by the tensor product $\rho = \rho^{\text{rad}} \otimes \rho^{\text{at}}$, where $\rho^{\text{at}} = \Pi_l \rho_l^{\text{at}}$, $\rho^{\text{rad}} = \Pi_n |\alpha_n\rangle\langle\alpha_n|$, and we assume each photon state n to be in a coherent state $|\alpha_n\rangle$ with amplitude $\alpha_n = \text{Tr}\{a_n \rho\}$. Using $\left[a_n, a_{n'}^\dagger\right] = \delta_{nn'}$,

along with the property $a_n|\alpha_n\rangle = \alpha_n|\alpha_n\rangle$ of coherent states (leading to $a_n\rho = \alpha_n\rho$ and $\rho a_n^\dagger = \alpha_n^*\rho$), we find from Eq. (D.2) that the coherent-state amplitude satisfies the equation [189, 220, 221]

$$\dot{\alpha}_n = \frac{d}{dt}\mathrm{Tr}\left\{a_n\rho\right\} = \mathrm{Tr}\left\{a_n\dot{\rho}\right\} = -\mathrm{i}\left(\omega_n - \mathrm{i}\frac{\Gamma_n}{2}\right)\alpha_n - \frac{\mathrm{i}}{\hbar}\sum_{lii'} g^*_{nlii'}\mathrm{Tr}\left\{(\sigma^\dagger_{lii'} + \sigma_{lii'})\rho^{\mathrm{at}}\right\}. \tag{D.4}$$

Having assumed coherent states for the photons, the Hamiltonian of the system reduces to

$$\mathcal{H} = \hbar\sum_n \omega_n|\alpha_n|^2 + \sum_l \mathcal{H}_l, \tag{D.5}$$

where

$$\mathcal{H}_l = \hbar\sum_i \varepsilon_i|li\rangle\langle li| + \sum_{ii'}\left(g^*_{lii'} + g_{lii'}\right)\left(\sigma^\dagger_{lii'} + \sigma_{ii'}\right) - \sum_{lii'}\mathbf{d}_{ii'}\cdot\mathbf{E}^{\mathrm{ext}}_l(t)\left(\sigma^\dagger_{lii'} + \sigma_{lii'}\right), \tag{D.6}$$

and we introduce the new coupling parameters

$$g_{lii'} = \sum_n g_{nlii'}\alpha_n. \tag{D.7}$$

We assume that every emitter can be described as the 4-level system sketched in Fig. D.1. Then, the equation of motion of a single emitter is explicitly given by

$$\begin{aligned}\dot{\rho}_l = &-\frac{\mathrm{i}}{\hbar}[\mathcal{H}_l, \rho_l] \\ &+ \frac{\gamma_{21}}{2}\left(2\sigma_{l12}\rho_l\sigma^\dagger_{l12} - \sigma^\dagger_{l12}\sigma_{l12}\rho_l - \rho_l\sigma^\dagger_{l12}\sigma_{l12}\right) \\ &+ \frac{\gamma_{43}}{2}\left(2\sigma_{l34}\rho_l\sigma^\dagger_{l34} - \sigma^\dagger_{l34}\sigma_{l34}\rho_l - \rho_l\sigma^\dagger_{l34}\sigma_{l34}\right) \\ &+ \frac{\gamma_{32}}{2}\left(2\sigma_{l23}\rho_l\sigma^\dagger_{l23} - \sigma^\dagger_{l23}\sigma_{l23}\rho_l - \rho_l\sigma^\dagger_{l23}\sigma_{l23}\right),\end{aligned} \tag{D.8}$$

where we drop the at superscript from ρ_l^{at} for convenience. In what follows, we also omit the index l, which is implicitly understood in the following expressions. Note that we assume the damping rates γ_{21}, γ_{32}, and γ_{43}, the energy levels $\hbar\varepsilon_i$, and

the transition dipoles $\mathbf{d}_{14}$ and $\mathbf{d}_{23}$ to be the same for all emitters (i.e., independent of l). Damping rates and transition dipoles other than these ones are disregarded. Additionally, radiative damping from level 4 and level 2 is ignored, so g_{23} is the only nonzero radiative coupling coefficient. Now, we express the density matrix in the state representation $\rho = \sum_{ii'} \rho_{ii'} |i\rangle\langle i'|$, from which the property $\rho^\dagger = \rho$ is found to lead to the condition $\rho_{ii'} = \rho^*_{i'i}$, so we only need to work out the elements with $i \leq i'$. Explicitly, the density-matrix equations of motion read

$$\dot{\rho}_{11} = \frac{\mathrm{i}}{\hbar}\mathbf{d}_{14} \cdot \mathbf{E}^{\mathrm{pump}}(t)\,(\rho_{41} - \rho_{14}) + \gamma_{21}\rho_{22}, \tag{D.9a}$$

$$\dot{\rho}_{22} = \frac{\mathrm{i}}{\hbar}\left[\mathbf{d}_{23} \cdot \mathbf{E}^{\mathrm{probe}}(t) - (g^*_{23} + g_{23})\right](\rho_{32} - \rho_{23}) - \gamma_{21}\rho_{22} + \gamma_{32}\rho_{33}, \tag{D.9b}$$

$$\dot{\rho}_{33} = -\frac{\mathrm{i}}{\hbar}\left[\mathbf{d}_{23} \cdot \mathbf{E}^{\mathrm{probe}}(t) - (g^*_{23} + g_{23})\right](\rho_{32} - \rho_{23}) + \gamma_{43}\rho_{44} - \gamma_{32}\rho_{33}, \tag{D.9c}$$

$$\dot{\rho}_{44} = -\frac{\mathrm{i}}{\hbar}\mathbf{d}_{14} \cdot \mathbf{E}^{\mathrm{pump}}(t)\,(\rho_{41} - \rho_{14}) - \gamma_{43}\rho_{44}, \tag{D.9d}$$

$$\dot{\rho}_{14} = \frac{\mathrm{i}}{\hbar}\mathbf{d}_{14} \cdot \mathbf{E}^{\mathrm{pump}}(t)\,(\rho_{44} - \rho_{11}) - \frac{\gamma_{43}}{2}\rho_{14} + \mathrm{i}\omega_{14}\rho_{14}, \tag{D.9e}$$

$$\dot{\rho}_{23} = \frac{\mathrm{i}}{\hbar}\left[\mathbf{d}_{23} \cdot \mathbf{E}^{\mathrm{probe}}(t) - (g^*_{23} + g_{23})\right](\rho_{33} - \rho_{22}) - \frac{\gamma_{21}}{2}\rho_{23} + \mathrm{i}\omega_{23}\rho_{23}, \tag{D.9f}$$

where we have defined $\omega_{14} = \varepsilon_4 - \varepsilon_1$, and $\omega_{23} = \varepsilon_3 - \varepsilon_2$, and we have assumed the optical pump to be nearly resonant with the $1 \to 4$ transition ($\omega' \simeq \omega_{14}$) and the probe field to be nearly resonant with the $2 \to 3$ transition ($\omega \simeq \omega_{23}$). In the following, we define $\mathbf{d}_{23} \cdot \mathbf{E}^{\mathrm{loc}}(t) = \mathbf{d}_{23} \cdot \mathbf{E}^{\mathrm{prob}}(t) - (g^*_{23} + g_{23})$ for simplicity. Separating real and imaginary parts of the coherences $\rho_{14} = \rho^{\mathrm{R}}_{14} + \mathrm{i}\rho^{\mathrm{I}}_{14}$ and $\rho_{23} = \rho^{\mathrm{R}}_{23} + \mathrm{i}\rho^{\mathrm{I}}_{23}$, also

noting $\rho_{41}-\rho_{14}=-2\mathrm{i}\rho_{14}^{\mathrm{I}}$ and $\rho_{32}-\rho_{23}=-2\mathrm{i}\rho_{23}^{\mathrm{I}}$, one finds

$$\dot{\rho}_{11}=\frac{2}{\hbar}\mathbf{d}_{14}\cdot\mathbf{E}^{\mathrm{pump}}(t)\rho_{14}^{\mathrm{I}}+\gamma_{21}\rho_{22}, \tag{D.10a}$$

$$\dot{\rho}_{22}=\frac{2}{\hbar}\mathbf{d}_{23}\cdot\mathbf{E}^{\mathrm{loc}}(t)\rho_{23}^{\mathrm{I}}-\gamma_{21}\rho_{22}+\gamma_{32}\rho_{33}, \tag{D.10b}$$

$$\dot{\rho}_{33}=-\frac{2}{\hbar}\mathbf{d}_{23}\cdot\mathbf{E}^{\mathrm{loc}}(t)\rho_{23}^{\mathrm{I}}+\gamma_{43}\rho_{44}-\gamma_{32}\rho_{33}, \tag{D.10c}$$

$$\dot{\rho}_{44}=-\frac{2}{\hbar}\mathbf{d}_{14}\cdot\mathbf{E}^{\mathrm{pump}}(t)\rho_{14}^{\mathrm{I}}-\gamma_{43}\rho_{44}, \tag{D.10d}$$

$$\dot{\rho}_{14}^{\mathrm{R}}=-\omega_{14}\rho_{14}^{\mathrm{I}}-\frac{\gamma_{43}}{2}\rho_{14}^{\mathrm{R}}, \tag{D.10e}$$

$$\dot{\rho}_{14}^{\mathrm{I}}=\frac{1}{\hbar}\mathbf{d}_{14}\cdot\mathbf{E}^{\mathrm{pump}}(t)\left(\rho_{44}-\rho_{11}\right)-\frac{\gamma_{43}}{2}\rho_{14}^{\mathrm{I}}+\omega_{14}\rho_{14}^{\mathrm{R}}, \tag{D.10f}$$

$$\dot{\rho}_{23}^{\mathrm{R}}=-\omega_{23}\rho_{23}^{\mathrm{I}}-\frac{\gamma_{21}+\gamma_{32}}{2}\rho_{23}^{\mathrm{R}}, \tag{D.10g}$$

$$\dot{\rho}_{23}^{\mathrm{I}}=\frac{1}{\hbar}\mathbf{d}_{23}\cdot\mathbf{E}^{\mathrm{loc}}(t)\left(\rho_{33}-\rho_{22}\right)-\frac{\gamma_{21}}{2}\rho_{23}^{\mathrm{I}}+\omega_{23}\rho_{23}^{\mathrm{R}}. \tag{D.10h}$$

Take the time derivative of Eq. (D.10)(e) and combine it with Eq. (D.10)(f), we obtain

$$\ddot{\rho}_{14}^{\mathrm{R}}+\gamma_{43}\dot{\rho}_{14}^{\mathrm{R}}+\left(\omega_{14}^{2}+\frac{\gamma_{43}^{2}}{4}\right)\rho_{14}^{\mathrm{R}}=-\frac{\omega_{14}}{\hbar}\mathbf{d}_{14}\cdot\mathbf{E}^{\mathrm{pump}}(t)\left(\rho_{44}-\rho_{11}\right). \tag{D.11}$$

Because the electric dipole moment induced in the atom is given by $\mathbf{p}(t)=\mathrm{Tr}\left\{\mathbf{d}_{12}(\sigma_{12}^{\dagger}+\sigma_{12})\rho\right\}$, so, the equation of motion of $\mathbf{p}_a$ (a stands for absorption) is

$$\ddot{p}_a+\gamma_{43}\dot{p}_a+\left(\omega_{14}^{2}+\frac{\gamma_{43}^{2}}{4}\right)p_a=-\frac{2\omega_{14}}{\hbar}\mathbf{d}_{14}\cdot\left[\mathbf{d}_{14}\cdot\mathbf{E}^{\mathrm{pump}}(t)\right]\left(\rho_{44}-\rho_{11}\right). \tag{D.12}$$

We assume the atom density is N, then the polarization density $\mathbf{P}_a=\mathbf{p}_aN$. The population density $N_i=\rho_{ii}N$ (i=1,2,3,4). If the dipole moments are assumed to be parallel with the pump field, then

$$\ddot{\mathbf{P}}_{\mathrm{a}}+\gamma_{43}\dot{\mathbf{P}}_{\mathrm{a}}+\left(\omega_{14}^{2}+\frac{\gamma_{43}^{2}}{4}\right)\mathbf{P}_{\mathrm{a}}=-\frac{2\omega_{14}d_{14}^{2}}{\hbar}\mathbf{E}^{\mathrm{pump}}(t)\left(N_4-N_1\right). \tag{D.13}$$

Similarity, combining Eq. (D.10)(g) and Eq. (D.10)(h), we have

$$\ddot{\mathbf{P}}_{\mathrm{e}} + (\gamma_{21} + \gamma_{32})\,\dot{\mathbf{P}}_{\mathrm{e}} + \left[\omega_{23}^2 + \left(\frac{\gamma_{21} + \gamma_{32}}{2}\right)^2\right]\mathbf{P}_{\mathrm{e}} = -\frac{2\omega_{23}d_{23}^2}{\hbar}\mathbf{E}^{\mathrm{loc}}(t)\,(N_3 - N_2)\,, \tag{D.14}$$

where the subscript e stands for emission.

Next, we derive equations of motion for the population densities. Pluging the expression of ρ_{14}^{I} based on Eq. D.10(e) into Eq. (D.10)(a), we have

$$\dot{\rho_{11}} = -\frac{1}{\hbar\omega_{14}}\mathbf{E}^{\mathrm{pump}}(t)\left[2\mathbf{d}_{14}\cdot\dot{\rho}_{14}^{\mathrm{R}} + \frac{\gamma_{43}}{2}\left(2\mathbf{d}_{14}\cdot\rho_{14}^{\mathrm{R}}\right)\right] + \gamma_{21}\rho_{22}. \tag{D.15}$$

Recall that $\mathrm{P_a}(t) = 2\mathbf{d}_{14}\rho_{14}^{\mathrm{R}}N$ and $N_1 = \rho_{11}N$, so we have

$$\dot{N}_1 = -\frac{1}{\hbar\omega_{14}}\mathbf{E}^{\mathrm{pump}}(t)\left(\dot{\mathbf{P}}_{\mathrm{a}} + \frac{\gamma_{43}}{2}\mathbf{P}_{\mathrm{a}}\right) + \gamma_{21}N_2. \tag{D.16}$$

In a similar way, we can also get

$$\dot{N}_2 = -\frac{1}{\hbar\omega_{23}}\mathbf{E}^{\mathrm{loc}}(t)\left(\dot{\mathbf{P}}_{\mathrm{e}} + \frac{\gamma_{32} + \gamma_{21}}{2}\mathbf{P}_{\mathrm{e}}\right) - \gamma_{21}N_2 + \gamma_{32}N_3, \tag{D.17a}$$

$$\dot{N}_3 = \frac{1}{\hbar\omega_{23}}\mathbf{E}^{\mathrm{loc}}(t)\left(\dot{\mathbf{P}}_{\mathrm{e}} + \frac{\gamma_{32} + \gamma_{21}}{2}\mathbf{P}_{\mathrm{e}}\right) + \gamma_{43}N_4 - \gamma_{32}N_3, \tag{D.17b}$$

$$\dot{N}_4 = \frac{1}{\hbar\omega_{14}}\mathbf{E}^{\mathrm{pump}}(t)\left(\dot{\mathbf{P}}_{\mathrm{a}} + \frac{\gamma_{43}}{2}\mathbf{P}_{\mathrm{a}}\right) - \gamma_{43}N_4. \tag{D.17c}$$

Equation (D.13)-(D.17) resembles the Eq. (1,2) in [95], which are widely used to characterize dynamics of gain. Based on this, we derive polarizability of 3-level atoms in stationary state (see Appendix E).

Appendix E

Quantum-mechanical description of three-level atoms

In the last appendix, we have introduced the method to derive time evolution equations of four-level atoms. Based on it, we will derive polarizability of an atom in stationary state but for three-level atoms, as well as the Green function for description of interactions among them. These two parts are used in Chapter 4 to calculate light scattering on regular three-level atom arrays.

The derivation process of time evolution equations of three-level atoms is very similar with that of four-level atoms. One can easily follow Eq. (D.1) to Eq. (D.10)

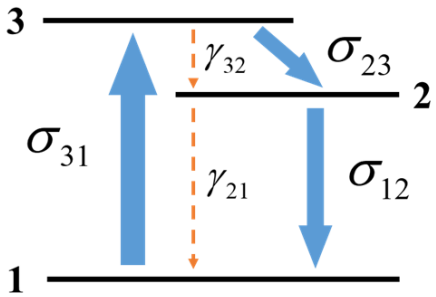

Figure E.1: Sketch of the 3-level system considered in our calculations.

to get rate equations of three-level atoms as

$$\begin{aligned}
\dot{\rho}_{11} &= \frac{2}{\hbar}\left[\mathbf{d}_{12}\cdot\mathbf{E}^{\text{probe}}(t) - (g_{12}^{*}+g_{12})\right]\rho_{12}^{\text{I}} + \frac{2}{\hbar}\mathbf{d}_{13}\cdot\mathbf{E}^{\text{pump}}(t)\rho_{13}^{\text{I}} + \gamma_{21}\rho_{22},\\
\dot{\rho}_{22} &= -\frac{2}{\hbar}\left[\mathbf{d}_{12}\cdot\mathbf{E}^{\text{probe}}(t) - (g_{12}^{*}+g_{12})\right]\rho_{12}^{\text{I}} + \gamma_{32}\rho_{33} - \gamma_{21}\rho_{22},\\
\dot{\rho}_{33} &= -\frac{2}{\hbar}\mathbf{d}_{13}\cdot\mathbf{E}^{\text{pump}}(t)\rho_{13}^{\text{I}} - \gamma_{32}\rho_{33},\\
\dot{\rho}_{12}^{\text{R}} &= -\omega_0\rho_{12}^{\text{I}} - \frac{\gamma_{21}}{2}\rho_{12}^{\text{R}},\\
\dot{\rho}_{12}^{\text{I}} &= \omega_0\rho_{12}^{\text{R}} + \frac{1}{\hbar}\left[\mathbf{d}_{12}\cdot\mathbf{E}^{\text{probe}}(t) - (g_{12}^{*}+g_{12})\right](\rho_{22}-\rho_{11}) - \frac{\gamma_{21}}{2}\rho_{12}^{\text{I}},\\
\dot{\rho}_{13}^{\text{R}} &= -\omega_0'\rho_{13}^{\text{I}} - \frac{\gamma_{32}}{2}\rho_{13}^{\text{R}},\\
\dot{\rho}_{13}^{\text{I}} &= \omega_0'\rho_{13}^{\text{R}} + \frac{1}{\hbar}\mathbf{d}_{13}\cdot\mathbf{E}^{\text{pump}}(t)(\rho_{33}-\rho_{11}) - \frac{\gamma_{32}}{2}\rho_{13}^{\text{I}}.
\end{aligned}$$

A sketch of the studied three-level atom is shown in Fig. E.1. Eliminating ρ_{12}^{I} and ρ_{13}^{I}, we obtain

$$\begin{aligned}
\dot{\rho}_{11} &= -\frac{2}{\hbar\omega_0}\left[\mathbf{d}_{12}\cdot\mathbf{E}^{\text{probe}}(t) - (g_{12}^{*}+g_{12})\right]\left(\dot{\rho}_{12}^{\text{R}} + \frac{\gamma_{21}}{2}\rho_{12}^{\text{R}}\right)\\
&\quad - \frac{2}{\hbar\omega_0'}\mathbf{d}_{13}\cdot\mathbf{E}^{\text{pump}}(t)\left(\dot{\rho}_{13}^{\text{R}} + \frac{\gamma_{32}}{2}\rho_{13}^{\text{R}}\right) + \gamma_{21}\rho_{22}, && \text{(E.1a)}\\
\dot{\rho}_{22} &= \frac{2}{\hbar\omega_0}\left[\mathbf{d}_{12}\cdot\mathbf{E}^{\text{probe}}(t) - (g_{12}^{*}+g_{12})\right]\left(\dot{\rho}_{12}^{\text{R}} + \frac{\gamma_{21}}{2}\rho_{12}^{\text{R}}\right) + \gamma_{32}\rho_{33} - \gamma_{21}\rho_{22}, && \text{(E.1b)}\\
\dot{\rho}_{33} &= \frac{2}{\hbar\omega_0'}\mathbf{d}_{13}\cdot\mathbf{E}^{\text{pump}}(t)\left(\dot{\rho}_{13}^{\text{R}} + \frac{\gamma_{32}}{2}\rho_{13}^{\text{R}}\right) - \gamma_{32}\rho_{33}, && \text{(E.1c)}\\
\ddot{\rho}_{12}^{\text{R}} &+ \gamma_{21}\dot{\rho}_{12}^{\text{R}} + \left(\omega_0^2 + \frac{\gamma_{21}^2}{4}\right)\rho_{12}^{\text{R}} = -\frac{\omega_0}{\hbar}(\rho_{22}-\rho_{11})\left[\mathbf{d}_{12}\cdot\mathbf{E}^{\text{probe}}(t) - (g_{12}^{*}+g_{12})\right], && \text{(E.1d)}\\
\ddot{\rho}_{13}^{\text{R}} &+ \gamma_{32}\dot{\rho}_{13}^{\text{R}} + \left(\omega'^{2}_{0} + \frac{\gamma_{32}^2}{4}\right)\rho_{13}^{\text{R}} = -\frac{\omega_0'}{\hbar}(\rho_{33}-\rho_{11})\,\mathbf{d}_{13}\cdot\mathbf{E}^{\text{pump}}(t), && \text{(E.1e)}\\
\rho_{12}^{\text{I}} &= -\frac{1}{\omega_0}\left(\dot{\rho}_{12}^{\text{R}} + \frac{\gamma_{21}}{2}\rho_{12}^{\text{R}}\right), && \text{(E.1f)}\\
\rho_{13}^{\text{I}} &= -\frac{1}{\omega_0'}\left(\dot{\rho}_{13}^{\text{R}} + \frac{\gamma_{32}}{2}\rho_{13}^{\text{R}}\right). && \text{(E.1g)}
\end{aligned}$$

It is straightforward to verify the condition $\sum_l \dot{\rho}_{ll} = 0$, confirming that the total population $\sum_l \rho_{ll} = 1$ is conserved.

From here, we start to derive the steady-state operation conditions for continuous-wave pump and probe at frequencies ω' and ω, respectively. For the sake of compactness, we introduce the new variables η and η', accounting for the probe and pump electric field amplitudes and implicitly defined by

$$\frac{1}{\hbar}\left[\mathbf{d}_{12}\cdot\mathbf{E}^{\text{probe}}(t)-(g_{12}^{*}+g_{12})\right]=\frac{1}{\hbar}\mathbf{d}_{12}\cdot\mathbf{E}^{\text{loc}}(t)=\eta\mathrm{e}^{-\mathrm{i}\omega t}+\text{c.c.}, \tag{E.2a}$$

$$\frac{1}{\hbar}\mathbf{d}_{13}\cdot\mathbf{E}^{\text{pump}}(t)=\eta'\mathrm{e}^{-\mathrm{i}\omega' t}+\text{c.c.}, \tag{E.2b}$$

where the g_{12} terms, representing the induced field (see below), have been absorbed into the local field $\mathbf{E}^{\text{loc}}$. Inserting these expressions into the density-matrix equations (E.1), anticipating the steady-state time dependences $\dot{\rho}_{11}=\dot{\rho}_{22}=\dot{\rho}_{33}=0$,

$$\rho_{12}^{\text{R}}=\xi\mathrm{e}^{-\mathrm{i}\omega t}+\text{c.c.},$$
$$\rho_{13}^{\text{R}}=\xi'\mathrm{e}^{-\mathrm{i}\omega' t}+\text{c.c.},$$

and adopting the rotating-wave approximation (RWA), we find

$$\rho_{11}=\frac{\left(1+\gamma_{32}^{-1}\Delta'\right)\left(1+\gamma_{21}^{-1}\Delta\right)}{1+2\gamma_{21}^{-1}\Delta+\left(\gamma_{21}^{-1}+2\gamma_{32}^{-1}\right)\Delta'+3\gamma_{21}^{-1}\gamma_{32}^{-1}\Delta\Delta'}, \tag{E.4a}$$

$$\rho_{22}=\frac{\gamma_{21}^{-1}(\Delta+\Delta')+\gamma_{21}^{-1}\gamma_{32}^{-1}\Delta\Delta'}{1+2\gamma_{21}^{-1}\Delta+\left(\gamma_{21}^{-1}+2\gamma_{32}^{-1}\right)\Delta'+3\gamma_{21}^{-1}\gamma_{32}^{-1}\Delta\Delta'}, \tag{E.4b}$$

$$\rho_{33}=\frac{\gamma_{32}^{-1}\Delta'\left(1+\gamma_{21}^{-1}\Delta\right)}{1+2\gamma_{21}^{-1}\Delta+\left(\gamma_{21}^{-1}+2\gamma_{32}^{-1}\right)\Delta'+3\gamma_{21}^{-1}\gamma_{32}^{-1}\Delta\Delta'}, \tag{E.4c}$$

$$\xi=\frac{\omega_0\eta}{(\omega+\mathrm{i}\gamma_{21}/2)^2-\omega_0^2}\left(\rho_{22}-\rho_{11}\right), \tag{E.4d}$$

$$\xi'=\frac{\omega_0'\eta'}{(\omega'+\mathrm{i}\gamma_{32}/2)^2-\omega_0'^2}\left(\rho_{33}-\rho_{11}\right), \tag{E.4e}$$

where we use

$$\Delta = 4|\eta|^2 \mathrm{Im}\left\{\frac{-1}{(\omega+\mathrm{i}\gamma_{21}/2)-\omega_0^2/(\omega+\mathrm{i}\gamma_{21}/2)}\right\} = \frac{2\gamma_{21}|\eta|^2\left(\omega^2+\omega_0^2+\gamma_{21}^2/4\right)}{\left(\omega^2-\omega_0^2-\gamma_{21}^2/4\right)^2+\gamma_{21}^2\omega^2}, \tag{E.5a}$$

$$\Delta' = 4|\eta'|^2 \mathrm{Im}\left\{\frac{-1}{(\omega'+\mathrm{i}\gamma_{32}/2)-\omega'^2_0/(\omega'+\mathrm{i}\gamma_{32}/2)}\right\} = \frac{2\gamma_{32}|\eta'|^2\left(\omega'^2+\omega_0'^2+\gamma_{32}^2/4\right)}{\left(\omega'^2-\omega_0'^2-\gamma_{32}^2/4\right)^2+\gamma_{32}^2\omega'^2}. \tag{E.5b}$$

Now, the electric dipole moment induced in the atom is given by $\mathbf{p} = \sum_{ii'} \mathbf{d}_{ii'} \,\mathrm{Tr}\left\{\left(\sigma^\dagger_{lii'}+\sigma_{lii'}\right)\rho\right\}$, and in particular, the component oscillating at frequency ω reduces to

$$\mathbf{p}(t) = \mathrm{Tr}\left\{\mathbf{d}_{12}(\sigma_{12}^\dagger+\sigma_{12})\rho\right\} = 2\mathbf{d}_{12}\,\mathrm{Re}\{\rho_{12}\} = 2\mathbf{d}_{12}\left(\xi \mathrm{e}^{-\mathrm{i}\omega t}+\xi^* \mathrm{e}^{\mathrm{i}\omega t}\right) = \mathbf{p}\,\mathrm{e}^{-\mathrm{i}\omega t}+\mathrm{c.c.}, \tag{E.6}$$

from which we obtain

$$\mathbf{p} = 2\mathbf{d}_{12}\,\xi = \frac{2\mathbf{d}_{12}\omega_0\eta}{(\omega+\mathrm{i}\gamma_{21}/2)^2-\omega_0^2}\left(\rho_{22}-\rho_{11}\right). \tag{E.7}$$

In order to derive the response of the atomic ensemble to the probe field, we consider the steady-state amplitude α_n of each photon mode of electric field $\mathbf{e}_{nl} = \mathbf{e}_n(\mathbf{r}_l)$, evaluated at the position of every atom l. The coupling coefficients are then $g_{nl\,12} = -\mathbf{d}_{12}\cdot\mathbf{e}_{nl}$. By using Eq. (E.6) in Eq. (D.4), we find

$$\alpha_n = \beta_n^- \mathrm{e}^{-\mathrm{i}\omega t} + \beta_n^+ \mathrm{e}^{\mathrm{i}\omega t}$$

with coefficients

$$\beta_n^- = \frac{1}{\hbar(\omega_n-\omega-\mathrm{i}\Gamma_n/2)}\sum_l \mathbf{e}_{nl}^*\cdot\mathbf{p}_l,$$
$$\beta_n^+ = \frac{1}{\hbar(\omega_n+\omega-\mathrm{i}\Gamma_n/2)}\sum_l \mathbf{e}_{nl}^*\cdot\mathbf{p}_l^*,$$

where we reinsert the l dependence in the sums over atoms. From here, using Eq. (D.7), we find

$$g_{l12} + g_{l12}^* = \sum_n (g_{nl12}\alpha_n + g_{nl12}^*\alpha_n^*) = -\mathbf{d}_{12} \cdot \mathcal{G}_{ll'} \cdot \mathbf{p}_{l'} \mathrm{e}^{-\mathrm{i}\omega t} + \text{c.c.}, \tag{E.8}$$

where we define

$$\mathcal{G}_{ll'} = \frac{1}{\hbar} \sum_n \left[\frac{\mathbf{e}_{nl} \otimes \mathbf{e}_{nl'}^*}{\omega_n - \omega - \mathrm{i}\Gamma_n/2} + \frac{\mathbf{e}_{nl}^* \otimes \mathbf{e}_{nl'}}{\omega_n + \omega + \mathrm{i}\Gamma_n/2} \right] \tag{E.9}$$

as the electromagnetic Green tensor. As noted above [see Eq. (E.2a)], the total local field at frequency ω acting on emitter l is given by the sum of the external field and the induced field produced by the emitters, that is, $\mathbf{E}_l^{\mathrm{loc}} = \mathbf{E}_l^{\mathrm{probe}} + \mathbf{E}_l^{\mathrm{ind}}$, where the induced field can be expressed, according to Eq. (E.8), in terms of the Green tensor as $\mathbf{E}_l^{\mathrm{ind}}(t) = \sum_{l'} \mathcal{G}_{ll'} \cdot \mathbf{p}_{l'} \mathrm{e}^{-\mathrm{i}\omega t} + \text{c.c.}$, so the total local field becomes

$$\mathbf{E}_l^{\mathrm{loc}}(t) = \left(\mathbf{E}_l^{\mathrm{probe}} + \sum_{l'} \mathcal{G}_{ll'} \cdot \mathbf{p}_{l'} \right) \mathrm{e}^{-\mathrm{i}\omega t} + \text{c.c.}$$

Finally, recalling that $(1/\hbar)\mathbf{d}_{12} \cdot \mathbf{E}_l^{\mathrm{loc}}(t) = \eta_l \mathrm{e}^{-\mathrm{i}\omega t} + \text{c.c.}$ [see Eq. (E.2a)] and using Eq. (E.7), we obtain the coupled-dipole equations

$$\mathbf{p}_l = \tilde{\alpha}(\omega) \left[\mathbf{E}_l^{\mathrm{probe}} + \sum_{l'} \mathcal{G}_{ll'} \cdot \mathbf{p}_{l'} \right], \tag{E.10}$$

where

$$\tilde{\alpha}(\omega) = \frac{2\omega_0 \delta n}{\hbar} \frac{\mathbf{d}_{12} \otimes \mathbf{d}_{12}}{(\omega + \mathrm{i}\gamma_{21}/2)^2 - \omega_0^2}$$

is the electrostatic polarizability tensor at a frequency ω near $\omega_0 = \varepsilon_2 - \varepsilon_1$, and [see Eqs. (E.4)]

$$\delta n = \rho_{22} - \rho_{11} = \frac{\left(\gamma_{21}^{-1} - \gamma_{32}^{-1}\right)\Delta' - 1}{1 + 2\gamma_{21}^{-1}\Delta + \left(\gamma_{21}^{-1} + 2\gamma_{32}^{-1}\right)\Delta' + 3\gamma_{21}^{-1}\gamma_{32}^{-1}\Delta\Delta'} \tag{E.11}$$

is the population difference of the emitter.

Now, it is useful to recast the expression of δn in terms of pump and local field amplitudes. We first rewrite Eq. (E.5a) using Eq. (E.2a) as

$$\Delta = \mathcal{I}\,\frac{2\gamma_{21}^3\left(\omega^2+\omega_0^2+\gamma_{21}^2/4\right)}{\left(\omega^2-\omega_0^2-\gamma_{21}^2/4\right)^2+\gamma_{21}^2\omega^2},$$

where we have assumed $\mathbf{E}^{\mathrm{loc}}$ to be oriented along $\mathbf{d}_{12}$, the l dependence is again implicitly understood, and we have defined

$$\mathcal{I} = \left|\mathbf{E}^{\mathrm{loc}}/E_{\mathrm{sat}}^{\mathrm{probe}}\right|^2, \qquad E_{\mathrm{sat}}^{\mathrm{probe}} = \hbar\gamma_{21}/d_{12}.$$

Additionally, we approximate $\gamma_{32} \ll \omega'$ and consider resonant pumping $\omega' = \omega_0'$, so that Eq. (E.5b) together with Eq. (E.2b) leads to

$$\Delta' = \mathcal{I}'\,\gamma_{21}, \tag{E.12}$$

where

$$\mathcal{I}' = |\mathbf{E}^{\mathrm{pump}}/E_{\mathrm{ref}}^{\mathrm{pump}}|^2, \qquad E_{\mathrm{ref}}^{\mathrm{pump}} = (\hbar/2)\sqrt{\gamma_{21}\gamma_{32}}/d_{13}. \tag{E.13}$$

Incidentally, we note the relation $I = c|E|^2/2\pi$ between the light intensity I and electric field E in Gaussian units, which allows us to directly define a relation between E^{pump}, E^{probe}, and the corresponding pump and probe intensities.

We conclude by expressing some of the above quantities in terms of δn. In particular, we find

$$\Delta = \frac{1}{2}\,\frac{(1-\mathcal{R})\mathcal{I}' - 1 - [(1+2\mathcal{R})\mathcal{I}'+1]\;\delta n}{1+(3/2)\mathcal{R}\mathcal{I}'}, \tag{E.14}$$

which in turns allows us to rewrite Eqs. (E.4a)-(E.4c) as

$$\rho_{11} = [(1+\mathcal{R}\mathcal{I}')/(2+3\mathcal{R}\mathcal{I}')]\;(1-\delta n), \tag{E.15a}$$

$$\rho_{22} = [(1+\mathcal{R}\mathcal{I}') + (1+2\mathcal{R}\mathcal{I}')\,\delta n]\,/(2+3\mathcal{R}\mathcal{I}'), \tag{E.15b}$$

$$\rho_{33} = [\mathcal{R}\mathcal{I}'/(2+3\mathcal{R}\mathcal{I}')]\;(1-\delta n), \tag{E.15c}$$

where

$$\mathcal{R} = \gamma_{21}/\gamma_{32}.$$

Incidentally, in the $\gamma_{21} << \gamma_{32}$ limit, assuming $\delta = \omega - \omega_0 \ll \omega_0$ and $\gamma_{21} \ll \omega_0$, the population difference reduces to

$$\delta n = \frac{-1 + \mathcal{I}'}{1 + 8\mathcal{I}(1 + 3\mathcal{I}'\gamma_{21}/2\gamma_{32})/(1 + 4\delta^2/\gamma_{21}^2) + \mathcal{I}'}.$$

Now, we prove that the quantum-mechnically derived electromagnetic Green tensor (E.9) can go back to its classical form. The atoms we consider are in vacuum. The electromagnetic Green tensor can then be worked out by using plane waves for the photon states, $\mathbf{e}_n(\mathbf{r}_l) = -\mathrm{i}\sqrt{2\pi\hbar qc/V}\,\mathrm{e}^{\mathrm{i}\mathbf{q}\cdot\mathbf{r}_l}\hat{\varepsilon}_\sigma$ with $\omega_n = qc$, in which the mode index n is multiplexed as $n \to \{\mathbf{q}, \sigma\}$, where $\mathbf{q}$ is the light wave vector, $\sigma = \mathrm{s}, \mathrm{p}$ is the polarization state corresponding to the unit vector $\hat{\varepsilon}_\sigma$, and V is the normalization volume. Additionally, the sum over photon modes becomes an integral using the substitution $\sum_n \to V \sum_\sigma \int d^3\mathbf{q}/(2\pi)^3$. Also, we find the Green tensor $\mathcal{G}_{ll'}(\omega) = \mathcal{G}(\mathbf{r}_l - \mathbf{r}_{l'}, \omega)$ to only depend on the relative coordinate vector $\mathbf{r} = \mathbf{r}_l - \mathbf{r}_{l'}$. Putting these ingredients together, we find from Eq. (E.9)

$$\mathcal{G}(\mathbf{r}, \omega) = \int \frac{d^3\mathbf{q}}{(2\pi)^3} \frac{4\pi q^2\,\mathrm{e}^{\mathrm{i}\mathbf{q}\cdot\mathbf{r}}}{q^2 - (k + i0^\dagger)^2} \sum_\sigma \hat{\boldsymbol{\varepsilon}}_\sigma \otimes \hat{\boldsymbol{\varepsilon}}_\sigma,$$

where $k = \omega/c$ and we have replaced $\Gamma_n/2 \to 0^+$, as appropriate for photons in free space. Now, the sum over σ can be transformed using the expression $\sum_\sigma \hat{\varepsilon}_\sigma \otimes \hat{\varepsilon}_\sigma = \mathcal{I}_3 - \hat{\mathbf{q}} \otimes \hat{\mathbf{q}}$, where $\mathcal{I}_3$ is the 3×3 identity matrix, while $\hat{\mathbf{q}}$ is the

unit vector along $\mathbf{q}$. Additionally, $\mathbf{q}$ can be replaced by $-\mathrm{i}\nabla$. This leads to

$$\begin{aligned}\mathcal{G}(\mathbf{r},\omega) &= \int \frac{d^3\mathbf{q}}{(2\pi)^3}\,(\mathcal{I}_3 q^2 - \mathbf{q}\otimes\mathbf{q})\,\frac{4\pi\,\mathrm{e}^{\mathrm{i}\mathbf{q}\cdot\mathbf{r}}}{q^2-(k+i0^\dagger)^2}\\ &= (-\nabla^2\mathcal{I}_3 + \nabla\otimes\nabla)\int \frac{d^3\mathbf{q}}{(2\pi)^3}\,\frac{4\pi\,\mathrm{e}^{\mathrm{i}\mathbf{q}\cdot\mathbf{r}}}{q^2-(k+i0^\dagger)^2}\\ &= (k^2\mathcal{I}_3 + \nabla\otimes\nabla)\frac{\mathrm{e}^{\mathrm{i}kr}}{r}\\ &= \frac{\mathrm{e}^{\mathrm{i}kr}}{r^3}\left[(k^2r^2+\mathrm{i}kr-1)\mathcal{I}_3 - (k^2r^2+3\mathrm{i}kr-3)\frac{\mathbf{r}\otimes\mathbf{r}}{r^2}\right], \end{aligned} \tag{E.16}$$

which is the well-known dipole-dipole interaction tensor in free space. Incidentally, we have replaced $\nabla^2 \to -k^2$ in the third line of the above derivation because $(\nabla^2+k^2)\mathrm{e}^{\mathrm{i}kr}/r = \delta(\mathbf{r})$ and we only need to evaluate the Green tensor for $\mathbf{r}\neq 0$.

We emphasis that the Eq. (E.11) is the electrostatic polarizability tensor of an atom. The self-interaction term $l' = l$ in Eq. (E.10) involves $\mathcal{G}_{ll}$. The real part of this term exhibits a divergence originating in the electrostatic interaction of two point dipoles at vanishing separation. This divergence can be effectively absorbed as an atomic resonance frequency shift. A detailed treatment of this effect requires a rather involved analysis [190] that goes beyond the scope of the present work, so we just ignore it and assume it to be correctly incorporated in the atomic resonance frequency. However, the remaining imaginary part remains finite. In the limit of small mode decay rates Γ_n, we obtain from Eq. (E.16)

$$\mathrm{Im}\,\{\hat{\mathbf{n}}\cdot\mathcal{G}_{ll}\cdot\hat{\mathbf{n}}\} = 2\omega^3/3c^3.$$

Self-interaction can be understood as a radiative-reaction contribution to the response of the atom. Assuming an isotropic environment, one can conveniently absorb it in a corrected polarizability

$$\alpha(\omega) = \frac{1}{1/\tilde{\alpha}(\omega) - 2\mathrm{i}\omega^3/3c^3},$$

while the coupled-dipole equations are modified as

$$\mathbf{p}_l = \alpha(\omega)\left[\mathbf{E}_l^{\text{probe}} + \sum_{l' \neq l} \mathcal{G}_{ll'} \cdot \mathbf{p}_{l'}\right], \tag{E.17}$$

so that the $l' = l$ term is excluded from the sum.

Bibliography

[1] Stefan Alexander Maier. *Plasmonics: fundamentals and applications*. Springer Science and Business Media, 2007.

[2] Ravishankar Sundararaman, Prineha Narang, Adam S Jermyn, William A Goddard III, and Harry A Atwater. Theoretical predictions for hot-carrier generation from surface plasmon decay. *Nature communications*, 5:5788, 2014.

[3] Mark L Brongersma, Naomi J Halas, and Peter Nordlander. Plasmon-induced hot carrier science and technology. *Nature nanotechnology*, 10(1):25, 2015.

[4] Guillaume Baffou and Romain Quidant. Thermo-plasmonics: using metallic nanostructures as nano-sources of heat. *Laser and photonics reviews*, 7(2):171–187, 2013.

[5] Lijun Meng, Renwen Yu, Min Qiu, and F Javier García de Abajo. Plasmonic nano-oven by concatenation of multishell photothermal enhancement. *ACS nano*, 11(8):7915–7924, 2017.

[6] Matthias Danckwerts and Lukas Novotny. Optical frequency mixing at coupled gold nanoparticles. *Physical review letters*, 98(2):026104, 2007.

[7] Seungchul Kim, Jonghan Jin, Young-Jin Kim, In-Yong Park, Yunseok Kim, and Seung-Woo Kim. High-harmonic generation by resonant plasmon field enhancement. *Nature*, 453(7196):757, 2008.

[8] Katrin Kneipp, Yang Wang, Harald Kneipp, Lev T Perelman, Irving Itzkan, Ramachandra R Dasari, and Michael S Feld. Single molecule detection using

surface-enhanced raman scattering (sers). *Physical review letters*, 78(9):1667, 1997.

[9] Shuming Nie and Steven R Emory. Probing single molecules and single nanoparticles by surface-enhanced raman scattering. *Science*, 275(5303):1102–1106, 1997.

[10] CJ Chen and RM Osgood. Direct observation of the local-field-enhanced surface photochemical reactions. *Physical review letters*, 50(21):1705, 1983.

[11] Shaunak Mukherjee, Florian Libisch, Nicolas Large, Oara Neumann, Lisa V Brown, Jin Cheng, J Britt Lassiter, Emily A Carter, Peter Nordlander, and Naomi J Halas. Hot electrons do the impossible: plasmon-induced dissociation of h2 on au. *Nano letters*, 13(1):240–247, 2012.

[12] Erik C Garnett, Wenshan Cai, Judy J Cha, Fakhruddin Mahmood, Stephen T Connor, M Greyson Christoforo, Yi Cui, Michael D McGehee, and Mark L Brongersma. Self-limited plasmonic welding of silver nanowire junctions. *Nature materials*, 11(3):241, 2012.

[13] Hangbo Yang, Jinsheng Lu, Pintu Ghosh, Ziyao Chen, Wei Wang, Hui Ye, Qian Yu, Min Qiu, and Qiang Li. Plasmonic-enhanced targeted nanohealing of metallic nanostructures. *Applied physics letters*, 112(7):071108, 2018.

[14] Changjun Min, Jinpeng Liu, Ting Lei, Guangyuan Si, Zhenwei Xie, Jiao Lin, Luping Du, and Xiaocong Yuan. Plasmonic nano-slits assisted polarization selective detour phase meta-hologram. *Laser and photonics reviews*, 10(6):978–985, 2016.

[15] Zhenwei Xie, Ting Lei, Guangyuan Si, Xianyou Wang, Jiao Lin, Changjun Min, and Xiaocong Yuan. Meta-holograms with full parameter control of wavefront over a 1000 nm bandwidth. *ACS photonics*, 4(9):2158–2164, 2017.

[16] Jiaming Hao, Jing Wang, Xianliang Liu, Willie J Padilla, Lei Zhou, and Min Qiu. High performance optical absorber based on a plasmonic metamaterial. *Applied physics letters*, 96(25):251104, 2010.

[17] Lijun Meng, Ding Zhao, Qiang Li, and Min Qiu. Polarization-sensitive perfect absorbers at near-infrared wavelengths. *Optics express*, 21(101):A111–A122, 2013.

[18] Lijun Meng, Ding Zhao, Zhichao Ruan, Qiang Li, Yuanqing Yang, and Min Qiu. Optimized grating as an ultra-narrow band absorber or plasmonic sensor. *Optics letters*, 39(5):1137–1140, 2014.

[19] Yong-Lai Zhang, Qi-Dai Chen, Hong Xia, and Hong-Bo Sun. Designable 3d nanofabrication by femtosecond laser direct writing. *Nano today*, 5(5):435–448, 2010.

[20] John David Jackson. *Classical electrodynamics*. John Wiley & Sons, 2012.

[21] Lukas Novotny and Bert Hecht. *Principles of nano-optics*. Cambridge university press, 2012.

[22] Shunping Zhang, Kui Bao, Naomi J Halas, Hongxing Xu, and Peter Nordlander. Substrate-induced fano resonances of a plasmonic nanocube: a route to increased-sensitivity localized surface plasmon resonance sensors revealed. *Nano letters*, 11(4):1657–1663, 2011.

[23] Feng Hao, Colleen L Nehl, Jason H Hafner, and Peter Nordlander. Plasmon resonances of a gold nanostar. *Nano letters*, 7(3):729–732, 2007.

[24] FJ García de Abajo and A Howie. Relativistic electron energy loss and electron-induced photon emission in inhomogeneous dielectrics. *Physical review letters*, 80(23):5180, 1998.

[25] Gouri Dhatt, Emmanuel LefranÃ, Gilbert Touzot, et al. *Finite element method*. John Wiley and Sons, 2012.

[26] Craig F Bohren and Donald R Huffman. *Absorption and scattering of light by small particles*. John Wiley and Sons, 2008.

[27] FJ Garcia de Abajo. Colloquium: Light scattering by particle and hole arrays. *Reviews of modern physics*, 79(4):1267, 2007.

[28] Peter B Johnson and R-W_ Christy. Optical constants of the noble metals. *Physical review B*, 6(12):4370, 1972.

[29] Claire M Watts, Xianliang Liu, and Willie J Padilla. Metamaterial electromagnetic wave absorbers. *Advanced materials*, 24(23):OP98–OP120, 2012.

[30] D RêŐň Smith, S Schultz, P Markoš, and CM Soukoulis. Determination of effective permittivity and permeability of metamaterials from reflection and transmission coefficients. *Physical Review B*, 65(19):195104, 2002.

[31] Hermann A Haus. *Waves and fields in optoelectronics*. Prentice-Hall,, 1984.

[32] Jaewoong Yoon, Kang Hee Seol, Seok Ho Song, and Robert Magnusson. Critical coupling in dissipative surface-plasmon resonators with multiple ports. *Optics express*, 18(25):25702–25711, 2010.

[33] N I Landy, S Sajuyigbe, JJ Mock, DR Smith, and WJ Padilla. Perfect metamaterial absorber. *Physical review letters*, 100(20):207402, 2008.

[34] Tatiana V Teperik, FJ García de Abajo, AG Borisov, M Abdelsalam, PN Bartlett, Y Sugawara, and JJ Baumberg. Omnidirectional absorption in nanostructured metal surfaces. *Nature photonics*, 2(5):299, 2008.

[35] TV Teperik, VV Popov, and FJ García de Abajo. Void plasmons and total absorption of light in nanoporous metallic films. *Physical review B*, 71(8):085408, 2005.

[36] Daniel Rodrigo, Odeta Limaj, Davide Janner, Dordaneh Etezadi, F Javier García de Abajo, Valerio Pruneri, and Hatice Altug. Mid-infrared plasmonic biosensing with graphene. *Science*, 349(6244):165–168, 2015.

[37] AN Grigorenko, Marco Polini, and KS Novoselov. Graphene plasmonics. *Nature photonics*, 6(11):749, 2012.

[38] F Javier Garcia de Abajo. Graphene plasmonics: challenges and opportunities. *ACS photonics*, 1(3):135–152, 2014.

[39] Sukosin Thongrattanasiri, Frank HL Koppens, and F Javier Garcia de Abajo. Complete optical absorption in periodically patterned graphene. *Physical review letters*, 108(4):047401, 2012.

[40] Seyoon Kim, Min Seok Jang, Victor W Brar, Kelly W Mauser, Laura Kim, and Harry A Atwater. Electronically tunable perfect absorption in graphene. *Nano letters*, 18(2):971–979, 2018.

[41] Kai-Kai Du, Qiang Li, Yan-Biao Lyu, Ji-Chao Ding, Yue Lu, Zhi-Yuan Cheng, and Min Qiu. Control over emissivity of zero-static-power thermal emitters based on phase-changing material gst. *Light: Science and Applications*, 6(1):e16194, 2017.

[42] Ortwin Hess, John B Pendry, Stefan A Maier, Rupert F Oulton, JM Hamm, and KL Tsakmakidis. Active nanoplasmonic metamaterials. *Nature materials*, 11(7):573, 2012.

[43] Koray Aydin, Vivian E Ferry, Ryan M Briggs, and Harry A Atwater. Broadband polarization-independent resonant light absorption using ultrathin plasmonic super absorbers. *Nature communications*, 2:517, 2011.

[44] Antoine Moreau, Cristian Ciraci, Jack J Mock, Ryan T Hill, Qiang Wang, Benjamin J Wiley, Ashutosh Chilkoti, and David R Smith. Controlled-reflectance surfaces with film-coupled colloidal nanoantennas. *Nature*, 492(7427):86, 2012.

[45] Yanxia Cui, Kin Hung Fung, Jun Xu, Hyungjin Ma, Yi Jin, Sailing He, and Nicholas X Fang. Ultrabroadband light absorption by a sawtooth anisotropic metamaterial slab. *Nano letters*, 12(3):1443–1447, 2012.

[46] Thomas Søndergaard, Sergey M Novikov, Tobias Holmgaard, René L Eriksen, Jonas Beermann, Zhanghua Han, Kjeld Pedersen, and Sergey I Bozhevolnyi. Plasmonic black gold by adiabatic nanofocusing and absorption of light in ultra-sharp convex grooves. *Nature communications*, 3:969, 2012.

[47] Harry A Atwater and Albert Polman. Plasmonics for improved photovoltaic devices. *Nature materials*, 9(3):205, 2010.

[48] Zhongyang Li, Serkan Butun, and Koray Aydin. Ultranarrow band absorbers based on surface lattice resonances in nanostructured metal surfaces. *ACS nano*, 8(8):8242–8248, 2014.

[49] Xiaoyuan Lu, Rengang Wan, and Tongyi Zhang. Metal-dielectric-metal based narrow band absorber for sensing applications. *Optics express*, 23(23):29842–29847, 2015.

[50] Yurui Qu, Qiang Li, Hanmo Gong, Kaikai Du, Songang Bai, Ding Zhao, Hui Ye, and Min Qiu. Spatially and spectrally resolved narrowband optical absorber based on 2d grating nanostructures on metallic films. *Advanced optical materials*, 4(3):480–486, 2016.

[51] Yan-Lin Liao and Yan Zhao. Graphene-based tunable ultra-narrowband mid-infrared te-polarization absorber. *Optics express*, 25(25):32080–32089, 2017.

[52] Mark W Knight, Heidar Sobhani, Peter Nordlander, and Naomi J Halas. Photodetection with active optical antennas. *Science*, 332(6030):702–704, 2011.

[53] Dong Wu, Ruifang Li, Yumin Liu, Zhongyuan Yu, Li Yu, Lei Chen, Chang Liu, Rui Ma, and Han Ye. Ultra-narrow band perfect absorber and its application as plasmonic sensor in the visible region. *Nanoscale research letters*, 12(1):427, 2017.

[54] Xianliang Liu, Talmage Tyler, Tatiana Starr, Anthony F Starr, Nan Marie Jokerst, and Willie J Padilla. Taming the blackbody with infrared metamaterials as selective thermal emitters. *Physical review letters*, 107(4):045901, 2011.

[55] Jean-Jacques Greffet, Rémi Carminati, Karl Joulain, Jean-Philippe Mulet, Stéphane Mainguy, and Yong Chen. Coherent emission of light by thermal sources. *Nature*, 416(6876):61, 2002.

[56] Alexander O Govorov and Hugh H Richardson. Generating heat with metal nanoparticles. *Nano today*, 2(1):30–38, 2007.

[57] Sergey I Bozhevolnyi, Valentyn S Volkov, Eloise Devaux, Jean-Yves Laluet, and Thomas W Ebbesen. Channel plasmon subwavelength waveguide components including interferometers and ring resonators. *Nature*, 440(7083):508, 2006.

[58] Xiaohua Huang, Prashant K Jain, Ivan H El-Sayed, and Mostafa A El-Sayed. Plasmonic photothermal therapy (pptt) using gold nanoparticles. *Lasers in medical science*, 23(3):217, 2008.

[59] Surbhi Lal, Susan E Clare, and Naomi J Halas. Nanoshell-enabled photothermal cancer therapy: impending clinical impact. *Accounts of chemical research*, 41(12):1842–1851, 2008.

[60] Mehmet Fatih Yanik, Hulusi Cinar, Hediye Nese Cinar, Andrew D Chisholm, Yishi Jin, and Adela Ben-Yakar. Neurosurgery: functional regeneration after laser axotomy. *Nature*, 432(7019):822, 2004.

[61] Alexander S Urban, Tom Pfeiffer, Michael Fedoruk, Andrey A Lutich, and Jochen Feldmann. Single-step injection of gold nanoparticles through phospholipid membranes. *ACS nano*, 5(5):3585–3590, 2011.

[62] Stéphane Berciaud, Laurent Cognet, Gerhard A Blab, and Brahim Lounis. Photothermal heterodyne imaging of individual nonfluorescent nanoclusters and nanocrystals. *Physical review letters*, 93(25):257402, 2004.

[63] A Gaiduk, M Yorulmaz, PV Ruijgrok, and M Orrit. Room-temperature detection of a single moleculeâĂŹs absorption by photothermal contrast. *Science*, 330(6002):353–356, 2010.

[64] Michael T Carlson, Andrew J Green, and Hugh H Richardson. Superheating water by cw excitation of gold nanodots. *Nano letters*, 12(3):1534–1537, 2012.

[65] Phillip Christopher, Hongliang Xin, and Suljo Linic. Visible-light-enhanced catalytic oxidation reactions on plasmonic silver nanostructures. *Nature chemistry*, 3(6):467, 2011.

[66] Gang L Liu, Jaeyoun Kim, YU Lu, and Luke P Lee. Optofluidic control using photothermal nanoparticles. *Nature materials*, 5(1):27, 2006.

[67] V Garcés-Chávez, Romain Quidant, PJ Reece, G Badenes, L Torner, and K Dholakia. Extended organization of colloidal microparticles by surface plasmon polariton excitation. *Physical review B*, 73(8):085417, 2006.

[68] Xi Chen, Yiting Chen, Min Yan, and Min Qiu. Nanosecond photothermal effects in plasmonic nanostructures. *ACS nano*, 6(3):2550–2557, 2012.

[69] Gerald L Pollack. Kapitza resistance. *Reviews of modern physics*, 41(1):48, 1969.

[70] G Baffou, R Quidant, and Ch Girard. Heat generation in plasmonic nanostructures: Influence of morphology. *Applied physics letters*, 94(15):153109, 2009.

[71] Guillaume Baffou, Romain Quidant, and F Javier García de Abajo. Nanoscale control of optical heating in complex plasmonic systems. *ACS nano*, 4(2):709–716, 2010.

[72] Guillaume Baffou and Hervé Rigneault. Femtosecond-pulsed optical heating of gold nanoparticles. *Physical review B*, 84(3):035415, 2011.

[73] Zhiguang Wu, Changyong Gao, Johannes Frueh, Jianming Sun, and Qiang He. Remote-controllable explosive polymer multilayer tubes for rapid cancer cell killing. *Macromolecular rapid communications*, 36(15):1444–1449, 2015.

[74] Balaji Panchapakesan, Shaoxin Lu, Kousik Sivakumar, Kasif Taker, Gregory Cesarone, and Eric Wickstrom. Single-wall carbon nanotube nanobomb agents for killing breast cancer cells. *Nanobiotechnology*, 1(2):133–139, 2005.

[75] Michael B Ross, Chad A Mirkin, and George C Schatz. Optical properties of one-, two-, and three-dimensional arrays of plasmonic nanostructures. *The journal of physical chemistry C*, 120(2):816–830, 2016.

[76] ML Glasser and IJ Zucker. Lattice sums. In *Theoretical chemistry: advances and perspectives*, pages 67–139. Elsevier, 1980.

[77] Shengli Zou, Nicolas Janel, and George C Schatz. Silver nanoparticle array structures that produce remarkably narrow plasmon lineshapes. *The journal of chemical physics*, 120(23):10871–10875, 2004.

[78] Shengli Zou and George C Schatz. Narrow plasmonic/photonic extinction and scattering line shapes for one and two dimensional silver nanoparticle arrays. *The journal of chemical physics*, 121(24):12606–12612, 2004.

[79] Weijia Wang, Mohammad Ramezani, Aaro I Väkeväinen, Päivi Törmä, Jaime Gómez Rivas, and Teri W Odom. The rich photonic world of plasmonic nanoparticle arrays. *Materials today*, 2017.

[80] G Vecchi, V Giannini, and J Gómez Rivas. Shaping the fluorescent emission by lattice resonances in plasmonic crystals of nanoantennas. *Physical review letters*, 102(14):146807, 2009.

[81] AI VaÌĹkevaÌĹinen, RJ Moerland, HT Rekola, A-P Eskelinen, J-P Martikainen, D-H Kim, and P ToÌĹrmaÌĹ. Plasmonic surface lattice resonances at the strong coupling regime. *Nano letters*, 14(4):1721–1727, 2013.

[82] KT Carron, W Fluhr, M Meier, A Wokaun, and HW Lehmann. Resonances of two-dimensional particle gratings in surface-enhanced raman scattering. *JOSA B*, 3(3):430–440, 1986.

[83] Gabriel Lozano, Said RK Rodriguez, Marc A Verschuuren, and Jaime Gómez Rivas. Metallic nanostructures for efficient led lighting. *Light: Science and Applications*, 5(6):e16080, 2016.

[84] Wei Zhou, Montacer Dridi, Jae Yong Suh, Chul Hoon Kim, Dick T Co, Michael R Wasielewski, George C Schatz, Teri W Odom, et al. Lasing action in strongly coupled plasmonic nanocavity arrays. *Nature nanotechnology*, 8(7):506, 2013.

[85] Thomas W Ebbesen, H JêŐň Lezec, HF Ghaemi, Tineke Thio, and PA Wolff. Extraordinary optical transmission through sub-wavelength hole arrays. *Nature*, 391(6668):667, 1998.

[86] Ephraim Shahmoon, Dominik S Wild, Mikhail D Lukin, and Susanne F Yelin. Cooperative resonances in light scattering from two-dimensional atomic arrays. *Physical review letters*, 118(11):113601, 2017.

[87] Meng Khoon Tey, Zilong Chen, Syed Abdullah Aljunid, Brenda Chng, Florian Huber, Gleb Maslennikov, and Christian Kurtsiefer. Strong interaction between light and a single trapped atom without the need for a cavity. *Nature physics*, 4(12):924, 2008.

[88] Herbert Walther, Benjamin TH Varcoe, Berthold-Georg Englert, and Thomas Becker. Cavity quantum electrodynamics. *Reports on progress in physics*, 69(5):1325, 2006.

[89] Robert J Bettles, Simon A Gardiner, and Charles S Adams. Enhanced optical cross section via collective coupling of atomic dipoles in a 2d array. *Physical review letters*, 116(10):103602, 2016.

[90] Zhi-Yuan Li and Younan Xia. Metal nanoparticles with gain toward single-molecule detection by surface-enhanced raman scattering. *Nano letters*, 10(1):243–249, 2009.

[91] Alejandro Manjavacas. Anisotropic optical response of nanostructures with balanced gain and loss. *ACS photonics*, 3(7):1301–1307, 2016.

[92] Xunya Jiang and CM Soukoulis. Time dependent theory for random lasers. *Physical review letters*, 85(1):70, 2000.

[93] A Fang, Th Koschny, M Wegener, and CM Soukoulis. Self-consistent calculation of metamaterials with gain. *Physical review B*, 79(24):241104, 2009.

[94] Anan Fang, Thomas Koschny, and Costas M Soukoulis. Lasing in metamaterial nanostructures. *Journal of optics*, 12(2):024013, 2010.

[95] Sebastian Wuestner, Andreas Pusch, Kosmas L Tsakmakidis, Joachim M Hamm, and Ortwin Hess. Overcoming losses with gain in a negative refractive index metamaterial. *Physical review letters*, 105(12):127401, 2010.

[96] Sebastian Wuestner, Andreas Pusch, Kosmas L Tsakmakidis, Joachim M Hamm, and Ortwin Hess. Gain and plasmon dynamics in active negative-index metamaterials. *Philosophical Transactions of the Royal Society of London A: Mathematical, Physical and Engineering Sciences*, 369(1950):3525–3550, 2011.

[97] Joachim M Hamm, Sebastian Wuestner, Kosmas L Tsakmakidis, and Ortwin Hess. Theory of light amplification in active fishnet metamaterials. *Physical review letters*, 107(16):167405, 2011.

[98] Chris Fietz and Costas M Soukoulis. Finite element simulation of microphotonic lasing system. *Optics express*, 20(10):11548–11560, 2012.

[99] J Cuerda, F Rüting, FJ García-Vidal, and J Bravo-Abad. Theory of lasing action in plasmonic crystals. *Physical review B*, 91(4):041118, 2015.

[100] J Cuerda, FJ García-Vidal, and J Bravo-Abad. Spatio-temporal modeling of lasing action in core–shell metallic nanoparticles. *ACS photonics*, 3(10):1952–1960, 2016.

[101] Alexey V Krasavin, Thanh Phong Vo, Wayne Dickson, Padraig M Bolger, and Anatoly V Zayats. All-plasmonic modulation via stimulated emission of copropagating surface plasmon polaritons on a substrate with gain. *Nano letters*, 11(6):2231–2235, 2011.

[102] Rupert F Oulton, Volker J Sorger, Thomas Zentgraf, Ren-Min Ma, Christopher Gladden, Lun Dai, Guy Bartal, and Xiang Zhang. Plasmon lasers at deep subwavelength scale. *Nature*, 461(7264):629, 2009.

[103] Alexander A Govyadinov and Viktor A Podolskiy. Gain-assisted slow to superluminal group velocity manipulation in nanowaveguides. *Physical review letters*, 97(22):223902, 2006.

[104] Zongfu Yu, Georgios Veronis, Shanhui Fan, and Mark L Brongersma. Gain-induced switching in metal-dielectric-metal plasmonic waveguides. *Applied physics letters*, 92(4):041117, 2008.

[105] Jie Wang, Dezhuan Han, Ang Chen, Yunyun Dai, Ming Zhou, Xinhua Hu, Zongfu Yu, Xiaohan Liu, Lei Shi, and Jian Zi. Using active gain to maximize light absorption. *Physical review B*, 96(19):195419, 2017.

[106] Zhichao Ruan. Spatial mode control of surface plasmon polariton excitation with gain medium: from spatial differentiator to integrator. *Optics letters*, 40(4):601–604, 2015.

[107] Robert Williams Wood. Xlii. on a remarkable case of uneven distribution of light in a diffraction grating spectrum. *The London, Edinburgh, and Dublin Philosophical Magazine and Journal of Science*, 4(21):396–402, 1902.

[108] A Sharon, S Glasberg, D Rosenblatt, and AA Friesem. Metal-based resonant grating waveguide structures. *JOSA A*, 14(3):588–595, 1997.

[109] Evgeni Popov, Daniel Maystre, RC McPhedran, Michel Nevière, MC Hutley, and GH Derrick. Total absorption of unpolarized light by crossed gratings. *Optics express*, 16(9):6146–6155, 2008.

[110] VG Kravets, F Schedin, and AN Grigorenko. Plasmonic blackbody: Almost complete absorption of light in nanostructured metallic coatings. *Physical review B*, 78(20):205405, 2008.

[111] A Polyakov, S Cabrini, S Dhuey, B Harteneck, PJ Schuck, and HA Padmore. Plasmonic light trapping in nanostructured metal surfaces. *Applied physics letters*, 98(20):203104, 2011.

[112] Marine Laroche, Christophe Arnold, François Marquier, Rémi Carminati, J-J Greffet, S Collin, N Bardou, and J-L Pelouard. Highly directional radiation generated by a tungsten thermal source. *Optics letters*, 30(19):2623–2625, 2005.

[113] Zhichao Ruan and Shanhui Fan. Temporal coupled-mode theory for fano resonance in light scattering by a single obstacle. *The journal of physical chemistry C*, 114(16):7324–7329, 2009.

[114] Zhichao Ruan and Shanhui Fan. Temporal coupled-mode theory for light scattering by an arbitrarily shaped object supporting a single resonance. *Physical review A*, 85(4):043828, 2012.

[115] Jean-Jacques Greffet and Manuel Nieto-Vesperinas. Field theory for generalized bidirectional reflectivity: derivation of helmholtz's reciprocity principle and kirchhoff's law. *JOSA A*, 15(10):2735–2744, 1998.

[116] Rémi Carminati and Jean-Jacques Greffet. Near-field effects in spatial coherence of thermal sources. *Physical review letters*, 82(8):1660, 1999.

[117] Lei Zhang, Chung Y Chan, Jia Li, and Hock C Ong. Rational design of high performance surface plasmon resonance sensors based on two-dimensional metallic hole arrays. *Optics express*, 20(11):12610–12621, 2012.

[118] Weitao Ma, Jun Zhou, Shuiping Huang, and Hongwei Yuan. Characteristic of subwavelength dielectric grating with metal layer and its sensing applications. *Zhongguo Jiguang(Chinese Journal of Lasers)*, 38(9):0905008–5, 2011.

[119] Chihhui Wu, III Burton Neuner, Gennady Shvets, Jeremy John, Andrew Milder, Byron Zollars, and Steve Savoy. Large-area wide-angle spectrally selective plasmonic absorber. *Physical review B*, 84(7):075102, 2011.

[120] Frank Neubrech, Annemarie Pucci, Thomas Walter Cornelius, Shafqat Karim, Aitzol García-Etxarri, and Javier Aizpurua. Resonant plasmonic and vibrational coupling in a tailored nanoantenna for infrared detection. *Physical review letters*, 101(15):157403, 2008.

[121] Na Liu, Ming L Tang, Mario Hentschel, Harald Giessen, and A Paul Alivisatos. Nanoantenna-enhanced gas sensing in a single tailored nanofocus. *Nature materials*, 10(8):631, 2011.

[122] Reuven Gordon, David Sinton, Karen L Kavanagh, and Alexandre G Brolo. A new generation of sensors based on extraordinary optical transmission. *Accounts of chemical research*, 41(8):1049–1057, 2008.

[123] Ahmet A Yanik, Arif E Cetin, Min Huang, Alp Artar, S Hossein Mousavi, Alexander Khanikaev, John H Connor, Gennady Shvets, and Hatice Altug. Seeing protein monolayers with naked eye through plasmonic fano resonances. *Proceedings of the National Academy of Sciences*, 108(29):11784–11789, 2011.

[124] Yang Shen, Jianhua Zhou, Tianran Liu, Yuting Tao, Ruibin Jiang, Mingxuan Liu, Guohui Xiao, Jinhao Zhu, Zhang-Kai Zhou, Xuehua Wang, et al. Plasmonic gold mushroom arrays with refractive index sensing figures of merit approaching the theoretical limit. *Nature communications*, 4:2381, 2013.

[125] Jiun-Chan Yang, Jin Ji, James M Hogle, and Dale N Larson. Multiplexed plasmonic sensing based on small-dimension nanohole arrays and intensity interrogation. *Biosensors and bioelectronics*, 24(8):2334–2338, 2009.

[126] Weiliang Jin, Chinmay Khandekar, Adi Pick, Athanasios G Polimeridis, and Alejandro W Rodriguez. Amplified and directional spontaneous emission from arbitrary composite bodies: A self-consistent treatment of purcell effect below threshold. *Physical Review B*, 93(12):125415, 2016.

[127] Zhichao Ruan and Shanhui Fan. Superscattering of light from subwavelength nanostructures. *Physical review letters*, 105(1):013901, 2010.

[128] Boris Luk'yanchuk, Nikolay I Zheludev, Stefan A Maier, Naomi J Halas, Peter Nordlander, Harald Giessen, and Chong Tow Chong. The fano resonance in plasmonic nanostructures and metamaterials. *Nature materials*, 9(9):707, 2010.

[129] Na Liu, Martin Mesch, Thomas Weiss, Mario Hentschel, and Harald Giessen. Infrared perfect absorber and its application as plasmonic sensor. *Nano letters*, 10(7):2342–2348, 2010.

[130] Ross Stanley. Plasmonics in the mid-infrared. *Nature photonics*, 6(7):409, 2012.

[131] Hai Hu, Xiaoxia Yang, Feng Zhai, Debo Hu, Ruina Liu, Kaihui Liu, Zhipei Sun, and Qing Dai. Far-field nanoscale infrared spectroscopy of vibrational

fingerprints of molecules with graphene plasmons. *Nature communications*, 7:12334, 2016.

[132] Lauren Zundel and Alejandro Manjavacas. Spatially resolved optical sensing using graphene nanodisk arrays. *ACS photonics*, 4(7):1831–1838, 2017.

[133] Arseniy I Kuznetsov, Andrey E Miroshnichenko, Mark L Brongersma, Yuri S Kivshar, and Boris LukâĂŹyanchuk. Optically resonant dielectric nanostructures. *Science*, 354(6314):aag2472, 2016.

[134] Guanying Chen, Hailong Qiu, Paras N Prasad, and Xiaoyuan Chen. Upconversion nanoparticles: design, nanochemistry, and applications in theranostics. *Chemical reviews*, 114(10):5161–5214, 2014.

[135] Feng Wang, Debapriya Banerjee, Yongsheng Liu, Xueyuan Chen, and Xiaogang Liu. Upconversion nanoparticles in biological labeling, imaging, and therapy. *Analyst*, 135(8):1839–1854, 2010.

[136] Bo Zhou, Bingyang Shi, Dayong Jin, and Xiaogang Liu. Controlling upconversion nanocrystals for emerging applications. *Nature nanotechnology*, 10(11):924, 2015.

[137] Ling Li, Kory Green, Hans Hallen, and Shuang Fang Lim. Enhancement of single particle rare earth doped nayf4: Yb, er emission with a gold shell. *Nanotechnology*, 26(2):025101, 2014.

[138] Ning Liu, Weiping Qin, Guanshi Qin, Tao Jiang, and Dan Zhao. Highly plasmon-enhanced upconversion emissions from au@ β-nayf 4: Yb, tm hybrid nanostructures. *Chemical communications*, 47(27):7671–7673, 2011.

[139] Jijun He, Wei Zheng, Filip Ligmajer, Chi-Fai Chan, Zhiyong Bao, Ka-Leung Wong, Xueyuan Chen, Jianhua Hao, Jiyan Dai, Siu-Fung Yu, et al. Plasmonic enhancement and polarization dependence of nonlinear upconversion emissions from single gold nanorod@ sio 2@ caf 2: Yb 3+, er 3+ hybrid core–shell–satellite nanostructures. *Light: science and applications*, 6(5):e16217, 2017.

[140] Kory Green, Janina Wirth, and Shuang Fang Lim. Optical investigation of gold shell enhanced 25 nm diameter upconverted fluorescence emission. *Nanotechnology*, 27(13):135201, 2016.

[141] Gerald L Pollack. Kapitza resistance. *Revew of modern physics*, 41:48, 1969.

[142] Eric T Swartz and Robert O Pohl. Thermal boundary resistance. *Revew of modern physics*, 61:605, 1989.

[143] Patrick E Hopkins. Thermal transport across solid interfaces with nanoscale imperfections: effects of roughness, disorder, dislocations, and bonding on thermal boundary conductance. *ISRN Mech. Eng.*, 2013:682586, 2013.

[144] Christian Monachon, Ludger Weber, and Chris Dames. Thermal boundary conductance: A materials science perspective. *Annu. Rev. Mater. Res.*, 46:433–463, 2016.

[145] K. R. Li, M. I. Stockman, and D. J. Bergman. Self-similar chain of metal nanospheres as an efficient nanolens. *Physical review letters*, 91:227402, 2003.

[146] RM Costescu, DG Cahill, FH Fabreguette, ZA Sechrist, and SM George. Ultra-low thermal conductivity in w/al2o3 nanolaminates. *Science*, 303:989–990, 2004.

[147] Hongxing Xu. Multilayered metal core-shell nanostructures for inducing a large and tunable local optical field. *Physical review B*, 72(7):073405, 2005.

[148] G. Mie. Beiträge zur optik trüber medien, speziell kolloidaler metallösungen. *Ann. Phys. (Leipzig)*, 25:377–445, 1908.

[149] J. D. Jackson. *Classical Electrodynamics*. Wiley, New York, 1999.

[150] Zhibin Lin, Leonid V. Zhigilei, and Vittorio Celli. Electron-phonon coupling and electron heat capacity of metals under conditions of strong electron-phonon nonequilibrium. *Physical review B*, 77:075133, 2008.

[151] O Ekici, RK Harrison, NJ Durr, DS Eversole, M Lee, and A Ben-Yakar. Thermal analysis of gold nanorods heated with femtosecond laser pulses. *Journal of physics D: applied physics*, 41(18):185501, 2008.

[152] Pavlo Zolotavin, Alessandro Alabastri, Peter Nordlander, and Douglas Natelson. Plasmonic heating in au nanowires at low temperatures: the role of thermal boundary resistance. *ACS nano*, 10(7):6972–6979, 2016.

[153] A Plech, V Kotaidis, S Grésillon, C Dahmen, and G Von Plessen. Laser-induced heating and melting of gold nanoparticles studied by time-resolved x-ray scattering. *Physical review B*, 70:195423, 2004.

[154] Mark W Knight, Lifei Liu, Yumin Wang, Lisa Brown, Shaunak Mukherjee, Nicholas S King, Henry O Everitt, Peter Nordlander, and Naomi J Halas. Aluminum plasmonic nanoantennas. *Nano letters*, 12:6000–6004, 2012.

[155] Jana Olsona, Alejandro Manjavacas, Lifei Liub, Wei-Shun Chang, Benjamin Foerster, Nicholas S. King, Mark W. Knight, Peter Nordlander, Naomi J. Halas, , and Stephan Link. Vivid, full-color aluminum plasmonic pixels. *Proceedings of the national academy of sciences*, 111:14348–14353, 2014.

[156] Ali Sobhani, Alejandro Manjavacas, Yang Cao, Michael J McClain, F Javier García de Abajo, Peter Nordlander, and Naomi J Halas. Pronounced linewidth narrowing of an aluminum nanoparticle plasmon resonance by interaction with an aluminum metallic film. *Nano letters*, 15:6946–6951, 2015.

[157] Chenglin Du, Wei Cai, Wei Wu, Li Li, Yinxiao Xiang, Mengxin Ren, Xinzheng Zhang, and Jingjun Xu. Evolution and coupling of plasmonic modes in single-crystal aluminum nanoridge antennas. *ACS photonics*, 5(8):2983–2989, 2018.

[158] Seungchul Kim, Jonghan Jin, Young-Jin Kim, In-Yong Park, Yunseok Kim, and Seung-Woo Kim. High-harmonic generation by resonant plasmon field enhancement. *Nature*, 453:757–760, 2008.

[159] In-Yong Park, Seungchul Kim, Joonhee Choi, Dong-Hyub Lee, Young-Jin Kim, Matthias F. Kling, Mark I. Stockman, and Seung-Woo Kim. Plasmonic generation of ultrashort extreme-ultraviolet light pulses. *Nat. Photon.*, 5:677–681, 2011.

[160] Pramod Reddy, Kenneth Castelino, and Arun Majumdar. Diffuse mismatch model of thermal boundary conductance using exact phonon dispersion. *Applied physics letters*, 87:211908, 2005.

[161] OW Käding, H Skurk, and KE Goodson. Thermal conduction in metallized silicon-dioxide layers on silicon. *Applied Physics Letters*, 65(13):1629–1631, 1994.

[162] Patrick E Hopkins. Thermal transport across solid interfaces with nanoscale imperfections: effects of roughness, disorder, dislocations, and bonding on thermal boundary conductance. *ISRN Mechanical Engineering*, 2013, 2013.

[163] Heng-Chieh Chien, Da-Jeng Yao, and Cheng-Ting Hsu. Measurement and evaluation of the interfacial thermal resistance between a metal and a dielectric. *Applied physics letters*, 93:231910, 2008.

[164] Mark D Losego, Martha E Grady, Nancy R Sottos, David G Cahill, and Paul V Braun. Effects of chemical bonding on heat transport across interfaces. *Nat. Mater.*, 11:502–506, 2012.

[165] L Xue, P Keblinski, SR Phillpot, SU-S Choi, and JA Eastman. Two regimes of thermal resistance at a liquid–solid interface. *Journal of chemical physics*, 118:337–339, 2003.

[166] Yun-Sheng Chen, Wolfgang Frey, Seungsoo Kim, Pieter Kruizinga, Kimberly Homan, and Stanislav Emelianov. Silica-coated gold nanorods as photoacoustic signal nanoamplifiers. *Nano letters*, 11:348–354, 2011.

[167] JW Cahn and F Lärche. Surface stress and the chemical equilibrium of small crystalsâĂŤii. solid particles embedded in a solid matrix. *Acta metallurgica*, 30(1):51–56, 1982.

[168] Robert C Cammarata and Karl Sieradzki. Surface and interface stresses. *Annual review of materials science*, 24(1):215–234, 1994.

[169] James F Shackelford, Young-Hwan Han, Sukyoung Kim, and Se-Hun Kwon. *CRC materials science and engineering handbook*. CRC press, 2016.

[170] Willi Pabst and EVA Gregorová. Elastic properties of silica polymorphsâĂŤa review. *Ceramics-Silikaty*, 57(3):167–184, 2013.

[171] Rijil Thomas, Sivaramapanicker Sreejith, Hrishikesh Joshi, Srikanth Pedireddy, Mihaiela Corina Stuparu, Yanli Zhao, and Soh Cheong Boon. Optically induced structural instability in gold–silica nanostructures: A case study. *The journal of physical chemistry C*, 120(20):11230–11236, 2016.

[172] Vincenzo Schettino and Roberto Bini. Molecules under extreme conditions: Chemical reactions at high pressure. *Physical chemistry chemical physics*, 5(10):1951–1965, 2003.

[173] Roberto Bini. Laser-assisted high-pressure chemical reactions. *Accounts of chemical research*, 37(2):95–101, 2004.

[174] AP Alivisatos, TD Harris, LE Brus, and A Jayaraman. Resonance raman scattering and optical absorption studies of cdse microclusters at high pressure.

[175] Samuele Fanetti, Margherita Citroni, and Roberto Bini. Pressure-induced fluorescence of pyridine. *J. Phys. Chem. B*, 115:12051–12058, 2011.

[176] Samuele Fanetti, Margherita Citroni, Lorenzo Malavasi, Gianluca A Artioli, Paolo Postorino, and Roberto Bini. High-pressure optical properties and chemical stability of picene. *J. Phys. Chem. C*, 117:5343–5351, 2013.

[177] Weiwei Zhang, Artem R Oganov, Alexander F Goncharov, Qiang Zhu, Salah Eddine Boulfelfel, Andriy O Lyakhov, Elissaios Stavrou, Maddury Somayazulu, Vitali B Prakapenka, and Zuzana Konôpková. Unexpected stable stoichiometries of sodium chlorides. *Science*, 342:1502–1505, 2013.

[178] A. I. Denisyuk, F. Jonsson, K. F. MacDonald, N. I. Zheludev, and F. J. García de Abajo. Luminescence readout of nanoparticle phase state. *Applied physics letters*, 92:093112, 2008.

[179] E. Prodan, C. Radloff, N. J. Halas, and P. Nordlander. Hybridization model for the plasmon response of complex nanostructures. *Science*, 302:419–422, 2003.

[180] Lord Rayleigh. Iii. note on the remarkable case of diffraction spectra described by prof. wood. *The London, Edinburgh, and Dublin Philosophical Magazine and Journal of Science*, 14(79):60–65, 1907.

[181] Ugo Fano. Some theoretical considerations on anomalous diffraction gratings. *Physical review*, 50(6):573, 1936.

[182] FJ Garcia de Abajo, R Gómez-Medina, and JJ Sáenz. Full transmission through perfect-conductor subwavelength hole arrays. *Physical review E*, 72(1):016608, 2005.

[183] Baptiste Auguié and William L Barnes. Collective resonances in gold nanoparticle arrays. *Physical review letters*, 101(14):143902, 2008.

[184] G Zumofen, NM Mojarad, V Sandoghdar, and M Agio. Perfect reflection of light by an oscillating dipole. *Physical review letters*, 101(18):180404, 2008.

[185] YLA Rezus, SG Walt, R Lettow, A Renn, G Zumofen, S Götzinger, and V Sandoghdar. Single-photon spectroscopy of a single molecule. *Physical review letters*, 108(9):093601, 2012.

[186] Jonathan D Hood, Akihisa Goban, Ana Asenjo-Garcia, Mingwu Lu, Su-Peng Yu, Darrick E Chang, and HJ Kimble. Atom–atom interactions around the band edge of a photonic crystal waveguide. *Proceedings of the national academy of sciences*, 113(38):10507–10512, 2016.

[187] David J Bergman and Mark I Stockman. Surface plasmon amplification by stimulated emission of radiation: quantum generation of coherent surface plasmons in nanosystems. *Physical review letters*, 90(2):027402, 2003.

[188] Marlan O Scully and M Suhail Zubairy. Quantum optics, 1999.

[189] Mark I Stockman. The spaser as a nanoscale quantum generator and ultrafast amplifier. *Journal of optics*, 12(2):024004, 2010.

[190] Z Ficek and Ryszard Tanaś. Entangled states and collective nonclassical effects in two-atom systems. *Physics reports*, 372(5):369–443, 2002.

[191] Kyozaburo Kambe. Theory of low-energy electron diffraction. *Zeitschrift für Naturforschung A*, 23(9):1280–1294, 1968.

[192] Daniel Barredo, Sylvain De Léséleuc, Vincent Lienhard, Thierry Lahaye, and Antoine Browaeys. An atom-by-atom assembler of defect-free arbitrary 2d atomic arrays. *Science*, page aah3778, 2016.

[193] Ajit Srivastava, Meinrad Sidler, Adrien V Allain, Dominik S Lembke, Andras Kis, and A Imamoğlu. Optically active quantum dots in monolayer wse 2. *Nature nanotechnology*, 10(6):491, 2015.

[194] Yu-Ming He, Genevieve Clark, John R Schaibley, Yu He, Ming-Cheng Chen, Yu-Jia Wei, Xing Ding, Qiang Zhang, Wang Yao, Xiaodong Xu, et al. Single quantum emitters in monolayer semiconductors. *Nature nanotechnology*, 10(6):497, 2015.

[195] Patrick Back, Sina Zeytinoglu, Aroosa Ijaz, Martin Kroner, and Atac Imamoğlu. Realization of an electrically tunable narrow-bandwidth atomically thin mirror using monolayer mose 2. *Physical review letters*, 120(3):037401, 2018.

[196] Giovanni Scuri, You Zhou, Alexander A High, Dominik S Wild, Chi Shu, Kristiaan De Greve, Luis A Jauregui, Takashi Taniguchi, Kenji Watanabe, Philip Kim, et al. Large excitonic reflectivity of monolayer mose 2 encapsulated in hexagonal boron nitride. *Physical review letters*, 120(3):037402, 2018.

[197] Zhong Lin, Bruno R Carvalho, Ethan Kahn, Ruitao Lv, Rahul Rao, Humberto Terrones, Marcos A Pimenta, and Mauricio Terrones. Defect engineering of two-dimensional transition metal dichalcogenides. *2D materials*, 3(2):022002, 2016.

[198] Chitraleema Chakraborty, Laura Kinnischtzke, Kenneth M Goodfellow, Ryan Beams, and A Nick Vamivakas. Voltage-controlled quantum light from an atomically thin semiconductor. *Nature nanotechnology*, 10(6):507, 2015.

[199] Carmen Palacios-Berraquero, Dhiren M Kara, Alejandro R-P Montblanch, Matteo Barbone, Pawel Latawiec, Duhee Yoon, Anna K Ott, Marko Loncar,

Andrea C Ferrari, and Mete Atatüre. Large-scale quantum-emitter arrays in atomically thin semiconductors. *Nature communications*, 8:15093, 2017.

[200] Stewart D Jenkins and Janne Ruostekoski. Metamaterial transparency induced by cooperative electromagnetic interactions. *Physical review letters*, 111(14):147401, 2013.

[201] F. E. Low. *Classical Field Theory: Electromagnetism and Gravitation*. John Wiley and Sons, New York, 1997.

[202] F. J. García de Abajo. Multiple scattering of radiation in clusters of dielectrics. *Physical review B*, 60:6086–6102, 1999.

[203] A. Messiah. *Quantum Mechanics*. North-Holland, New York, 1966.

[204] FJ Garcia de Abajo, MA Van Hove, and CS Fadley. Multiple scattering of electrons in solids and molecules: A cluster-model approach. *Physical review B*, 63(7):075404, 2001.

[205] LA Blanco and FJ García de Abajo. Spontaneous light emission in complex nanostructures. *Physical review B*, 69(20):205414, 2004.

[206] J Lombard, F Detcheverry, and S Merabia. Influence of the electron–phonon interfacial conductance on the thermal transport at metal/dielectric interfaces. *Journal of physical chemistry*, 27:015007, 2014.

[207] Haitao Wang, Yibin Xu, Masato Shimono, Yoshihisa Tanaka, and Masayoshi Yamazaki. Computation of interfacial thermal resistance by phonon diffuse mismatch model. *Mate. Trans.*, 48:2349–2352, 2007.

[208] Ho-Ki Lyeo and David G Cahill. Thermal conductance of interfaces between highly dissimilar materials. *Physical review B*, 73:144301, 2006.

[209] Robert J Stevens, Andrew N Smith, and Pamela M Norris. Measurement of thermal boundary conductance of a series of metal-dielectric interfaces by the transient thermoreflectance technique. *J. Heat Transfer*, 127:315–322, 2005.

[210] Mihai G Burzo, Pavel L Komarov, and Peter E Raad. Thermal transport properties of gold-covered thin-film silicon dioxide. *IEEE Trans. Compon. Packag. Technol.*, 26:80–88, 2003.

[211] ET Swartz and RO Pohl. Thermal resistance at interfaces. *Applied physics letters*, 51:2200–2202, 1987.

[212] Ryozo Kato, Yibin Xu, and Masahiro Goto. Development of a frequency-domain method using completely optical techniques for measuring the interfacial thermal resistance between the metal film and the substrate. *Jpn. J. Appl. Phys.*, 50:106602, 2011.

[213] Pavlo Zolotavin, Alessandro Alabastri, Peter Nordlander, and Douglas Natelson. Plasmonic heating in au nanowires at low temperatures: The role of thermal boundary resistance. *ACS nano*, 10:6972–6979, 2016.

[214] Patrick E Hopkins and Pamela M Norris. Substrate influence in electron–phonon coupling measurements in thin au films. *Appl. Surf. Sci.*, 253:6289–6294, 2007.

[215] Patrick E Hopkins, Jared L Kassebaum, and Pamela M Norris. Effects of electron scattering at metal-nonmetal interfaces on electron-phonon equilibration in gold films. *Jornal of applied physics*, 105:023710, 2009.

[216] Liang Guo, Stephen L Hodson, Timothy S Fisher, and Xianfan Xu. Heat transfer across metal-dielectric interfaces during ultrafast-laser heating. *J. Heat Transfer*, 134:042402, 2012.

[217] AV Sergeev. Electronic kapitza conductance due to inelastic electron-boundary scattering. *Physical review B*, 58:R10199, 1998.

[218] H Sam Huang, Vikas Varshney, Jennifer L Wohlwend, and Ajit K Roy. Heat transfer at aluminum–water interfaces: Effect of surface roughness. *J. Nanotech. Eng. Med.*, 3:031008, 2012.

[219] G. Baffou, R. Quidant, and F. J. García de Abajo. Nanoscale control of optical heating in complex plasmonic systems. *ACS nano*, 4:709–716, 2010.

[220] Kuiru Li, Mark I Stockman, and David J Bergman. Self-similar chain of metal nanospheres as an efficient nanolens. *Physical review letters*, 91(22):227402, 2003.

[221] Marlan O Scully. Ms zubairy quantum optics. *CambridgePress, London*, 1997.